

DANCING ATOP THE GRAVE THAT HAS THEIR NAME: GEOMETRIC, RADIATIVE, AND HYDRODYNAMIC SIMULATIONS OF COLLIDING WIND NEBULAE

By

Ryan M. T. White

A THESIS SUBMITTED TO MACQUARIE UNIVERSITY
FOR THE DEGREE OF MASTER OF RESEARCH
FACULTY OF SCIENCE AND ENGINEERING
SCHOOL OF MATHEMATICAL AND PHYSICAL SCIENCES
NOVEMBER 2025

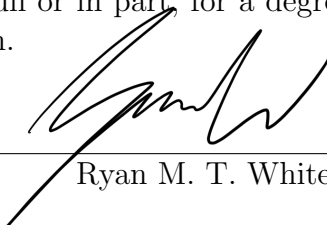


© Ryan M. T. White, 2025.

Typeset in L^AT_EX 2_ε.

This thesis is submitted to Macquarie University in fulfilment of the requirement for the Degree of Master of Research.

The work presented in this thesis is, to the best of my knowledge and belief, original except as acknowledged in the text. I hereby declare that I have not submitted this material, either in full or in part, for a degree at this or any other institution.



Ryan M. T. White

Acknowledgements

I would have been driven mad a hundred or more times over if it weren't for your unceasing support this year, Sascha. From 5am looping right back over to 6am, you were always there when I needed to rant, some words of affirmation, or some distraction from the various horrors unfolding. I'm convinced that there is no better hype man than you, whether it's about the mundane or the sublime, and you're the first with whom I share my wins and losses alike. Thank you for being who you are.

Macquarie would be a lesser place if it weren't for my lovely friends Gabby, Jayde, and Jack. Collectively, you made me feel right at home at MQ, and there's no one I'd rather go for coffee runs or lunch with. Although I wouldn't wish the horrors we experienced – literal and figurative – on my worst enemies, I am glad we got to bond over them and come out the other side with aura second to none.

I wouldn't have made it through the year if not for you, Luci; truly, I'm not sure I could have done half of this thesis without your encouragement and humility early on. How lucky I was to catch you, the MCFOST expert, in the last year of your PhD. That code is an untameable beast, and you helped me realise that I'm actually not stupid for struggling to no end with its villainy. Many of my friends should be thanking you in particular for motivating me to start baking regularly during the year, too. I hope post-PhD life is filled with treats and rat behaviour both.

A special thank you goes out to Max, Grace, and Stef, who made me feel so very welcome in my move to Sydney. You guys are truly the only ones who could *almost* make me care about instrumentation, and I would seldom make the trip to USyd if it weren't for you. I cannot wait for more time spent together. A mandatory shout out, too, to Nada and Smriti for being lovely human beings with a *mean* fashion sense; I'll never look at black and red the same way again.

To my Queensland astro friends, Katelyn, Shashank, Hugh, and Jess, oh so far away but not in spirit. I always loved hearing from you all about what was going on back at home, be it shenanigans transpiring at UQ, a nice painting timelapse, or pictures of clouds over the Brown Snake. I can't wait to see you all again soon.

This thesis would not be possible without the constant flow of caffeine and smiles from my darlings at Cult: Andreas, Jasmin, Gabrielle, Elle, Hynobi, Cathy, Vasili, Sushil, and Jenna. While I may have gone to Cult multiple times a day for the coffee, I would have gone if for no other reason than to see you all.

On some level I need to thank Gang of Youths, whose albums have, this year in particular, had an unreasonable impact on me. *The Positions* for reminding me that there is self discovery in turmoil, and healing always follows. *Let Me Be Clear* for a sobering melancholy that welcomes empathy, and for *Still Unbeaten Life* whose lyrics made their way into the title of this Thesis. *Go Farther In Lightness* for a life affirming

quality like no other, an ode to the joy of feeling and feeling everything, beautiful or painful. And finally, *angel in realtime* for encapsulating the higher dimensions inherent in our most complicated relationships. Music keeps me going, and I am glad to have existed in the Universe at the same time as this beautiful band.

Almost the entire body of simulations within this work were performed on the OzSTAR national facility at Swinburne University of Technology. The OzSTAR program receives funding in part from the Astronomy National Collaborative Research Infrastructure Strategy (NCRIS) allocation provided by the Australian Government, and from the Victorian Higher Education State Investment Fund (VHESIF) provided by the Victorian Government. I am extremely grateful that I was able to hog hundreds of performant CPU cores for months on end, and this thesis would not have been possible without the OzSTAR facility.

It was a pleasure working with Yinuo for much of this year, who was a welcome presence in our numerous Zoom calls with the press and collaborators. Publishing companion papers with you was such a cool experience and there's no one I'd rather share the title of 'Apep wrangler' with. I'd also like to thank Peredur and Noel who routinely offered words of encouragement for our colliding wind binary models, and were more than generous in handing over their old data.

It wouldn't be a thesis on Wolf-Rayet colliding wind binaries without a huge thank you to Peter Tuthill. Over the course of the year you probably added to my 'to-do' list more than my on-the-books supervisors combined, but your enthusiasm for the science always kept me motivated and thinking of new ideas.

I am endlessly grateful to you, Ben, for convincing me to come to Sydney. What a wonderful city this is and I can truly see myself living here forever. You are an endless fountain of ideas and this thesis and my research alike wouldn't be quite the same without your ambitious flair. Even though we can't quite agree on what films *or* food are good or not, I think we're of the same mind in thinking that Wolf-Rayet stars are pretty cool.

And finally, what a joy to work with you for the first time Orsola. Every day felt almost like a race to beat you into the office, and I'm so grateful to have found a supervisor as crazy as me to have meetings practically as the sun rises. I still don't quite believe you when you say you don't really understand dust (if you don't then I'm afraid no one does), but none of this would have been possible without your continued support and words of encouragement.

List of Publications

- **Ryan M. T. White** *et al*, *The Serpent Eating Its Own Tail: Dust Destruction in the Apep Colliding-Wind Nebula*, 2025. Accepted with The Astrophysical Journal, [arXiv.2507.14610](#)
- **Ryan M. T. White**, Peter G. Tuthill, *Wolf-Rayet Colliding Wind Binaries*, 2026. Published in *Encyclopedia of Astrophysics*, Vol 2, pp 584-603, [10.1016/B978-0-443-21439-4.00067-5](#), [arXiv.2412.12534](#)
- Yinuo Han, **Ryan M. T. White** *et al*, *The formation and evolution of dust in the colliding-wind binary Apep revealed by JWST*, 2025. Accepted with The Astrophysical Journal, [arXiv.2507.14498](#)
- Noel D. Richardson *et al* (including **Ryan M. T. White**), *Carbon-rich dust injected into the interstellar medium by Galactic WC binaries survives for hundreds of years*, 2025. Published in The Astrophysical Journal, Vol 987, pp 160, [10.3847/1538-4357/addf30](#), [arXiv:2505.11616](#)

Abstract

Dust is ubiquitous across all astrophysical scales, from planetary systems up to entire galaxies. Some of the earliest carbon dust in the Universe was dispersed throughout galaxies by colliding wind binaries hosting Wolf-Rayet stars. Despite fostering a hostile environment to fragile grains, these systems are able to copiously form dust due to the shock interface at the wind collision zone between the stars. Although these are being observed routinely with ground- and space-based telescopes, their dust formation and properties remains poorly understood in this rare class of system. To investigate this and provide a foundation for future studies, in this thesis we take a dual approach to dust modelling: first, we expand the state-of-the-art geometric model of these nebulae to incorporate a radiative transfer code, hence allowing us to simulate the light curves of these systems and to model far away systems that cannot be directly imaged. Simultaneously we provide new functionality to model the velocity structure of these nebulae so that we may better understand upcoming ALMA datasets of these systems. Finally, we perform the first hydrodynamic simulations of the Apep system to better understand the dust formation in a system that challenges our understanding of colliding wind binaries. Our simulation reproduces Apep's nebula morphology strikingly well and we find that, with a few standard assumptions, the dust production rate in our simulations matches exactly the observational rate. In parallel we study the grain properties in the recently discovered tertiary cavity of the Apep nebula, providing key constraints on any surviving dust within.

Contents

Acknowledgements	v
List of Publications	vii
Abstract	ix
List of Figures	xiii
List of Tables	xv
1 Introduction	1
2 Massive Stellar Multiples	3
2.1 A Brief Cosmic History of Dust and Chemical Enrichment	3
2.2 Dancing with the (Massive) Stars	5
2.2.1 Stellar Evolution, Turned up to $> 30M_{\odot}$	6
2.2.2 Colliding Wind Binaries Hosting Wolf-Rayet Stars	7
2.2.3 Apep	9
2.2.4 Systems Beyond Our View	10
3 Modelling Circumstellar Dust	11
3.1 Hydrodynamic Simulations	11
3.1.1 Hydrodynamic Simulations of Colliding Wind Binaries	14
3.2 Geometric Modelling	16
3.3 Radiative Transfer	18
4 Radiation Transport with Colliding Wind Binaries	21
4.1 Evolving <code>xenomorph</code>	21
4.1.1 Velocity Slicing Nebulae	22
4.1.2 A Varying Dust Mass and Grain Size Distribution	23
4.2 Radiative Transfer with <code>MCFOST</code>	28
4.2.1 Simulating and Processing Radiative Transfer Models	28
4.2.2 Light Curve Parameter Space Exploration	33
4.2.3 Cooling Curve Analysis	37
5 Peering into the Serpent's Dust	41
5.1 Dust Formation	41
5.1.1 Simulation Setup	42

5.1.2	Results	44
5.2	Dust Destruction	51
5.2.1	Effect on Dust Grains in the Cavity	53
6	Conclusions and Future Work	55
A	Appendices	59
A.1	Additional Hydrodynamic Simulation Plots	59
References		63
List of External Links		73

List of Figures

2.1	Colliding Wind Binary morphology	7
2.2	WR CWB Observations	8
3.1	Colliding Wind Shock Structure	15
3.2	Geometric Model Basic Idea	17
3.3	Radiation Transport Schematic	19
4.1	Velocity Sliced Colliding Wind Nebula	23
4.2	Shell Dust Mass Evolution	26
4.3	Grain Size Distribution Exponent Evolution	27
4.4	Apep Radiation Transport	30
4.5	Bandpass Approximations	32
4.6	WR 140 Light Curve Inclination Grid	34
4.7	Effect of Varying Dust Mass and Grain Size Exponent on Light Curve	35
4.8	Dust Mass and Grain Size Exponent Grid Variation Metrics	35
4.9	WR 140 Light Curve Comparison	36
4.10	Apep Temperature Structure	38
4.11	Modelled Apep Cooling Curve	39
5.1	Hydrodynamic Simulation Density Cross Section Comparison	45
5.2	Hydrodynamic Simulation Column Density Comparison	46
5.3	Hydrodynamic Simulation Adiabatic Index Shock Temperature Comparison	47
5.4	Pressure versus Radius Plot of SPH Particles for $\gamma = 1.10$	49
5.5	Hydrodynamic Simulation versus Geometric Model for Apep	50
5.6	Apep's Cavity	52
A.1	Hydrodynamic Simulation Density Cross Section Comparison (Zoomed Out)	59
A.2	Shocked Pressure versus Adiabatic Index	60
A.3	Comparison of Expansion Velocity vs Adiabatic Index	60
A.4	Pressure versus Radius Plot of SPH Particles for $\gamma = 1.01$	61
A.5	Pressure versus Radius Plot of SPH Particles for $\gamma = 5/3$	61
A.6	Pressure versus Radius versus Temperature Plot of SPH Particles for $\gamma = 1.10$	62

List of Tables

4.1	Infrared Band Parameters	31
4.2	WR 140 Light Curve Parameter Estimates	37
5.1	Dust Destruction Cavity Parameters	51

[watching it rain frogs outside the window]

STANLEY SPECTOR

This happens. This is something that
happens.

Magnolia (1999)

1

Introduction

Dust is ubiquitous across all fields in astrophysics; whether studying the formation of planets, the distribution and behaviour of stars in the Milky Way, or even supernovae at cosmological distances, the presence of astrophysical dust impacts the observational characteristics and physical processes of most phenomena. Dust is produced from a variety of stellar sources in our modern Universe, predominantly from stars nearing or reaching the end of their lives – from lower mass asymptotic giant branch stars to the stellar winds and supernovae of massive stars. In the early Universe, before low mass stars had time enough to evolve in large numbers, dust formation was dominated by processes involving massive stars. In this Thesis, we focus on the dust produced by massive stars not yet at death’s door, though fast approaching it.

Wolf-Rayet (WR) stars are the end-of-life phases of the most massive stars, being in the final $\sim 5\%$ of their few million years life. Having shed their hydrogen envelope, the exposed cores of these massive stars are characterised by extreme luminosities, temperatures, and stellar winds to boot; their winds are some of the strongest sustained winds of any star having both high wind speeds ($1000 - 5000 \text{ km s}^{-1}$) and uniquely high mass loss rates ($10^{-5} - 10^{-4} M_{\odot} \text{ yr}^{-1}$, i.e. about 10^9 times more than the solar rate). These physical conditions provide a particularly hostile environment to astrophysical dust which, in our contexts, is made up of fragile molecules of carbon. Yet, despite all odds, there is a wealth of observational evidence that dust forms copiously around a small population of WR stars, and that this nucleation mechanism would have been particularly prevalent for the observed early-Universe dust formation.

What is special about this small population of systems are two factors working in parallel. The first is that the Wolf-Rayet star is of the carbon subtype; these so-called ‘WC’ stars have a uniquely carbon-rich wind, even reaching up to 50% carbon by mass. The second is that these WC stars are in a binary system together with another massive star (be it a main-sequence or evolved O star, or even another WR star). As the two stars in the binary orbit each other, the winds collide to form a bow shock structure. This shock compresses and heats the stellar winds along a cone

interface, where turbulent mixing can very efficiently nucleate carbon grains as the plasma cools. Although these WR stars are not in this ‘colliding wind binary’ (CWB) phase for long ($\lesssim 10^5$ yr), the high mass loss rates of evolved massive stars mean that they are important dust factories in the Galaxy.

Although these systems are rare – there being no more than a few dozen in the Milky Way and Magellanic Clouds – understanding their dust properties are key to understanding the role of massive stars in the Galaxy’s evolution. To do this, we have a variety of tools including, but not limited to, direct imagery and photometric monitoring in the infrared where the thermal dust is luminous. Direct imagery of the nearby CWBs reveals dust extended over $\lesssim 1$ pc scales, and so even the most advanced infrared telescopes today cannot resolve these systems in the LMC/SMC or at the far side of the Galaxy. This leaves photometry – which is not so resolution limited – as a valuable probe into dust formation. Still, there has not yet been a published simulation of the light curve of a dusty colliding wind binary despite decades of observations of such systems, meaning that the literature has skewed towards tailored explanations of these systems rather than systematic reproduction of observations. Hence, developing a light curve model for these systems offers an opportunity to better infer the dust properties across the entire known population rather than a resolvable few. Even within these resolvable few, the conditions that lead to dust formation, and in some cases its destruction once formed, are still broadly unclear. The Apep CWB stands out above the rest as the most puzzling of this class of system, being the only confirmed classical WR+WR and the longest period WR-CWB. To understand how this carbon dust forms across CWBs requires both understanding edge cases, like Apep, as well as the broader population of WR binaries.

We review the current understanding of these WR-CWBs and their place in our cosmic history in Chapter 2; this Chapter is intended as a companion to and expands upon our published book chapter on WR-CWBs, [White & Tuthill \(2026\)](#), to better contextualise the literature in the frame of this work. Chapter 3 overviews the methodology we employ in this thesis, namely the theory behind hydrodynamic simulations and radiative transfer, as well as a geometric model specific to dusty colliding wind nebulae that we have developed in [White et al. \(2024, 2025\)](#). We introduce in Chapter 4 the first ever light curve simulations for these WR-CWBs, made by integrating our geometric models together with a radiative transfer code. Chapter 5 sees us model the Apep colliding wind nebula with a hydrodynamic code for the first time which allows us to compare to recent JWST observations and simultaneously validate the geometric model as a valid tool to describe the circumstellar dust distribution. Finally, we conclude in Chapter 6 and provide multiple avenues of possible future research that are motivated by the caveats and results of this thesis.

Too soon, the wind dies, and the voice
with it.

Amal El-Mohtar, *This Is How You Lose the
Time War*, (2019)

2

Massive Stellar Multiples

Massive stars – those with initial masses $\gtrsim 8M_{\odot}$ and O or B type classifications (hereafter referred to as OB stars) – are one of the dominant influences within galactic environments. Their energy output dwarfs that of the more common low mass stars in both life and death: their intense radiation shapes the nurseries in which they were formed (Poudel et al., 2025), and their eventual supernova explosions can be seen across the Universe when temporarily as bright as even their own host galaxy (Grayling et al., 2023).

In this chapter we give a broad overview of the role of massive stars across cosmic time, and in particular the impact of massive binaries. We go on to describe how, as the stars evolve in these binaries, they can become powerful factories of carbonaceous dust where this circumstellar dust encodes the parameters of the system at its core. This chapter is intended in-part to summarise and otherwise complement my submitted and peer-reviewed book chapter on Wolf-Rayet colliding wind binaries, White & Tuthill (2026), as a background for the astrophysical phenomena discussed in this thesis.

2.1 A Brief Cosmic History of Dust and Chemical Enrichment

The Earth and the Solar System formed approximately 4.5 Gyr ago. The conditions leading to this remain debated (supported theories ranging from WR-wind bubble induced to conventional gas cloud collapse; Dwarkadas et al., 2017; Forbes et al., 2021), though it is clear from Earth’s chemical content alone that the Solar system is made of recycled stellar material (Burbidge et al., 1957, and e.g. the production of gold via the *r*-process in merging neutron stars; Freiburghaus et al. 1999; Kasen et al. 2017). Hence, in the time before the Solar System’s formation, there must have been multiple cycles of stellar life and death to enrich the Galaxy with the observed chemistry.

Observations of galaxies at a redshift of $z \gtrsim 0.5^1$ – representing the cosmic epoch corresponding to the Solar System’s formation and earlier – reveal that the Universe was a much more energetic place. The star formation rate (SFR) at earlier epochs was orders of magnitude higher (see [Madau & Dickinson, 2014](#), for a review), and the initial mass function (IMF; [Salpeter, 1955](#)) of stars in this epoch preferred higher mass stars compared to the present day (as evidenced by a variable initial mass function slope with time; [Kroupa, 2001](#); [Li et al., 2023a](#); [Cullen et al., 2025](#)). The emerging picture is that the chemical content of the early Universe was primarily attributed to processes involving massive stars: their strong stellar winds ([Mujres et al., 2012](#); [Rivera-Thorsen et al., 2024](#)) and their eventual core-collapse supernovae ([Dahlen et al., 2012](#); [Schneider & Maiolino, 2024](#), the latter for a review on the history of dust production).

The dust production in our modern Milky Way and local Universe is supported by stars of all masses. In contrast to earlier times, asymptotic giant branch (AGB) and post-AGB stars – the evolved population of stars initially $\lesssim 8M_{\odot}$ ([van Winckel, 2003](#)) – are now a dominant producer of dust and metals ([Boyer et al., 2012](#); [Ventura et al., 2020](#)). This is in part simply due to the fact that there are more of these stars (due to the IMF dictating that more low-mass stars are formed) despite their longer evolutionary timescales. Still, there remains a modest population of massive stars that contribute material to the interstellar medium in broadly the same way that their younger-Universe counterparts would have – a key distinction being the effect of metallicity on stellar evolution and output.

The interstellar medium within the Galaxy tends towards higher metallicity over time, and so more recently formed stars will tend to have higher metallicities as a result ([Lian et al., 2023](#)). This has been suggested to be the root cause behind the IMF changing from top-heavy to bottom-heavy (preferentially forming high or low mass stars respectively) over time ([Chruslinska & Nelemans, 2019](#); [Sharda & Krumholz, 2022](#)). Not only does a changing metallicity affect the processes of star formation, but the lives of formed stars too. For example, stars in lower metallicity environments have been observed tending towards faster rotation rates, even approaching the critical rate ([Vink & Harries, 2017](#); [Ettorre et al., 2025](#)), which can enhance mass loss and interior mixing ([Mestel, 1953](#); [Maeder & Meynet, 2000](#)) and fundamentally change the eventual fate of the star. Enhanced mass loss can also take place due to the line-driven winds of evolved massive stars (Wolf-Rayet stars, discussed more in Section 2.2.1) where radiation pressure from emission lines results in extreme stellar winds and angular momentum loss ([Vink & de Koter, 2005](#); [Gräfener & Hamann, 2008](#); [Ud-Doula et al., 2009](#)). This loss of angular momentum inherent of more metal-rich stars is likely the dominant factor in a redshift-dependence of Long Gamma-Ray Bursts (LGRBs; [Woosley & Heger, 2006](#); [Lan et al., 2021](#)) arising from Wolf-Rayet stars via the collapsar model ([Woosley, 1993](#); [Detmers et al., 2008](#); [Sobacchi et al., 2017](#)), suggesting that these seldom occur in our present epoch. The dependence of stellar mass loss and angular momentum evolution on metallicity can therefore be the deciding factor on the type of supernova a star undergoes ([Boissier & Prantzos, 2009](#); [Pessi et al., 2023](#)), and the species of compact remnant – if any – left in its wake ([Heger et al., 2003](#)).

¹A lookback time of roughly 5 Gyr assuming a standard Λ CDM Universe

2.2 Dancing with the (Massive) Stars

We discussed in the previous section how metallicity can influence the evolution and fate of massive stars, although there is another physical factor which can alter their histories even moreso: the multiplicity of massive stellar systems (Sana et al., 2012). Binary systems are ubiquitous stellar laboratories offering valuable insight into a range of astrophysics including, but not limited to: testing General Relativity (Hulse & Taylor, 1975; Claret et al., 2010); mapping stellar surfaces (Oláh et al., 2025); stellar mass loss and nebula formation (Davidson & Humphreys, 1997; White & Tuthill, 2026); and mass transfer (Marchant & Bodensteiner, 2024). The multiplicity fraction of stars increases monotonically with stellar mass (even being as high as 80% for stars $\gtrsim 10M_{\odot}$; Duchêne & Kraus, 2013; Offner et al., 2023), and so studying binaries is essential to understand the behaviour of most massive stars.

Binary evolution of stars is reasonably well understood and readily modelled, but a majority of the most massive stars are in triple or higher-order systems (Sana et al., 2013). The dynamics of triple systems are inherently unstable² in a phenomenon known as ‘the three body problem’. The orbits of these systems may be quasi-stable – at least for a period of time – if they exist in a hierarchical configuration, where two stars are in a close ‘inner binary’ and the third star makes a wide ‘outer binary’ with the more compact system. Still, the third star will have a perturbative influence on the inner binary via the Kozai-Lidov mechanism (Toonen et al., 2016, and see Naoz, 2016, for a review). This manifests as a periodic oscillation in the eccentricity of the inner binary, even up to values approaching $e \sim 1$, and a mutual inclination oscillation between the outer and inner binaries.

With the orbital parameters of the inner binary changing as a result of the tertiary perturbations, the evolution of the inner binary stars is no longer predictable. Mass transfer is a common occurrence in close binaries that evolve asymmetrically, but the changing orbital behaviour of the inner binary in a hierarchical triple then means that mass transfer may occur even for wider binaries or at multiple phases over the system’s lifetime (Toonen et al., 2020). Further, the orbit in an isolated binary is often circularised before (or during) the mass transfer phase (Davis et al., 2013), but triple systems can retain eccentric orbits as a result of the perturbative influence of the tertiary (Toonen et al., 2020).

It is well understood that a tertiary star can radically change the stellar evolutionary history of the inner binary in a hierarchical triple, and the post-supernova remnant behaviour is similarly sensitive to a distant companion. Assuming that the inner-binary’s evolution results in a binary black hole (BBH), the subsequent merger time can be radically shortened (by many orders of magnitude) depending on the mass and orbit of the outer tertiary companion (Stegmann et al., 2022; Vigna-Gómez et al., 2025). Tertiary systems have also been proposed as progenitors of some of the most massive observed gravitational wave signals so far (Vigna-Gómez et al., 2021), and so the influence of a tertiary companion is present throughout the entire life-cycle of triple stellar systems.

²See the [ThreeBodyBot](#) for a number of visualisations demonstrating this.

2.2.1 Stellar Evolution, Turned up to $> 30M_{\odot}$

The journey of an evolving star is separated into distinct paths depending on whether the star is low ($\lesssim 8M_{\odot}$) or high (otherwise) mass. While low mass stars end their lives by transforming into a white dwarf through a planetary nebula phase (van Winckel, 2003), high mass stars explode as supernovae and leave a neutron star or black hole remnant. With that said, the evolutionary track of a star can be radically different even within each of these two wide mass classifications.

Massive stars, like all those on the main-sequence, spend the majority of their lives fusing hydrogen in their core. Once this hydrogen is depleted, their evolutionary progression is then a sensitive function of the stellar mass and other properties. Most stars of mass $8M_{\odot} \leq M \leq 30M_{\odot}$ will quickly evolve onto the red supergiant (RSG) branch, where the star inflates and cools while increasing in luminosity (Ekström & Georgy, 2025). Depending on the core-helium and envelope mass, stars may transition from RSGs to blue supergiants (BSGs), or if the star is massive enough it may directly evolve to a BSG after the main-sequence phase (Saio et al., 2013). The most massive stars, those that are $> 30M_{\odot}$ and rare due to the negative slope of the initial mass function (Kroupa, 2001), may skip the RSG and BSG phases altogether and evolve into a Wolf-Rayet star (Eldridge & Stanway, 2022; Marchant & Bodensteiner, 2024), one of the brightest and hottest class of star and one immediately preceding a supernova explosion.

Wolf-Rayet stars were first discovered as stars with emission line dominated spectra, notably from the elements helium, carbon, nitrogen and/or oxygen (Wolf & Rayet, 1867). Within the WR classification, there exist WN, WC, and WO subtypes to differentiate between the strengths of the nitrogen, carbon and oxygen lines respectively, and these emission lines are the primary drivers of these stars' mass loss (Castor et al., 1975; Crowther, 2007). In fact, these stars feature some of the strongest winds of any class of star (in both mass loss rates and wind speed) and these winds are sustained for $\gtrsim 10^5$ yr until the star eventually undergoes a hydrogen depleted core-collapse supernova explosion (De Marco & Izzard, 2017; Shenar, 2024). These stars undergo Type Ib/c supernovae as they lack hydrogen envelopes; how this hydrogen envelope – which makes up the majority of the stellar mass – is dispelled remains a topic of uncertainty, but is likely caused by intrinsic mass loss from the radiation-driven winds (the strength of which is metallicity dependent; Shenar et al., 2020), binary interaction, or some interplay between the two.

Many Wolf-Rayet stars evolve and die within binary systems. The multiplicity fraction, while dependent on WR subtype, is ~ 0.5 (although different methodologies have not yet converged on a single value Dsilva et al., 2020; Deshmukh et al., 2024), and so binary interactions play a large role in the final phases of these massive stars. Indeed, mass transfer from the primary onto the secondary in a binary system may be one mechanism by which hydrogen envelopes may be shed and WR stars formed (Shenar, 2024, and references therein). At low-metallicity, this mass-transfer may lead to more WR stellar formation where the secondary may otherwise have been too low-mass to independently evolve into a WR star (see the quasi-chemically homogeneous tracks in Figure 1 of Eldridge & Stanway, 2022). These discussed *intrinsic* interactions are for closely orbiting binaries, but *extrinsic* interaction can occur in the environment

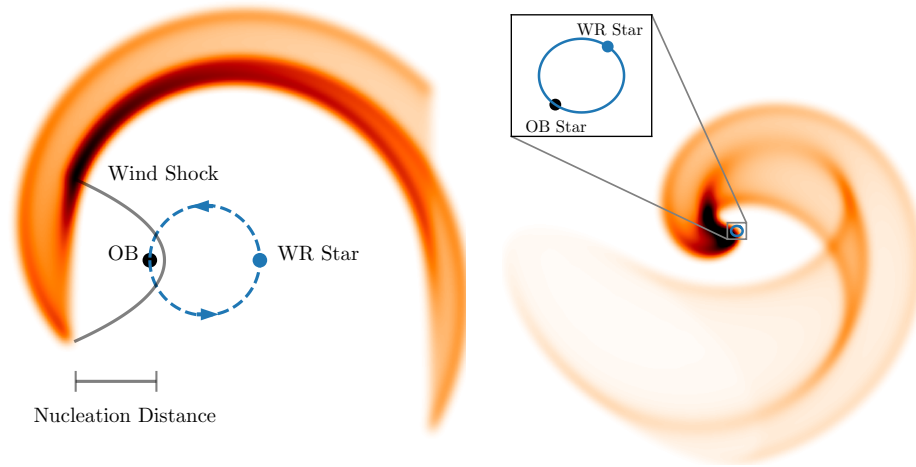


FIGURE 2.1: The wind-wind shock of Wolf-Rayet colliding wind binaries offers a shielded site for copious dust formation. The left figure shows a (not-to-scale) schematic of the processes involved in the dust production, where the WR wind overpowers that of the O star, dust is nucleated downstream of the shock front, and the orbital motion wraps the dust into a spiral. The right figure shows this process to a scale typical of these systems. Figure from White & Tuthill (2026).

far from the stellar surface. One such interaction, quite unique to WR stars, is the nucleation of sculpted dust shells from the colliding winds between the WR star and another massive companion.

2.2.2 Colliding Wind Binaries Hosting Wolf-Rayet Stars

Stars of all masses have stellar winds – a flow of material from the surface driven by the stellar luminosity and/or magnetic fields. For main sequence stars, there is a rough mass progression where more massive O or B type stars have a more intense wind, meaning higher mass loss rates and/or wind velocity (see Kudritzki & Puls, 2000, for a review). Although far off the main sequence, a defining characteristic of Wolf-Rayet stars is their uniquely powerful wind, and so WR stars in a binary with another WR or OB star will see the winds of each star collide where the WR wind overpowers that of its companion – these systems are known as Wolf-Rayet colliding wind binaries (Cherepashchuk, 1976; Prilutskii & Usov, 1976; and White & Tuthill, 2026, for our review).

Colliding wind binaries, even with main sequence stars, are known to be highly luminous non-thermal emitters. The wind collision between the two stars results in a bow shock where the wind is compressed and rapidly heated, where the turbulent shock front and wake present localised magnetic fields that may accelerate particles which give of synchrotron radiation (Rauw & Nazé, 2016). What makes WR CWBs unique compared to main sequence (or other classifications of) CWBs is dust formation; in almost all cases where a WC star has a massive WR/OB companion in a sufficiently wide binary (orbital periods of ~ 100 d or more), dust is very efficiently produced in

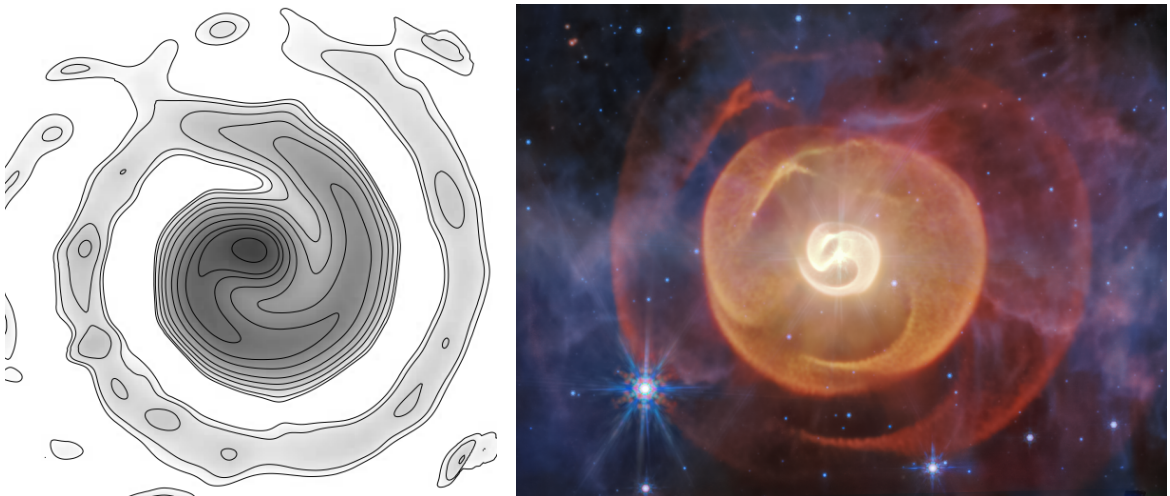


FIGURE 2.2: The spiral colliding wind nebulae have been observed for ~ 25 years now, where infrared imaging has developed significantly. *Left:* The first image of a WR CWB, here WR 104, taken with aperture masking interferometry from a ground based observatory (Tuthill et al., 1999). *Right:* The Apep triple system, composed of the only known WN+WC binary, as directly imaged with the space-based *James Webb Space Telescope* (STScI/NASA/ESA; Han et al., 2025; White et al., 2025).

the wake of the colliding wind shock. Here, the WC star provides an enriched wind full of carbon, the wind-wind shock compresses this wind, and turbulence from the shock creates regions of high density that shield the material from the ionising radiation of the hot binary. Figure 2.1 shows this phenomenology, where dust is nucleated sufficiently far down the shock front once the material has cooled, and orbital motion wraps the dust nucleation site (a surface along the conical shock) into a spiral.

Since the first images of colliding wind nebulae taken with aperture masking interferometry and poorly resolved direct imagery (Tuthill et al., 1999; Monnier et al., 1999; Marchenko et al., 1999), more of these systems have been imaged and better resolved. In the past 3 years, the *James Webb Space Telescope* (JWST) has imaged a notable subset of the WR CWBs, including WR 48a, WR 112, WR 125, WR 137 (Lau et al., 2024; Richardson et al., 2025, for the four systems mentioned so far), WR 140 (Lau et al., 2022; Lieb et al., 2025), and the Apep system (Figure 2.2, right side; Han et al., 2025; White et al., 2025). Each of these systems (with the exception of WR 125) had been imaged with ground-based instruments prior to the JWST mid-infrared direct imaging; on comparison, JWST imagery invariably reveals fainter and cooler dust extending to larger radii – dust that reveals the dynamical history of these systems going back even up to ~ 700 yr (as in the case of Apep). This history is recoverable from the concentric rungs of dust in these images, where each rung corresponds to a previous orbital period. This phenomenon is especially prevalent in the episodic dust producers; the WR+WR/OB binaries in these systems are on eccentric orbits where the conditions of dust formation change as a function of orbital phase such that dust is only produced in a narrow window of true anomaly near to the stars' periastron passage (White & Tuthill, 2026).

2.2.3 Apep

Although only a recent discovery, the WR+WR colliding wind binary Apep is quickly becoming one of the most closely studied systems on account of its puzzling characteristics. [Callingham et al. \(2019\)](#) cite the discovery of the Apep system, first noting it as an unusually luminous X-ray and radio source in the Galactic plane then corroborating it as a bright infrared object. High resolution spectra of the inner binary of the system confirmed it as the first and currently only known WN+WC binary (although not the only confirmed WR+WR binary, the other being WR 20a by [Rauw et al., 2005](#), which is composed of two WNh stars that are not classical WR stars), the evolutionary pathway of how to obtain such a configuration remaining unknown ([Callingham et al., 2020](#)).

The two WR stars in the Apep inner binary are known to have wind speeds of $v_{\text{WC}} = 2100 \pm 200 \text{ km s}^{-1}$ and $v_{\text{WN}} = 3500 \pm 100 \text{ km s}^{-1}$, although the proper motion expansion of the nebula is constrained to $v_{\text{dust}} = 1020 \pm 100 \text{ km s}^{-1}$. This discrepancy poses a problem in our understanding, as the dust expansion is expected to be coeval with the wind flow. In the past, this discrepancy has been suggested to be the result of a slow equatorial wind of one of the WR stars in the system, hinting at near-critical rotation and implying a future gamma-ray burst progenitor ([Callingham et al., 2019](#)). While this hypothesis has not been proven false, more recent results have favoured that the system is more distant than previously thought which may resolve this discrepancy (since the proper motion dust expansion is covariant with the system distance; [Han et al., 2025](#)). Radio modelling of the non-thermal emission from the inner binary also supports the anisotropic wind argument, although [Bloot et al. \(2022\)](#) relies on outdated parameters of the binary orbit which have recently been refined by JWST imaging and geometric modelling ([Han et al., 2025](#); [White et al., 2025](#)).

The first image of the Apep system not only revealed a complex dust nebula and two WR stars, but also a O8Iaf supergiant star that photobombed the image 0.7" to the north of the WR+WR binary. A similar line-of-sight dust extinction and presence of the same diffuse interstellar bands in the WR binary and the O star companion suggested that the O star is dynamically associated with the inner binary, although are not definitive tracers ([Callingham et al., 2019, 2020](#)). In contrast, radio non-detections of wind interactions between the WR binary and O star suggest that the stars are not associated ([Callingham et al., 2019; Marcote et al., 2021](#)). Despite this, we made a definitive association of the O supergiant to the WR+WR inner binary in [White et al. \(2025\)](#) on account of an imprint of interaction in the expanding dust nebula made by the O star. The exact mechanism by which the cavity is carved is not yet known, although we suggest in [White et al. \(2025\)](#), and in Chapter 5.2, that the cavity geometry is consistent with the expected geometry of a tertiary wind-wind shock assuming typical O8Iaf wind parameters. Despite the qualitative agreement in the modelling of the tertiary cavity, there remains a horizontal bar of dust in the northern region of the nebula which is not explained by geometric models. More rigorous modelling of the Apep nebula, e.g. with a hydrodynamics code, is sorely needed to understand the cavity formation and the presence of the bar, as well as determining whether the derived parameters of the system are consistent with the non-detection of radio emission of a tertiary shock.

2.2.4 Systems Beyond Our View

While we are able to obtain spectacular direct imagery for an increasing number of WR-CWBs, this directly observable population has a limit. At a high enough distance, the nebulae enshrouding these systems subtends such a small angle that even the most advanced infrared telescopes cannot resolve them. For these distant systems we then rely almost exclusively on their photometry and spectra to infer dust production. CWBs have been observed in X-ray photometry even as far away as M33 (Garofali et al., 2019), and optical interferometry may be a viable avenue to infer geometry for systems at intermediate distances (e.g. for WR 118; Millour et al., 2009). The most effective tool for distant dust inference, though, is observation of infrared light curves, where periastron passage for episodic dust producers facilitates a burst of dust formation that forms a prominent and periodic peak in the light curve. Williams (2019) finds evidence of many WR-CWBs in this way, including an episodic producer as far away as the Large Magellanic Cloud. In the same study, the light curve of an apparent twin to the prototypical WR 140 is discussed, a highly eccentric system with an orbital period of ~ 10 yr by the name of WR 19. As a caveat, though, many WR-CWB light curves are chaotic (e.g. CV Ser and WR 70; David-Uraz et al., 2012; Williams et al., 2013), and so any inferred parameters may be unreliable.

These light curves, going back decades for some prominent systems, motivate us to understand how the circumstellar nebula geometry influences the photometry of these systems. If a predictive light curve model were developed, we may, in principle, be able to infer the dust geometry and orbital parameters purely from the light curve of a system. Modelling these light curves involves emulating both the dust production rate and radiation transport within the system, and we describe in the next section the essential tools – conceptual and tangible – needed to create such a model.

Reign of love, I can't let go
 To the sea I offer this heavy load
 Locusts wind, lift me up
 I'm just a prisoner in a reign of love

Chris Martin, *Lovers in Japan*
 (*Coldplay's 'Viva La Vida'*)

3

Modelling Circumstellar Dust

Modelling the distribution and properties of circumstellar dust has provided insight into stellar dynamics, evolution, and more. Different modelling techniques offer insight into different areas of physics, so utilising a broad arsenal of models allows us to best form a complete picture of colliding wind binaries. In this chapter we introduce the various simulation and modelling techniques that we employ in this thesis, discussing the niches that they each fill and how they are relevant to CWBs.

3.1 Hydrodynamic Simulations

Fluid dynamics is ubiquitous across astrophysics; fluid flow is relevant at cosmological, galactic, stellar, and planetary scales, and there exist a vast body of hydrodynamical codes to simulate the evolution of such fluids. Simulating these fluid flows typically involves solving the equations of compressible hydrodynamics (Springel, 2010, for a review in an astrophysics context),

$$\text{Conservation of mass: } \frac{D\rho}{Dt} + \rho \nabla \cdot \mathbf{v} = 0 \quad (3.1)$$

$$\text{Conservation of momentum: } \frac{D\mathbf{v}}{Dt} + \frac{\nabla P}{\rho} + \mathbf{f}_{\text{mass}} = 0 \quad (3.2)$$

$$\text{Conservation of energy: } \frac{Du}{Dt} + \frac{P}{\rho} \nabla \cdot \mathbf{v} + \mathbf{f}_{\text{energy}} = 0 \quad (3.3)$$

although in many cases the equations of magnetohydrodynamics must be used¹ (MHD, which is out of the scope of this work). In these equations, ρ is the density of the fluid, \mathbf{v} the velocity vector, P the pressure, u the internal energy, and \mathbf{f} is an additional

¹The MHD equations describe the additional influence of electromagnetism on the fluid, relevant to e.g. compact objects or accretion disc simulations (among many other contexts).

function that can describe additional effects relating to the physical context (e.g. shock heating/cooling, self-gravity, etc). The Lagrangian time derivative,

$$\frac{D}{Dt} = \frac{\partial}{\partial t} + \mathbf{v} \cdot \nabla \quad (3.4)$$

is used in equations 3.1-3.3 as a convenience in computation so that all calculations are done in a comoving reference frame, compared to an Eulerian reference frame in which the velocity vector will be non-zero (and hence the rightmost term of equation 3.4 cannot be ignored).

The hydrodynamics equations, as they are in the form above, are not solvable without a defined equation of state (EOS) – a prescription of how the pressure of the fluid is coupled to one or more other state variables. The standard ‘ideal gas’ equation of state is given by

$$P = (\gamma - 1) \rho u \quad (\text{Ideal EOS}) \quad (3.5)$$

where γ is the adiabatic (or polytropic) index, or the ratio of the pressure-constant to volume-constant heat capacities of the fluid. If a thermodynamically reversible process is assumed (implying $f_{\text{energy}} = 0$ in equation 3.3), then using the ideal EOS with conservation of energy can yield the polytropic EOS (Price et al., 2018),

$$P = K \rho^\gamma \quad (\text{Polytropic EOS}) \quad (3.6)$$

where K is the polytropic constant of the material. In the special case of an isothermal problem where the temperature is constant – or alternatively locally isothermal, where the temperature is a function of position – the polytropic constant is given by the squared sound speed of the medium, and the EOS is then

$$P = c_s^2 \rho \quad (\text{Isothermal EOS}) \quad (3.7)$$

More generally, the sound speed of the medium is given by

$$c_s = \sqrt{\frac{\gamma P}{\rho}} \quad (3.8)$$

which applies for any chosen EOS. The choice of EOS can result in very different behaviour in a simulation, both quantitatively and qualitatively; it is therefore important to choose a physically plausible EOS for the phenomenon being modelled. For example, isothermal equations of state (or equivalently, ideal/polytropic EOS with $\gamma \sim 1$) have been used in hydrodynamical simulations of gas cloud collapse leading to star formation (Klessen et al., 2000; Mathew et al., 2023) since radiation is efficient at dissipating heat at the low densities associated with the beginning stages of collapse (Kuruwita et al., 2024, and references therein). Simulation of discs are commonly done with both isothermal (e.g. Flores-Rivera et al., 2020; Li et al., 2023b, for a protoplanetary disc and accretion disc respectively) and ideal/polytropic (e.g. Cecil et al., 2024; Rowan et al., 2025, for a protoplanetary disc and accretion disc respectively) equations of state. In contrast, modern hydrodynamic simulations seeking to model stellar winds typically use an ideal/polytropic equation of state (i.e. $\gamma > 1$; e.g. Siess et al., 2022; Vermeulen et al., 2025), which are more general across physical regimes (Johnstone et al., 2015).

Aside from the physical parameters pertaining to the context, the numerical integration scheme of the hydrodynamic code can influence the accuracy of the simulation too. Two principal hydrodynamic evolution methods have been widely adopted: grid-based codes and smoothed particle hydrodynamics (SPH) codes. Grid-based methods involve discretising the physical domain of interest into a number of grid cells on which the hydrodynamic equations are solved. Older codes employing this technique would often suffer from a lack of resolution due to static grids not adapting to time-changing regions of interest (e.g. that of a high contrast in state variables). This can sometimes be mitigated by performing the simulation in a co-moving frame of reference, but more modern codes will typically use some form of static or adaptive mesh refinement (Berger & Colella, 1989) to automatically resolve areas of high density contrast. These mesh refinement techniques involve partitioning a uniform grid into regions of higher resolution around points of interest. Static mesh refinement (a one-time division of the uniform grid) is a useful tool to reduce computational complexity compared to adaptive mesh refinement – especially when working in a comoving reference frame where regions of interest are more-or-less stationary (Abdi et al., 2024). More commonly used in astrophysics is adaptive mesh refinement (e.g. in the hydrodynamics code RAMSES; Teyssier, 2002), which periodically updates the structure of the mesh according to the spatial distribution of some state variable (e.g. the density) to dynamically track regions of contrast, albeit at a higher computational cost than static mesh refinement techniques.

Instead of manually or algorithmically deciding on spatial bounds in grid-based methods, the smoothed particle method involves using free-moving particles as interpolation points on which to solve the hydrodynamic equations. First introduced by Lucy (1977) and Gingold & Monaghan (1977), SPH involves evolving the positions of particles via equations of motion derived from the local particle density. There exist comprehensive descriptions of how this is done in published reviews about SPH (e.g. Monaghan, 1992; Springel, 2010; Price, 2012); in short, if particles have an identical mass and clusters of particles have a correspondingly high mass density – the density of the associated fluid is then

$$\rho(\mathbf{r}) = \sum_{b=1}^{N_n} m_b W(\mathbf{r} - \mathbf{r}_b, h) \quad (3.9)$$

where W is a smoothing kernel for the discretised mass packets onto a continuous domain, N_n is the number of neighbours around some test particle, m_b is the neighbour particle mass, and h is the ‘smoothing length’. The ideal smoothing kernel is a Gaussian function which is infinitely differentiable, but in practice a reasonably high-order B-spline function is used to reduce computational complexity (as a Gaussian would require interactions between all particles at once; see Price, 2012, for more detail). The smoothing length denotes the scale of the smoothing kernel and is inversely proportional to the number density of particles. The equations of motion of the particles are then derived from a reformulated version of the hydrodynamic equations incorporating this smoothed particle (and hence mass) density of the fluid. Since the particles are free-moving, SPH naturally resolves regions of high density contrast unlike grid-based methods (which suffer from low resolution, or higher computational cost with refinement); this makes SPH an attractive method for astrophysical phenomena involving

steep density gradients such as gas fragmentation or colliding winds (Price & Federrath, 2010).

Although hydrodynamic simulations are the state-of-the-art for most accurately modelling many astrophysical phenomena, their aim is (usually) not to directly reproduce observations. Doing so requires prohibitively specific initial conditions and a full account for all of the physics involved for the phenomenon. Still, hydrodynamic simulations have a proven track-record of reproducing the *macrostates* of observations, neglecting fine details of e.g. the exact position and structure of turbulent structure. For example, 2D simulations faithfully reproduced the rough flocculation of H₂ in the NGC 3132 nebula in De Marco et al. (2022), and 3D simulations are routinely used to study the fragmentation of matter on cosmic scales and to match statistical observations (e.g. in the Illustris simulation, Vogelsberger et al., 2014).

3.1.1 Hydrodynamic Simulations of Colliding Wind Binaries

Modelling colliding wind binaries presents unique challenges for hydrodynamic codes. The colliding wind shock itself is a large, three-dimensional region with extreme density contrast with respect to the surrounding winds of the two stars, requiring high resolution. The wake of the contact discontinuity then extends over orders of magnitude larger spatial scales, which would necessitate a low resolution simulation to reduce computational cost. Hence, modelling these accurately all but requires adaptive mesh or SPH codes.

Simulations of colliding wind binaries with numerical hydrodynamics codes were first performed in Stevens et al. (1992). Therein, the authors used a 2D grid code to study the cooling of the post-shock material within turbulent regions – similar studies since have included more realistic cooling prescriptions and monitored the close-in shock over a wider range of binary parameter space (Pittard, 1998; MacLeod & Loeb, 2020). Especially in early studies of CWBs, the binary systems are often simulated with no orbital motion to wrap the shock into a spiral (Pittard, 1998; Lamberts et al., 2011). This is usually to discern the fluid behaviour of the shock front itself, or to understand the sensitivity of the results to the physics assumed. Hydrodynamic studies of CWBs in the literature have been done with either isothermal or adiabatic wind flows, often with little or no justification for the choice, and Lamberts et al. (2011) investigated the effect of the EOS in a non-rotating CWB. For near-equal momenta winds, modelling with an isothermal EOS yields a thin shock front that is susceptible to ‘thin shell’ instabilities due to the EOS allowing higher compressibility in the fluid. This higher compressibility emulates efficient cooling in the shock, although the same phenomenology can be seen in adiabatic winds with additional cooling prescriptions (van Marle et al., 2011; Hendrix et al., 2016), and this behaviour can be sensitive to the mutual wind velocities and separation in the binary (van Marle et al., 2011).

While non-orbiting stars are useful to discern the effects of assumptions on a simulation, to attempt to model real CWB systems the orbital motion of the stars needs to be accounted for. We show in Figure 3.1 how the introduction of orbital motion affects the structure of the colliding wind shock, namely through the creation of a leading and trailing spiral arms of enhanced density. As a result of this orbital motion, the

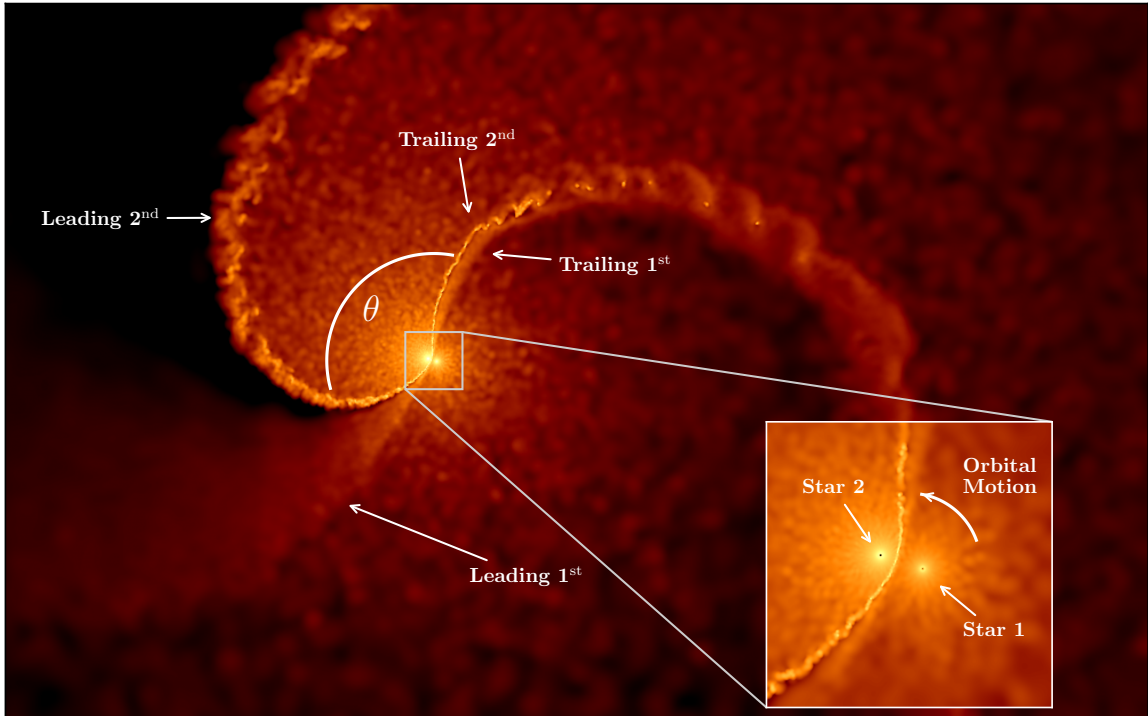


FIGURE 3.1: The structure of a colliding wind bow shock is sensitive to the orbital parameters and wind strength of each star. The higher momentum wind (here, that from ‘Star 1’) wraps the weaker wind (‘Star 2’) into a series of shocks where the wind momentum ratio determines the cone opening angle, denoted θ . The orbital motion of the binary can change the structure of colliding wind shocks, namely introducing a leading and trailing spiral arm which presents asymmetries in the post-shock conditions that are dependent on the material cooling. The contact discontinuity – the interface between each stellar wind along the shock – is analogous to the second shock here given the near-equal wind momentum ratio in this simulation (see Chapter 5 for more information). This figure is adapted from the data shown in Figure 5.1, and inspired by similar figures in [Lamberts et al. \(2011, 2012\)](#).

trailing arm tends to have higher post-shock densities and lower temperatures than the leading arm ([Lemaster et al., 2007](#)), and so the trailing arm generally provides more favourable conditions for dust formation ([Lamberts et al., 2012](#)); this effect has even been observed in real dusty CWBs ([Han et al., 2022](#)).

Simulating the nucleation of dust grains in colliding wind binaries, over spatial scales comparable to or larger than the binary orbit, is a challenging task. The creation of dust grains is known to occur in the highly mixed and cooled regions of the turbulent post-shock flow, and hence is very sensitive to the EOS used, the prescribed cooling functions, and the resolution of the simulation. There have been various methods used to emulate dust growth in hydrodynamic CWB studies, ranging from simple post-processing on a pre-completed simulation (e.g. [Soulain et al., 2023](#)) to integrating the physics within each run timestep (e.g. [Hendrix et al., 2016; Eatson et al., 2022](#)). The former option is computationally simple but does not account for the additional effects that dust formation can have on local cooling and density enhancement, which in turn

can lead to more or less dust nucleation. More recent studies have included numerical dust formation throughout hydrodynamic simulations, even taking into account the chemistry and grain-size distributions of the dust (Eatson et al., 2022; Siess et al., 2022).

The majority of publications seeking to model colliding wind binaries hydrodynamically have either neglected or loosely focused on recreating real systems. Broadly they opt instead to study how varying parameters affects the micro and macrostate properties of dust shells. The few real systems where a direct reproduction of observables has been attempted have mostly been of the ‘constant dust producers’ WR 104 or WR 98a (which have little or no orbital eccentricity; Lamberts et al., 2012; Hendrix et al., 2016; Soulain et al., 2023), with comparatively little attention paid to the ‘episodic dust producers’ with high orbital eccentricity. Modelling eccentric CWBs presents challenges in resolution, since the spatial scale of the shock changes over the course of each orbit. Despite this, some hydrodynamic simulations have been performed of η Carinae (Parkin et al., 2009; Madura et al., 2013), WR 140 (although not focusing on dust production; Russell, 2013; Reitberger et al., 2014), and WR 22 (to model the X-ray emission; Parkin & Gosset, 2011). More simulations of these eccentric dust producers are needed, as they offer a unique opportunity to compare theory and observation of colliding winds and subsequent dust nucleation simultaneously over multiple regimes. We found that the Apep system adds an additional layer of complexity and intrigue onto the conventional dusty CWB case via the inclusion of a third star offset from the inner binary orbital plane (White et al., 2025). Triple systems have seldom been modelled with hydrodynamic codes before, and so simulating a massive triple with two simultaneous colliding-wind shocks (see Malfait et al., 2024a, for a low-mass analogue of this) may reveal interesting phenomena.

3.2 Geometric Modelling

Hydrodynamic modelling of colliding wind binaries is a powerful tool for studying the conditions that lead to dust nucleation, provided that the properties of the binary stars are known *a priori*. When this is not the case, geometric models are a useful tool to use the observed spatial distribution of dust to infer the parameters of the stars that make it. These models approximate the behaviour of dust formation, typically assuming that dust nucleates in the colliding wind shock and then moves radially out of the system after formation. In order to couple this flavour of modelling with observations, though, direct imagery of CWBs is needed. Tuthill et al. (1999, Figure 2.2) revealed the first such image of a dusty CWB, WR 104, and used a simple one-dimensional geometric model to liken the observed ‘pinwheel nebula’ to an Archimedean spiral. Fitting these simple spirals to colliding wind nebulae requires that the system orbits almost exactly in the plane of the sky (i.e. the observer has a top-down view of the orbit), and a fully 3D geometric model is needed to recreate nebulae in other orientations. This kind of model – creating dust along the surface of a shock cone and then evolving its trajectory ballistically as the binary orbits – was introduced in Monnier et al. (2002), where the first direct images of WR 140 were presented.

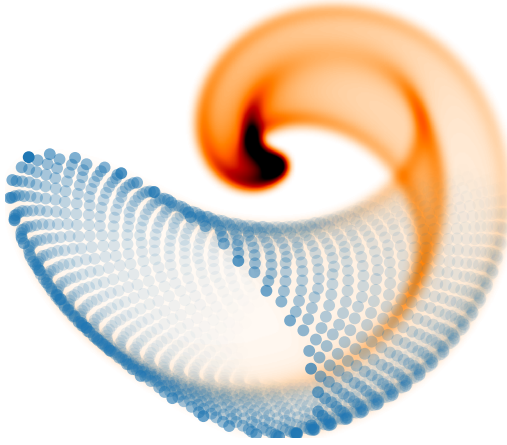


FIGURE 3.2: The basic idea behind the geometric model is to place a ring of discretised dust ‘particles’ along a 2D slice of the colliding wind shock front, and create a new ring for each timestep as the binary stars move in their orbits at the heart of the nebula. Since the shock front changes in position and orientation as the stars orbit, the particles get wrapped into a geometric spiral. An image of the projected nebula can then be created by taking the column density (i.e. a 2D histogram) of the dust particles after translating them to their true orientation in the plane of the sky. This plot represents the transformation from a point cloud of dust particles into a simulated column density image, from White et al. (2025).

Fast and feature-rich geometric models have been developed in the time since the first direct imaging of dusty CWBs. We describe in White et al. (2025) a geometric model that is orders of magnitude faster than previous analogues, and with more physically-motivated tweaks to the basic principle described in Figure 3.2. This, and recent models before it, are able to capture a plethora of observed and theorised phenomenology, including dust enhancement in the trailing edge of the shock (Han et al., 2022), dust modulation as a function of orbital phase when conditions are not favourable to nucleation (Williams et al., 2009; Han et al., 2022), and acceleration of the dust due to radiation pressure. Still, these models have so far neglected to include some theorised phenomenology which may impact the distribution and evolution of dust, namely the geometric skew of the shock front as a function of orbital true anomaly (since a changing orbital velocity can influence the orientation of the shock relative to the stars; Parkin & Pittard, 2008), and the thickness of the dust-forming shock front edges (to emulate the effect of thin shell instabilities as seen in e.g. van Marle et al., 2011).

Geometric models have been critical in inferring the binary parameters in many WR colliding wind binaries. One key reason for this is that the geometry of the dust plumes are often unique for a given set of orbit or system parameters; while degeneracies between parameters can still exist, these are usually for extrinsic parameters relating to e.g. the distance to the system (White et al., 2025). As such, a single spectrum (which can reveal the terminal windspeed of each of the stars in the binary; Callingham et al., 2020) and a single infrared direct image of the dust shells are usually enough to uniquely determine the system parameters; this has been done in WR 104 (Harries et al., 2004; Soulain et al., 2018), WR 112 (Lau et al., 2020), WR 137 (Lau et al., 2024), and WR 140 (Han et al., 2022; Lau et al., 2022). In cases where there remains ambiguity in the parameters after a single epoch of observation, continued monitoring over a fraction of the orbital period with a few more observing epochs can break degeneracies and offer a unique solution (as in the Apep system; Han et al., 2025; White et al., 2025).

3.3 Radiative Transfer

Hydrodynamic and geometric modelling of dust structures are useful to learn about the composition and distribution of dust grains, but often require shortcuts to be taken in making simulated images (of what one might see with a telescope). This is because these methods do not natively model radiation transport (also referred to as radiative transfer) – the process by which electromagnetic radiation is emitted, absorbed, and/or scattered within some medium (see Figure 3.3 for a graphical representation). Modelling this allows one to accurately determine the equilibrium temperature of gas or dust subject to an irradiating source(s). This process is governed by the radiation transport equation (Schuster, 1905; Schwarzschild, 1906; Chandrasekhar, 1950),

$$\frac{1}{c} \frac{\partial I_\nu}{\partial t} + \nabla I_\nu + (\kappa_{\nu,s} + \kappa_{\nu,a})\rho I_\nu = j_\nu\rho + \frac{\kappa_{\nu,s}\rho}{4\pi} \int_\Omega I_\nu d\Omega \quad (3.10)$$

where I_ν is the spectral radiance, $\kappa_{\nu,s}$ is the scattering opacity, $\kappa_{\nu,a}$ is the absorption opacity, j_ν is the emission coefficient, and ρ is the local mass density. In practice, equation 3.10 is most often solved under a series of assumptions that: the system is in a steady state (so $\partial I_\nu/\partial t = 0$), there is no back-scattering (so $\int I_\nu d\Omega = 0$), or even sometimes that there is no scattering at all (so $\kappa_{\nu,s} = 0$). Making these first two assumptions yields a simpler radiation transport equation,

$$\frac{1}{\rho} \nabla I_\nu = \mathcal{S}_\nu - (\kappa_{\nu,a} + \kappa_{\nu,s})I_\nu \quad (3.11)$$

where $\mathcal{S}_\nu = j_\nu/\kappa_{\nu,a}$ is the ‘source function’ describing how readily emitting the material is. This equation is easily solved in the 1D case, especially when assuming a ‘grey’ material whose properties are not frequency dependent (Hummer & Rybicki, 1971). Much of the development in the field of radiation transport was motivated by the need to understand radiation transport within the Sun, specifically the solar atmosphere. To a good approximation, the radiation transport here can be modelled with a static 1D plane-parallel atmosphere (i.e. ignoring the curvature inherent of a spherical body along with any radial expansion its material may have) with isotropic scattering and grey approximation, and hence has an analytic solution (Chandrasekhar, 1950). For modelling the entire radiation output from a star, especially early-type stars with extended photospheres, it becomes increasingly important to model the effect of curvature along the stellar surface with spherical symmetry (Peraiah, 1973) which can lead to e.g. limb darkening among other phenomena. This, too, has an analytic solution given the usual assumptions (Kosirev, 1934; Hummer & Rybicki, 1971).

The problem of radiation transport becomes quickly complex when these assumptions are no longer valid. For example, it is not analytically solvable for an anisotropic distribution of dust in 3D. To solve the radiation transport equation in these contexts, then, a Monte Carlo (MC) approach is needed (Metropolis & Ulam, 1949; Boisse, 1990; Lucy, 1999) which solves the radiation transport problem iteratively. The MC approach closely models the true physical process that takes place, where rays are traced along the line of sight through some optically thin medium, scattering and absorption (and subsequent thermal emission) being taken into account as the rays are traced. For a statistically large enough sample of these rays traced – essentially a large body of

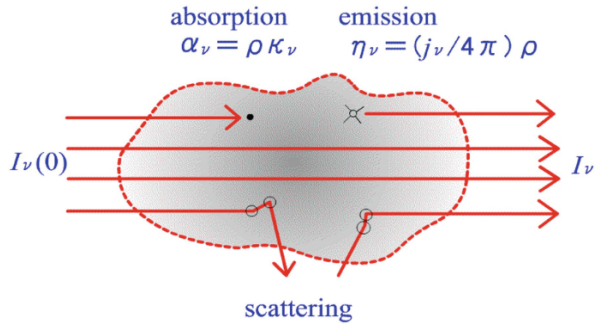


FIGURE 3.3: The radiation transport equation seeks to solve for the spectral radiance I_ν . With the Monte Carlo approach, rays are traced backwards through an optically thin medium, accounting for scattering, absorption, and emission effects that perturb what would be observed from an otherwise unobstructed light source $I_\nu(0)$. This Figure is from Kato & Fukue (2020).

sampled microstates across the spatial distribution of the astrophysical ‘image’ – an approximate image can be formed. The MC method forms essentially a hammer where all of the phenomena that limited early attempts at radiative transfer (e.g. anisotropic scattering, inhomogeneous opacities, etc) now become nails (see Noebauer & Sim, 2019, for a review on how MC radiative transfer has produced solutions for a range of applications). Intuitively, though, forming a large enough sample of traced rays through a potentially complex distribution is computationally intensive, hence the relatively recent development of the field in lockstep with Moore’s Law (Moore, 1965, which broadly predicts that transistors in a circuit doubles every two years).

The Monte Carlo approach natively performs very well when simulating dust distributed in e.g. discs/tori which have an analytic distribution and an axis of symmetry, and are easily mappable to a grid-based radiation transport solver. Output from SPH simulations (or geometric models) are not so easily mapped to a Cartesian grid due to their asymmetry in all axes and stochasticity in the position of each particle. To better resolve dense regions, adaptive mesh refinement has long been used to better resolve the radiation transport in dense regions while not wasting compute time on sparse regions (e.g. as in Harries et al., 2004). More recently, use of an unstructured grid via Delaunay or Voronoi tessellation has become the standard (Delaunay, 1934; Voronoi, 1908 and applications in Paardekooper et al., 2010; Camps et al., 2013, respectively). With these non-uniform tessellation methods, a grid is constructed that automatically follows the density contrast of the input particles and so the radiation transport can be modelled at the optimal resolution across the dust distribution.

Colliding wind binaries present a unique challenge for the radiative transfer problem. There are orders of magnitude ranges in space, media density, temperature, and opacity that need to be taken into account to appropriately model the systems. With the advent of the MC approach, radiative transfer codes have been used to infer dust properties of colliding wind binaries for almost as long as they have been modelled. The dust-producing WR CWBs are known to nucleate predominantly amorphous carbon dust – the unordered amalgamation of carbon atoms – and so the opacity and

emissivity properties of these grains are universally used in radiation transfer simulations of these systems (e.g. [Rouleau & Martin, 1991](#)). [Soulain et al. \(2023\)](#) used a radiative transfer code to recover the dust temperature in the environment around WR 104 as a post-processing step on a hydrodynamic simulation, in turn inferring the dust sublimation radius. A similar study was done on the η Carinae system, although looking at the ionisation fraction of hydrogen (since there is no carbon-rich WR wind in this system; [Clementel et al., 2014](#)). [Soulain et al. \(2018\)](#) used a radiative transfer code on a geometric model of WR 104 to study the surrounding dust mass and compare to observations. Simulating images of WR CWBs with a radiative transfer code has seldom been attempted, however. To date, there appears to be only two instances of this in the literature: [Harries et al. \(2004\)](#) simulates this on a geometric model of WR 104 to discern the amorphous carbon grain size distribution in the spiral nebula, and [Hendrix et al. \(2016\)](#) simulates this on a hydrodynamic model of WR 98a to predict what infrared and sub-millimetre telescopes might observe. This leaves radiative transfer on CWBs as a seldom explored and promising avenue for image simulation and light curve modelling.

The stars must be my friends
To shine for me

Christine McVie, *Never Forget*
(*Fleetwood Mac's 'Tusk'*)

4

Radiation Transport with Colliding Wind Binaries

As described in Chapter 3.2, there are a highly performant class of simulations that seek to use the orbital and stellar parameters of colliding wind binaries to generate their nebulae purely using geometry. Over the past 20 years, this has been a powerful tool to match theory to observations, but only to direct images of colliding wind nebulae taken in the mid-infrared where thermal dust emission shines. In this Chapter we introduce new ways that we can use geometric modelling to infer the physics of colliding wind binaries. We expand upon and use our code `xenomorph` (White et al., 2025) to be able to match output with upcoming data cubes and couple it with the radiative transfer code `MCFOST` (Pinte et al., 2006, 2009) in an effort to reproduce archival photometric data going back decades. The former tells us about the kinematic properties of colliding wind nebulae, and the latter describes the properties of dust which is so copiously dispersed into the interstellar medium by these systems.

4.1 Evolving `xenomorph`

The state-of-the-art in geometrically modelling colliding wind nebulae is the `xenomorph` code, introduced in our paper White et al. (2025). This code is written in the autodifferentiable Python framework JAX (Bradbury et al., 2018) and is highly performant due incorporation of Just In Time (JIT) compilation, meaning that a beginning-to-end point cloud construction takes a fraction of a second CPU-time. Not only is this code faster than its predecessors, but it comes packaged with more physics too, e.g. dust acceleration and wind anisotropy prescriptions. In this section we describe the modifications and expansions made to the `xenomorph` code to prepare for upcoming data (Section 4.1.1) and integration with a radiative transfer code (Section 4.2).

4.1.1 Velocity Slicing Nebulae

Taking a single image of a colliding wind nebula is incredibly useful and can sensitively constrain many orbital/wind parameters of the system alone. To constrain the remaining orbital or wind parameters, however, one would typically need many epochs of imaging to discern the evolution of the shells over time. Even with this, it can still be difficult to unambiguously determine some parameters which can be covariant and/or degenerate.

Another useful tool, should one have access, is a spectral data cube; not only are there two dimensions for mapping the spatial extent of dust emission, but a third dimension corresponding to the spectrum of each pixel. If a particular emission line within the gas coeval with the dust can be isolated, then the third dimension effectively encodes the radial velocity of the bright dust/gas. Such data cubes are commonplace in radio astronomy, and are becoming more readily accessible at shorter wavelengths in recent times via the Atacama Large Millimeter Array (ALMA; [Brown et al., 2004](#)), and even JWST ([Böker et al., 2022](#)). This data format is used to routinely observe and model the kinematics within e.g. protoplanetary disks ([Speedie et al., 2024](#)) and circumstellar dust structures around evolved stars ([De Beck et al., 2025](#)); while no data is yet public for a resolved colliding wind binary, WR 112 and Apep have now been imaged with ALMA. This type of observation is uniquely powerful for colliding wind binaries, since the obtained velocity structure is absolute (e.g. in units of km s^{-1}) rather than a relative and/or projected velocity structure which multiple epochs of direct imaging may give (e.g. in units of arcsec yr^{-1}). An absolute velocity structure would allow one to unambiguously determine the expansion properties and distance to the system using a forwards model (such as the `xenomorph` code) – a goal which is sorely needed to constrain the highly uncertain distance to these CWB systems (for an example, see the distance estimates within [Han et al., 2025](#), for the Apep system).

To prepare for the analysis of this new ALMA data once public, we expanded the `xenomorph` code to be able to sample the line-of-sight velocity structure of a generated nebula point cloud. The model already simulated the velocity structure in the backend, but we have now implemented a user-friendly frontend interface so that the velocity structure is easily accessible and comparable to observations. The interface partitions the particles based on a velocity grid, such that particles within some bound of radial velocity are sampled into discrete velocity bins. The user can specify simply a number of velocity bins in which they would like to divide the nebula into (in which case each velocity bin will have the same width, from the maximal receding to approaching velocities), or they can specify custom bins in which to partition the nebula. An example of the former is shown for 12 velocity bins of the WR 140 system in Figure 4.1.

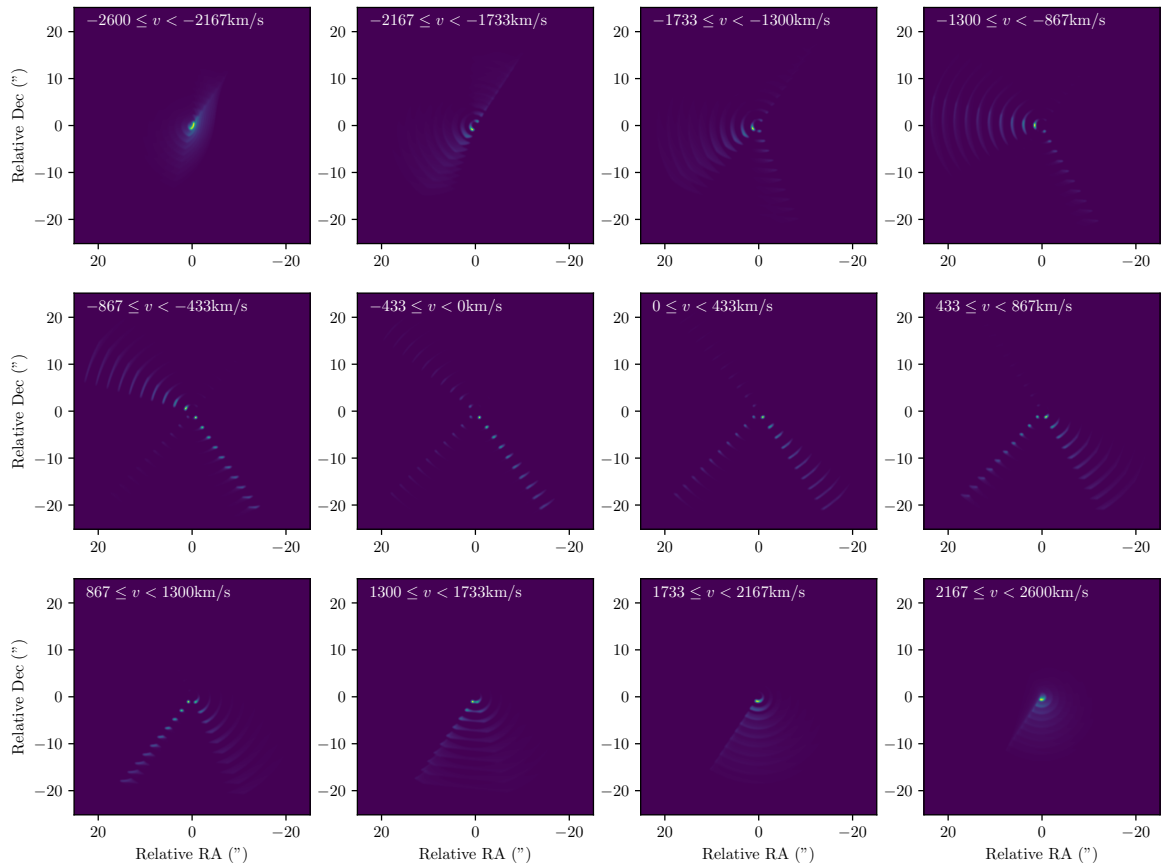


FIGURE 4.1: Each colliding wind nebula point cloud can be sliced into predetermined velocity bins, here for the WR 140 system. Panels going left-to-right, top-down gradually increase in line-of-sight velocity, where negative velocities are approaching and positive are receding, from the maximum receding to approaching velocity of the nebula. The nebulosity in each panel corresponds to the column density of point cloud particles, normalised to the number of particles in that panel. A worked example of how to generate this plot is available on the [xenomorph documentation page](#).

4.1.2 A Varying Dust Mass and Grain Size Distribution

Before we can make any photometric prediction of our modelled colliding wind nebulae with a radiative transfer code, we first need to model the dust properties within the nebula. Prior to the changes we detail in this section, the `xenomorph` code would make no estimate of the dust mass and grain size distribution evolution within each dust shell, only modelling the relative dust mass change as a function of geometry. In actuality, though, the grain properties within each comoving parcel of dust change over time; dust grains initially form out of a few atoms and have low mass, they tend to accrete more carbon as time goes on (increasing their grain size and mass), and may eventually be subject to destruction mechanisms that regress their state. This phenomenon has been qualitatively discussed previously, e.g. in Williams et al. (2009); Williams (2011), although a model linking CWB dust mass or grain-size distribution to its age has not been attempted to our knowledge. We propose here, for the first

time, prescriptions to emulate the time-varying dust mass and grain-size distributions within a colliding wind nebula.

To define the mass of each dust parcel within the nebula, we propose the use of a modified surge function. A surge function is mathematically simple – we propose a function that is parameterised by just three constants – and traces the expected shape in mass with respect to time that a single dust parcel (or a point in or geometric point cloud) would have. Williams (2011) describes a steep initial incline in dust mass as grains accumulate carbon, then a gradual fall-off over time as the grains no longer accrete mass (due to the decrease in the medium density) and are instead subjected to the ionising radiation of the stellar binary. A visualisation of the general functional form we use to describe the changing mass over time is shown in Figure 4.2. We begin our derivation with a basic form of a surge function parameterised by the age of the dust parcel, t ,

$$m_d(t) = (t - d_d)e^{-(b_d t - d_d)} + c_d \quad (4.1)$$

which is physically meaningful when $b_d > 0$ ($b_d \leq 0$ has the dust mass increasing indefinitely). Broadly speaking, the parameter b_d dictates how slowly the dust mass changes as a function of time (or equivalently orbital phase); higher values of b_d result in a later peak and a more gradual rise/fall off. The parameter c_d influences the function mainly by choosing the terminal dust mass (i.e. as $t \rightarrow \infty$), although it does slightly change the position of the function peak in time (orbital phase) and its slope albeit not as strongly as b_d . Finally, d_d is a horizontal shifting constant. Naturally, we expect the dust mass in any parcel to be 0 initially and so d_d is evaluated on the condition that $m_d = 0$ when $t = 0$, which transforms equation 4.1 into a non-linear equation that can be solved analytically with the (principal index) Lambert W function given c_d ,

$$d_d = W_0(c_d) = \frac{1}{\pi} \int_0^\pi \ln \left(1 + c_d \frac{\sin z}{z} e^{z \cot z} \right) dz \quad (4.2)$$

which is defined for $c_d \geq 0$. Rather than implementing our own numerical integrator, we use the fast SciPy (Virtanen et al., 2020) Lambert W implementation within our code to calculate the value of d_d .

In its current form, equation 4.1 can take on almost any range of values. To link the output of this equation to a desired dust mass, we must first normalise the equation to be between 0 and 1 and then multiply by a user-defined *maximum* dust mass to yield physical units. We normalise the equation by finding its peak value and dividing by that. Since equation 4.1 is a surge function, the maximum value corresponds to the turning point $dm_d(t)/dt = 0$. Taking the time derivative of the earlier equation gives

$$\frac{dm_d(t)}{dt} = \underbrace{e^{-(b_d t - d_d)}}_{\text{term 1}} \underbrace{(b_d d_d + 1 - b_d t)}_{\text{term 2}} \quad (4.3)$$

where our requirement that $dm_d(t)/dt = 0$ implies that either term 1 or term 2 are equal to 0. Since the exponential term will only approach 0 (as $t \rightarrow \infty$, and never being equal to it), term 2 must be equal to 0 at the function maximum. Hence the maximum value, t_{\max} , occurs at

$$t_{\max} = d_d + \frac{1}{b_d} \quad (4.4)$$

with the maximal value of the function found by substituting t_{\max} into equation 4.1, yielding

$$m_{d,\max} = \frac{1}{b_d} e^{-(b_d d_d - d_d + 1)} + c_d \quad (4.5)$$

Therefore, a normalised alternative to equation 4.1 is $\hat{m}_d(t) = m_d(t)/m_{d,\max}$, and the physical dust mass, M_d , can be found by multiplying this normalised equation by the true maximal mass of dust, $M_{d,\max}$,

$$M_d(t) = M_{d,\max} \left(\frac{m_d(t)}{m_{d,\max}} \right)^{\beta_d} = M_{d,\max} \left(\frac{(t - d_d) e^{-(b_d t - d_d)} + c_d}{\frac{1}{b_d} e^{-(b_d d_d - d_d + 1)} + c_d} \right)^{\beta_d} \quad (4.6)$$

where d_d is calculated as in equation 4.2 using the value of c_d . We also introduce a constant β_d which can take on values 0 or 1, where the user might choose to set $\beta_d = 0$ if they do not want to model the evolution of dust mass with respect to time (and hence the dust mass of all particles will be the same before the applied weighting scheme in `xenomorph`); except where otherwise stated, we will usually take $\beta_d = 1$ so that the dust mass evolution is simulated.

In these equations, t is in units of orbital periods. We initially explored a parametrisation based on orbital phase rather than time, but dust rings are often generated prior to periastron passage (i.e. as the stars are approaching each other), and so the dust mass ascribed to each ring would be inconsistent using the proposed formalism. Parameterising the ring mass based on its age (time) allows consistency no matter where the rings are generated within the orbit.

Due to the normalisation scaling applied within equation 4.6, the limiting dust mass is no longer simply c_d . Taking the limit of the equation as $t \rightarrow \infty$ yields

$$\lim_{t \rightarrow \infty} M_d(t) = \frac{M_{d,\max} c_d}{\frac{1}{b_d} e^{-(b_d d_d - d_d + 1)} + c_d} \quad (4.7)$$

which describes the dust mass of the nebula in the limit where the stars no longer have a significant effect on the dust grains e.g. via photodissociation, and when the dust density is no longer high enough for efficient grain sputtering.

For the same reason we expect the mass of each dust parcel to change with age, so too should the grain size distribution within that parcel evolve. The size distribution of comoving dust grains is typically modelled in radiative transfer codes as a power law on grain size, a ,

$$N(a) \propto a^\alpha \implies \frac{d \log N(a)}{d \log a} = \alpha \quad (4.8)$$

with a constant exponent α . One might expect though, looking over as broad a spatial scale as we are around colliding wind binaries, that the grain size distribution should depend on the environment that the dust parcel is in. For example, very close to the binary – where dust is only just nucleating – we might expect the grain size distribution exponent to be very negative so that there are many more small grains than large grains. As individual grains accrete more carbon – ageing dust grains – we might then expect the distribution to peak at some more positive exponent so that there are now more

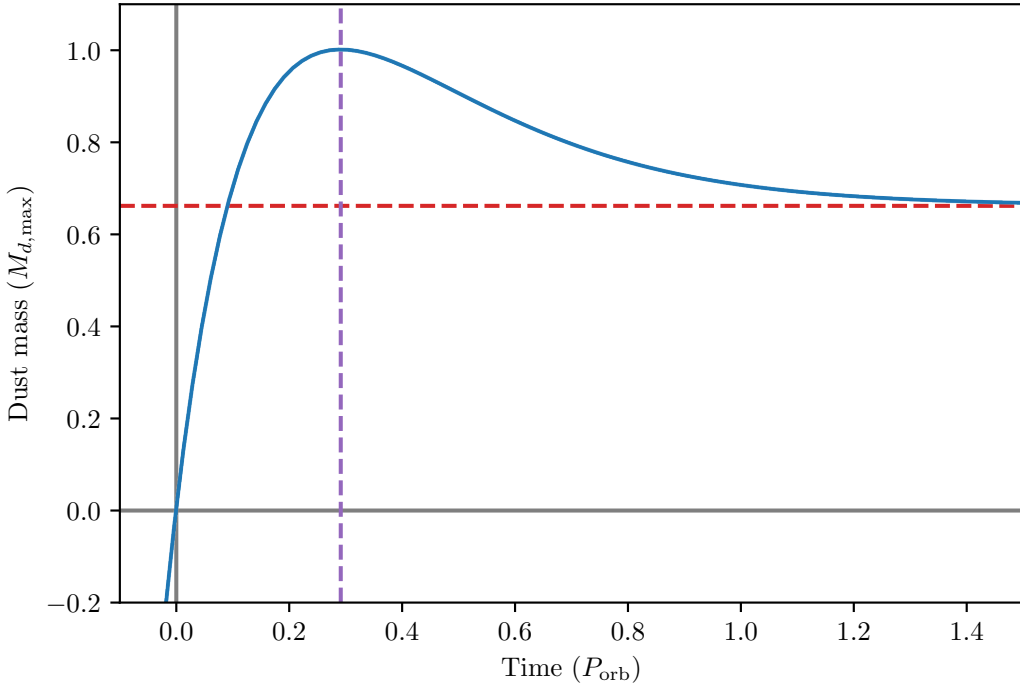


FIGURE 4.2: The form of our modified surge function describing the mass of a dust parcel over time quickly increases to a maximum after $t = 0$, then exponentially falls off to a terminal value. The blue curve here shows the output of equation 4.6, setting $b_d = 5$ and $c_d = 0.1$. The time of maximum mass, as calculated by equation 4.4, relies on a single parameter and is shown by a vertical purple line. The horizontal red line shows the terminal dust mass value as calculated by equation 4.7.

large grains than before. By the same notion that we expect the mass of each dust parcel to eventually decrease as it ages – via grain sputtering and photodissociation – we should then expect the grain size distribution exponent to get slightly more negative so that there are now relatively more small grains compared to the maximal dust mass. Hence, we can model the grain size distribution exponent with a modified surge function, just as we did with the dust mass. We propose a modification to equation 4.6 to now describe the grain size distribution exponent as a function of dust parcel age:

$$\alpha(t) = \alpha_{\text{max}} \left(\frac{(t - d_g)e^{-(b_g t - d_g)} + c_g}{\frac{1}{b_g}e^{-(b_g d_g - d_g + 1)} + c_g} \right)^{\beta_g} \quad (4.9)$$

This new equation has analogous but distinct constants, b_g , c_g , d_g , α_{max} , and β_g , but here we note that we allow d_g to be a free parameter; where we imposed $M_d(0) = 0$ as a physical condition before, $\alpha(0)$ can in principle take on any value and so the user must define d_g rather than calculate it using the other parameters.

In practice, radiative transfer codes are run with a single grain size distribution exponent that encompasses all of the circumstellar dust. In other words, a single grain size distribution is assumed to hold for the entire colliding wind nebula, despite the expectation that distribution is strongly dependent on the local conditions. To emulate some degree of the true physical process, we still model the parcel-specific exponents

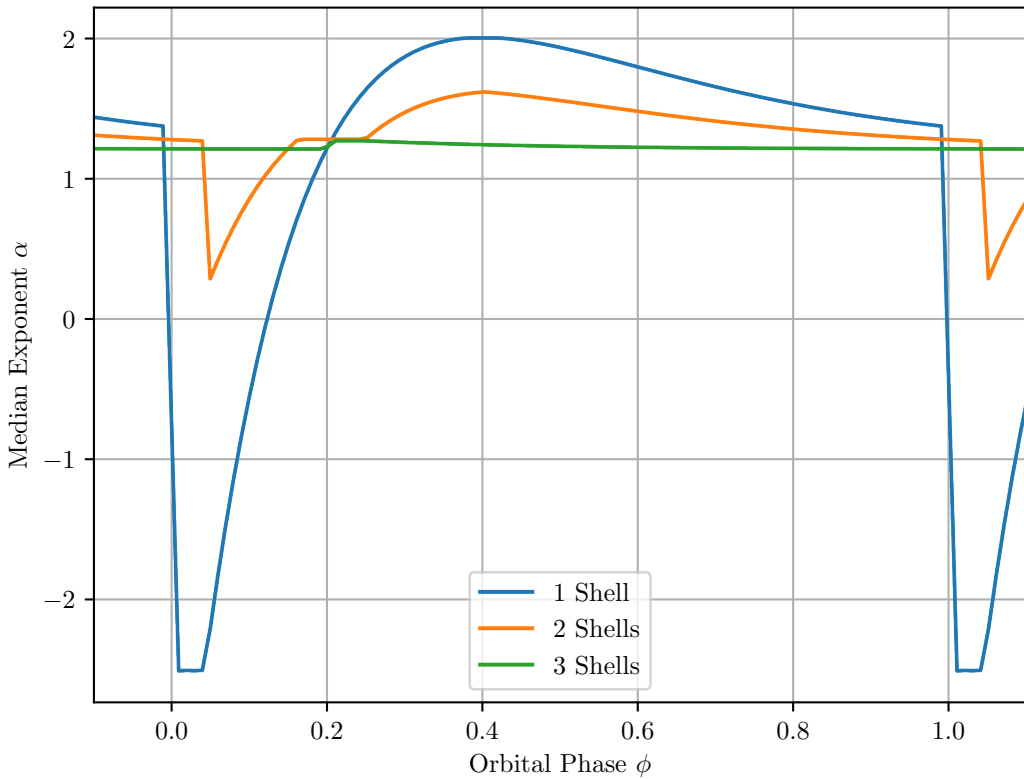


FIGURE 4.3: Taking the median value of the particle grain size distribution exponents across the entire nebula point cloud results in a changing value with phase as new dust is created and older dust ages. The profile of this curve is heavily dependent on how many shells are being simulated at once, since more shells equates to more old dust and hence a median exponent skewed towards the terminal value of equation 4.9. Each of the curves here are generated with $b_g = 5$, $c_g = 0.05$, $d_g = 0.2$, and $\alpha_{\max} = 2$.

across the nebula, but then feed the median exponent of all the points in the point cloud into the radiative transfer code. For episodic dust producers in particular, this results in an orbital-phase-evolving macroscopic exponent as new dust is created and older dust ages which will capture some of the true physical process. An example of this is shown in Figure 4.3 for the WR 140 system.

The utility of this fix depends strongly on the goal of the radiative transfer simulation. As we show in Figure 4.3, the magnitude of the exponent shift over an orbit is heavily dependent on the number of shells simulated; naturally, simulating more shells means there will be a higher proportion of old, dispersed dust that is now barely evolving over time. Hence, the change in median of the exponents across the point cloud will be damped as the shell number increases. Therefore, having an evolving dust grain distribution with orbital phase will only be relevant for simulating colliding wind nebulae at lower wavelengths; the dust temperatures associated with mid-infrared thermal emission are held for several consecutive shells, even in long period systems like Apε Han et al. (2025), and so many shells need to be simulated to properly reproduce observed luminosities. In contrast, near-infrared emission is typically only produced

from the innermost shell of colliding wind nebulae as the dust forms and very quickly cools, and so an evolving grain size distribution should be important for photometry in e.g. only the H and K bands and especially for systems near periastron.

4.2 Radiative Transfer with MCFOST

In my Honours work (White et al., 2024), I introduced a way of generating approximate light curves using `xenomorph`. This was done by rendering an image of the nebula point cloud, taking a subset of pixels with the highest surface density, then rationalising that this was directly proportional to the infrared luminosity of those pixels. Although highly performant, there are many problems with this approach. Firstly, the ‘brightness’ output is not in any physical units which makes it dubious to compare to real observations. Secondly, there is no wavelength information in this framework; in actuality, the profile of the light curve of any CWB can change dramatically depending on the portion of its spectrum, and so to accurately reproduce an infrared light curve, the temperature of the luminous dust cannot be ignored. Hence, for anything more than a quick and rough consistency check, the temperature structure of the circumstellar dust and the radiation transport needs to be simulated with a radiative transfer code.

In this work we use the widely-used and well-tested radiative transfer code MCFOST (Pinte et al., 2006, 2009). MCFOST is a Fortran based code that implements the Monte Carlo and ray tracing approach to radiative transfer, allowing the temperature structure of circumstellar dust to be calculated and subsequent images made according to the thermal emission and photon scattering of this dust. There are plethora published radiative transfer codes for use in astrophysics, but many are closed-source or designed specifically for a given purpose (e.g. cosmological simulations). Of the open-source, performant codes in the stellar astrophysics literature, MCFOST and RADMC-3D (Dullemond et al., 2012) stand out as the most widely used and tested, where either give effectively the same result for any given simulation (see e.g. Mignon-Risse et al., 2020, for comparisons). We opted to use MCFOST since it has a recently updated implementation of Voronoi tessellation which is needed in order to couple the radiative transfer code with the unstructured set of points produced by `xenomorph`. RADMC-3D similarly has implementations of unstructured meshes, although in an experimental build which at the time of writing has not been updated for years, compared to the release build of MCFOST that was last updated on a timescale of months.

4.2.1 Simulating and Processing Radiative Transfer Models

The MCFOST code is run by calling functions on the command line with specific arguments, and hence cannot be natively interfaced with a Python package like `xenomorph`. In this Section we describe our work in developing a new `xenomorph.mcfoст` module that marries the two codes making for a more accessible user-experience.

Integrating `xenomorph` and MCFOST

At the beginning of any `xenomorph`/MCFOST run, the nebula point cloud is generated as normal. MCFOST takes this distribution of points as a pre-saved Flexible Image

Transport System (FITS) file, where the primary Header Data Unit (HDU) is a 1-dimensional array of all of the ordered particle masses. We calculate these masses according to equation 4.4, where we multiply the first-pass dust masses by each particle weight. The image HDU in the FITS file is the 3-dimensional point cloud given in Cartesian coordinates. **MCFOST** then uses `voro++` (Rycroft, 2009) to perform the Voronoi tesselation using this point cloud.

A parameter file – containing all of the information about the circumstellar dust, radiation sources, and simulation specifics – must also be supplied to **MCFOST** at runtime. All simulations are run with the Radiative Equilibrium plus Local Thermal Equilibrium (RE+LTE) approximation¹; in the vast majority of cases this is a reasonable assumption, except possibly during intense dust formation when dust is being freshly nucleated (where there may in truth be large temperature gradients across each dust parcel). In addition, Lau et al. (2023) finds that there may be comoving populations of dust with distinct grain sizes and temperatures, implying that local thermal equilibrium may not always hold, although it is not clear exactly how or if this would affect a light curve. The dust produced from our objects of interest, Wolf-Rayet colliding wind binaries, is overwhelmingly amorphous carbon (see e.g. Han et al., 2025; Lau et al., 2023), and so we simulate one species of dust in **MCFOST** with the prepackaged amorphous carbon optical indices from Rouleau & Martin (1991). Although set to be user customisable in our Python wrapping, the minimum and maximum grain sizes are usually set to 0.001 and 0.5 μm respectively, simulating $n_{\text{grains}} = 100$ grain sizes in the distribution between these bounds (across log space). As discussed in Section 4.1.2, **MCFOST** cannot spatially differentiate grain sizes, and so the chosen grain size distribution exponent α applies to all of the circumstellar dust at once; we calculate this according to equation 4.9 as explained previously. Finally, the porosity of the carbon grains can affect the temperature profile and subsequent spectrum of circumstellar dust (see Kirchschlager & Wolf 2014 or Potapov et al. 2025 for a review on dust porosity). Most studies on astrophysical grain porosity have focused on the interstellar medium, and so the dust porosity from newly nucleated amorphous carbon in a colliding wind binary is ill constrained, hence we fix a fiducial porosity value of 0.2.

The temperature structure of the circumstellar dust is computed based on the radiation transport from one or more irradiating sources – stars – as described in the parameter file. We add parameters for each star in a specified system to this parameter file, specifically the stellar temperature and radius. **MCFOST** uses the temperature and radius to then calculate the luminosity of each star using the Stefan-Boltzmann law,

$$L = 4\pi R^2 \sigma T^4 \quad \Rightarrow \quad R = \sqrt{\frac{L}{4\pi\sigma T^4}} \quad (4.10)$$

where σ is the Stefan-Boltzmann constant. The photospheric radii of WR stars are not well constrained, though their luminosities are usually known more precisely. Hence, we take the luminosity of these stars from the literature and convert that to a radius using the rightmost equality of equation 4.10 to feed into **MCFOST**. The spectrum of each star is modelled as a blackbody curve given the stellar temperature, since detailed

¹We note too that **MCFOST** currently does not support NRE or NTLE runs with a supplied unstructured density grid.

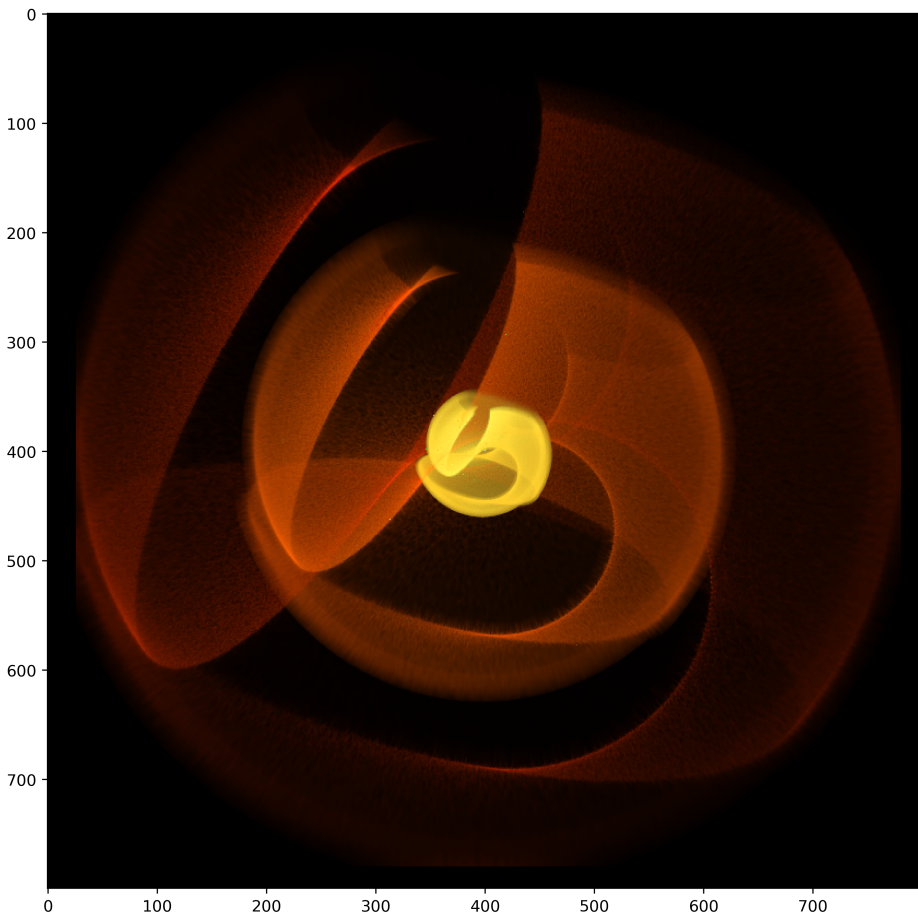


FIGURE 4.4: To validate that the radiative transfer works as expected, we simulated an 800×800 pixel image that mimics the Apε JWST clearly showing 3 concentric shells. The process to make this RGB is as described in the text.

spectra do not come prepackaged within MCFOST for Wolf-Rayet stars. Finally, each of the radiation sources are set to be in the geometric centre of the colliding wind nebula; the separation between the stars is typically orders of magnitude smaller than that of the stars to the circumstellar dust, and so this should have negligible impact on the temperature structure of the nebula.

For every simulation of the nebula luminosity, two MCFOST calls must be made: the first is to compute the temperature structure and the second is to create a ray-traced image. The total flux for the nebula can then be found by summing the flux over all of the pixels in the produced image. Since ray-tracing is a fundamentally random process, we need to evaluate that the integrated flux has converged to a single value given the image resolution and number of injected photons, n_{photons} . To make a light curve of each CWB, we care only about the photometry and not necessarily the fine details of each nebula, hence we set the resolution of simulated images to 30×30 pixels. Given this image resolution we find that $n_{\text{photons}} \sim 2 \times 10^7$ yields a converged flux with a random fluctuation of order 0.1% of the total flux for most systems (specifically for a total dust mass of $\lesssim 10^{-8} M_\odot$). In systems where the dust mass may be higher, factors of a few more photons should be injected. Similarly, if a high resolution image

of a colliding wind nebula is desired, with orders of magnitude more pixels (see e.g. Figure 4.4), orders of magnitude more photons are needed.

As a proof of concept, we show in Figure 4.4 a high resolution RGB image of the innermost 3 shells of the Apep system. This was generated as a comparison to the RGB image of Apep as seen via JWST in Figure 2.2. Hence, we mapped the blue channel to $7.7\text{ }\mu\text{m}$ emission, the green to $15\text{ }\mu\text{m}$, and the red to $25.5\text{ }\mu\text{m}$, with a logarithmic scaling function applied. This was done using the Lupton et al. (2004) algorithm implemented within the Astropy package (Astropy Collaboration et al., 2013, 2018, 2022). For each channel, 5×10^9 photons were used – totalling about 450 CPU hours for the RGB image – so that the edges of the Voronoi mesh were sampled with a high enough resolution to avoid visual artefacts. This RGB image well-reproduces the phenomenology of the actual JWST composite, and is an important consistency check for the more numerical modelling done with our `xenomorph-MCFOST` integration.

Broadband Filters

Ground-based infrared astronomy is done by looking in wavelength bands that are translucent to atmospheric water. The naming of these bands follows a progression in wavelength, where the K band allows through lower wavelength light than the M band, for example. In the context of our dust-producing colliding wind binaries, we should care about those bands that trace thermal dust emission, i.e. whose wavelengths correspond to blackbody emission of $\lesssim 2000\text{ K}$ (corresponding to about $1.5\text{ }\mu\text{m}$ and higher). Hence, in this work we focus on the infrared H, K, L, and M bands, and we describe some of their properties in Table 4.1.

Radiative transfer models with MCFOST are calculated at a single wavelength, and so to emulate what one might truly observe over an infrared band we must generate integrated fluxes at a series of points across the bandwidth and integrate these according to the sensitivity of the band at each wavelength. This means that several calls to MCFOST must be made for each individual band, and so to reduce computational cost we want to sample as few representative points across the band transmittance curve as possible. We show our sampled points of the transmittance curve for each of our four

Filter	Central	Full Width at	Zero-Mag Flux
	Wavelength (μm)	Half Maximum (μm)	($\text{W m}^{-2}\text{ }\mu\text{m}^{-1}$)
H	1.65	0.3	1.12×10^{-9}
K	2.2	0.4	4.07×10^{-10}
L	3.45	0.5	7.3×10^{-11}
M	4.8	0.5	2.12×10^{-11}

TABLE 4.1: In our code we consider four of the most commonly used infrared filters with which to simulate light curves. We show here key parameters for each filter, where detailed transmittance curves are shown in Figure 4.5. The data here are sourced from the filters on board the UK IR Telescope and NSFCam.

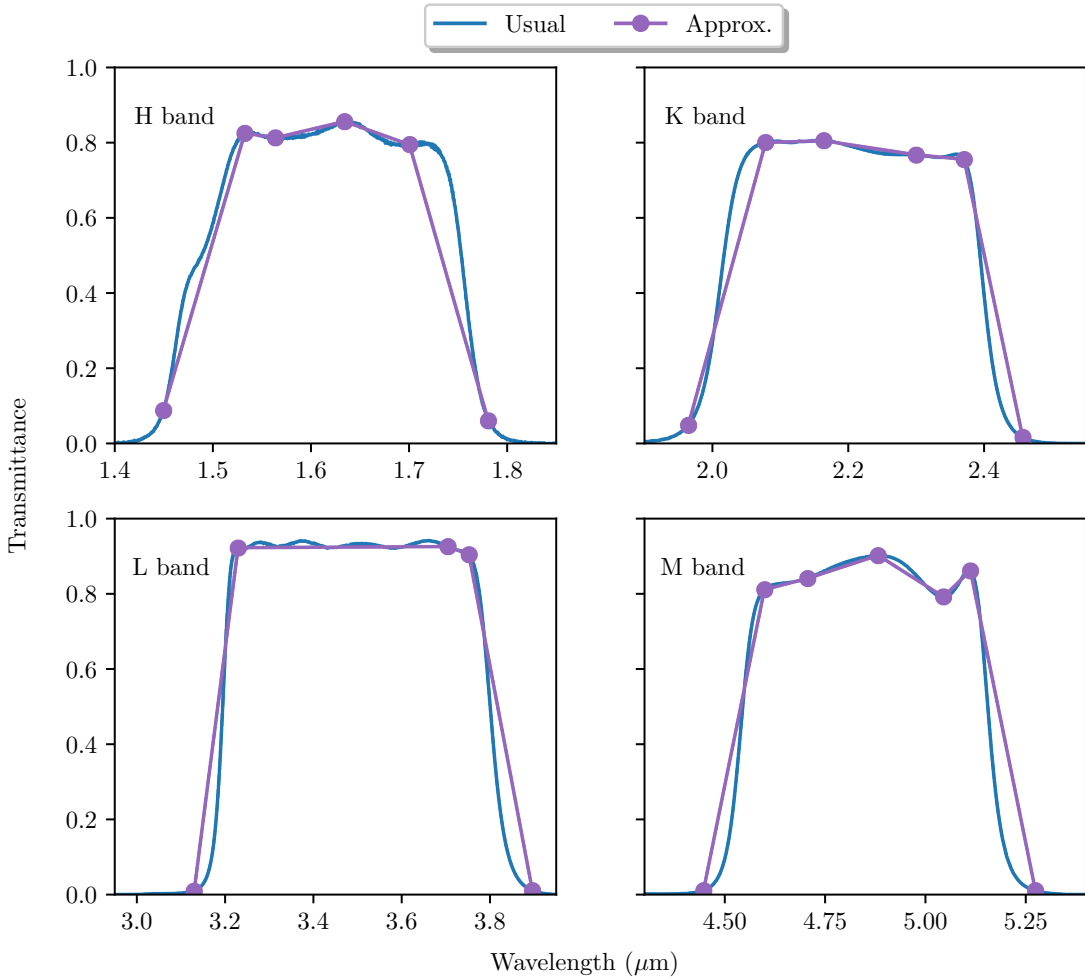


FIGURE 4.5: We generate images of our colliding wind nebula at several characteristic points across the bandwidth for each of the four chosen filters. The blue curves show the highly sampled transmittance curves of the H, K, L, and M bands, where the purple markers are the sampled wavelengths on these curves that approximately reproduce their characteristic shape, which we then generate images at. The band transmittance curves are those of the NSFCam filters, though they will be similar for other instruments too.

infrared bands in Figure 4.5. To calculate the total flux across the band, we integrate the weighted specific fluxes over the band divided by the integral of the transmittance curve,

$$F = \frac{\int_{\lambda_l}^{\lambda_h} F_\lambda(\lambda) T(\lambda) d\lambda}{\int_{\lambda_l}^{\lambda_h} T(\lambda) d\lambda} \quad (4.11)$$

using the trapezoid rule. Most flux values are quoted in terms of magnitudes, however, and we can convert from the integrated flux to an apparent magnitude by use of the zero-mag fluxes in Table 4.1 with

$$m = -2.5 \log_{10}(F) + 2.5 \log_{10}(F_0) \quad (4.12)$$

Calculating fluxes of what one might observe through an infrared band is important

when comparing to observations. Depending on the dust properties (mass, distribution, grain sizes, etc), the proportion of energy emitted by the stars versus the dust over the bandwidth can change by 10s of %. Being accurate in this way comes at a 5-10 times increase in computational cost, though, and is not necessarily needed when performing parameter space explorations; this can be done at a single wavelength to see the broad behaviour of light curves as individual parameters pertaining to the stars or nebulae are changed.

4.2.2 Light Curve Parameter Space Exploration

With the pipeline to generate light curves successfully built, we now turn our attention to how changing parameters intrinsic to the binary system or its circumstellar dust manifests in the light curve profile. To do this, we generate large grids of light curves with linearly stepped parameters and non-linearly spaced phase samples; we use a ‘periastron-dense’ sampling where samples are log spaced up to $\phi = 0.5$ (which gives many more samples at low phase), then duplicated and flipped up to $\phi = 1$, which gives sparse sampling around the $\phi \sim 0.5$ region but dense leading up to and trailing away from periastron. Computing light curve grids is a computationally expensive process, since each light curve needs dozens of phase samples, and so we generate these grids focusing on emission from only a single wavelength. Similarly, except where otherwise stated we generate gridded light curves with time invariant dust masses and grain size distributions (i.e. by setting $\beta_d = \beta_d = 0$ in equations 4.6 and 4.9 respectively).

We focus the bulk of this exploration on the WR 140 system. This stands out as the singular system with extraordinarily well-defined geometry – through decades of imaging, spectroscopic orbits, and geometric modelling – that also has a well-sampled infrared light curve, in part due to its relatively short orbital period. There exist some systems with well-defined geometry (e.g. Apep; [White et al., 2025](#)) and well-sampled light curves (e.g. WR 48a; [Williams et al., 2012](#)), but none quite as complete as WR 140. Therefore it is a suitable testbed to see how changing parameters affects the light curve.

We start by considering the effect of changing inclination. Even with spectroscopically determining orbits – long considered the gold-standard in obtaining orbital parameters – there is an inherent mass-inclination degeneracy where lower masses or lower inclinations can produce the same behaviour. Any information that the photometry of these systems could give, then, would be beneficial in breaking such a degeneracy. Figure 4.6 shows the effect of changing the binary orbital inclination on the light curve overall, namely that, at least keeping all other parameters in WR 140 constant, the effect is constrained to around periastron passage – the decline in brightness following this, and the subsequent baseline flux, is unaffected by the inclination of the system. Interestingly, the orbital phase at which the light curve sharply increases seems to be a sort of step function parameterised on inclination. We see that high inclinations, those $50^\circ \lesssim i \lesssim 90^\circ$, begin to increase in flux at $\phi \sim 0.97$ while those at lower inclinations peak just after periastron. We note, interestingly, that the half-open angle for WR 140 is approximately 40° ([Han et al., 2022](#)), and so this discontinuity could be a result of dust along the line of sight between the observer and the central binary. It

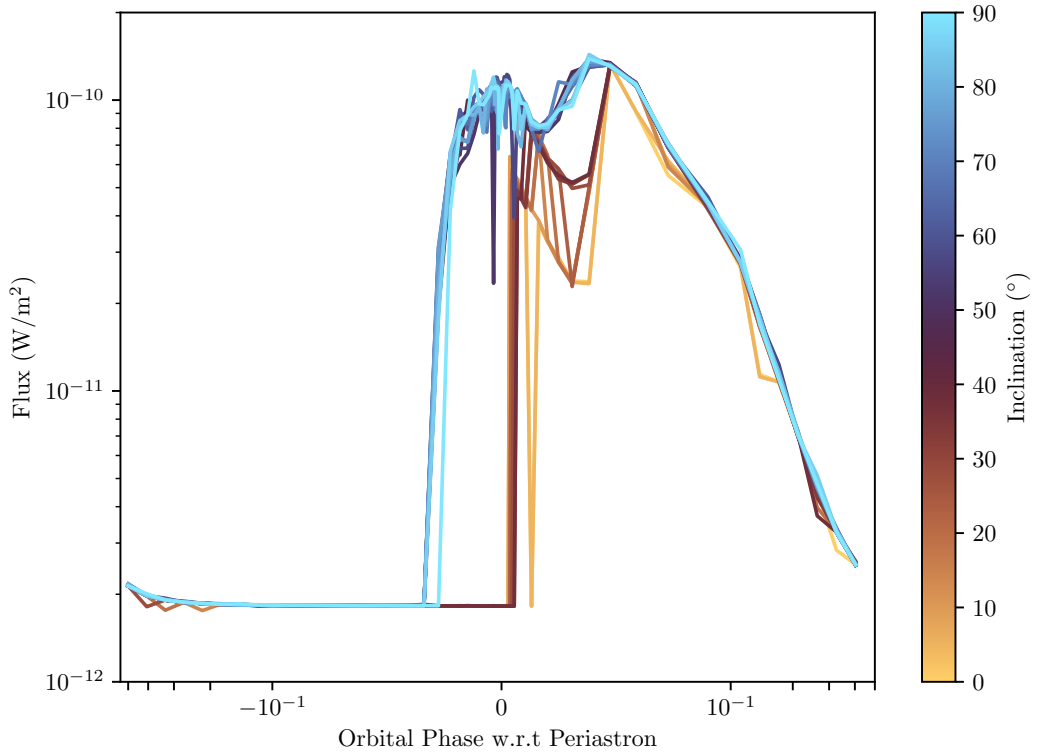


FIGURE 4.6: We ran a grid of light curve simulations for WR 140 capturing $3.5 \mu\text{m}$ emission (approximately L band), varying purely the inclination of the system. Light curves are generated between $i = 0^\circ$ (binary orbit is in the plane of the sky) and $i = 90^\circ$ (binary orbital plane is in the line of sight). Each light curve was generated with 60 phase samples using the ‘periastron-dense’ sampling technique described in the text. Note that the phase axis is on a symmetric log scale, with a linear axis $\Delta\phi = 0.1$ either side of $\phi = 0$.

is not clear why dust between us and the stars leads to an earlier onset of flux rather than the reverse (intuitively, we might expect the initially optically thick dust to be *obscuring* the stars), though perhaps this young dust does not effectively scatter light, instead absorbing it and re-emitting it in a radial direction.

In addition to a grid of inclinations, we simulated a grid sampling over dust mass and grain size distribution (for which both were time invariant) to see, for the first time, numerically how these influence a light curve. Representations of this light curve grid are shown in Figures 4.7 and 4.8. We find that the dust mass within each shell is by far the dominant parameter on the overall flux within the light curve – intuitively, more dust mass should lead to more thermal emission (once the shells are optically thin). Looking to the rate of flux decline from peak, as shown via the orbital phase at half-brightness (right side of Figure 4.8), we see that the dust mass is still marginally dominant, albeit with large grains having as much of an impact as dust mass to prolong the decline in flux.

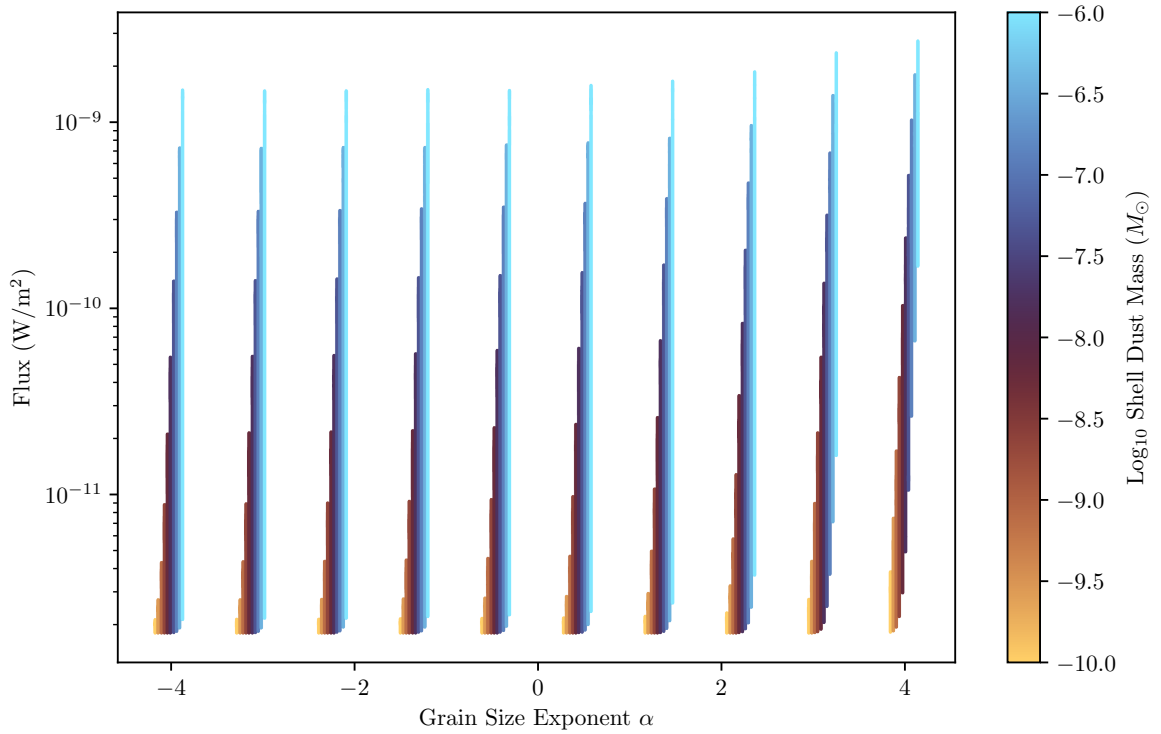


FIGURE 4.7: We show here the flux ranges for each light curve in our dust mass versus grain size distribution exponent grid. Each vertical line represents the range between the flux minima and maxima for a light curve of that maximum dust mass and grain size, where each group of light curves across the exponent axis are all evaluated at the same α but have some horizontal scatter to differentiate between the samples.

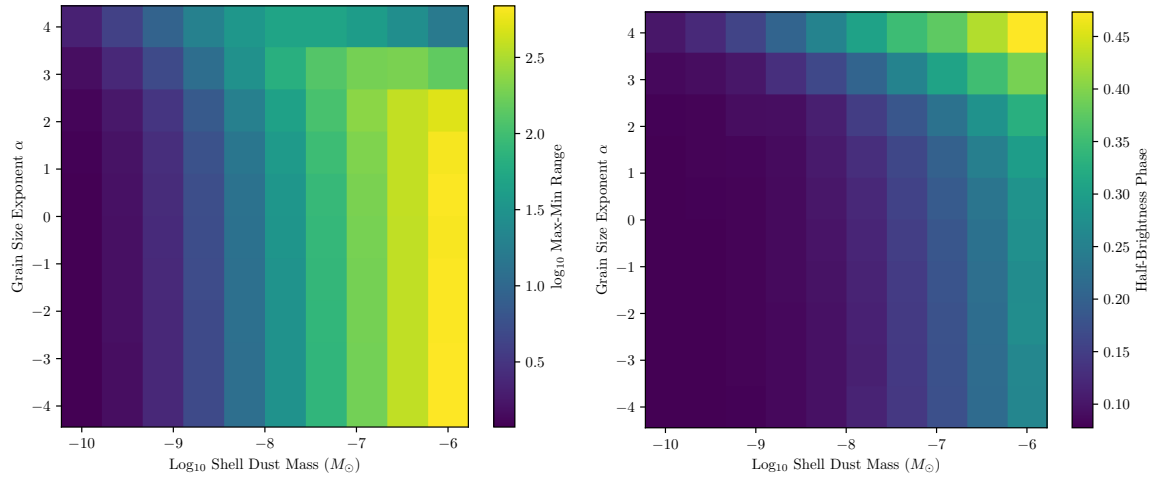


FIGURE 4.8: *Left:* The orders of magnitude difference between the flux minimum and maximum of each light curve of our grid shows that the dominant influence is the shell dust mass. *Right:* How fast the light curve declines after the peak is less dominated by one parameter, instead being dependent almost equally on dust mass and the grain size distribution. All of the light curve peaks are at approximately the same orbital phase, and so the phase when the light curve declines to its half brightness well-describes the decline rate.

So far we have investigated the effect of changing dust parameters on the light curve profile, but not yet compared to real data. We show the first such comparison in Figure 4.9, where we simulate a light curve of $3.5\text{ }\mu\text{m}$ emission and compare it to archival data from Taranova & Shenavrin (2011a,b). We see that the broad behaviour – a sharp peak in flux just after periastron passage and subsequent slow decline – is well reproduced, albeit with some ~ 1 mag residual error in the peak profile. This large second peak in flux is observed in longer wavelength emission (see the M band curve in Williams, 2011), though not in lower wavelengths. WR 140’s orbit is extremely eccentric, with dust production happening almost entirely in the phase range $0 \lesssim \phi \lesssim 0.05$; this favours a sharp peak in flux with a rapid falloff, and so in order to capture the slow decline our model required a large maximum grain size distribution exponent ($\alpha_{\max} = 4.5$ for 2 shells, with a minimum and maximum size of $0.01\text{ }\mu\text{m}$ and $0.5\text{ }\mu\text{m}$ respectively). The other dust parameters used in the simulation are described in Table 4.2, where the orbital and geometric parameters used are those in Han et al. (2022) and Lau et al. (2022).

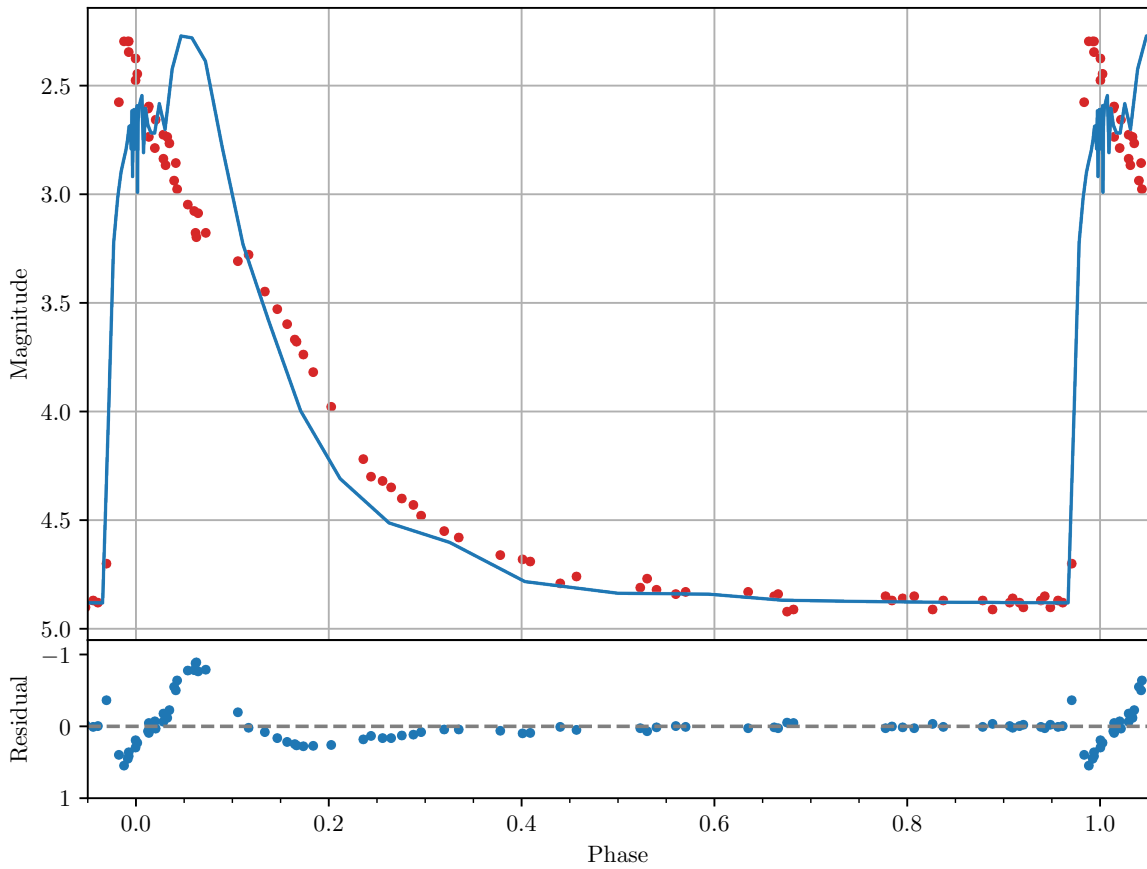


FIGURE 4.9: We compare a simulated light curve of WR 140 (blue line) to archival data at $3.5\text{ }\mu\text{m}$ (red points) from Taranova & Shenavrin (2011a,b). The used dust and system parameters are as shown in Table 4.2, and two dust shells were used in the radiative transfer run. The residuals, $F_{\text{model}} - F_{\text{data}}$ are shown in the bottom panel; the broad phenomenology is reproduced well, but there remains discrepancies particularly in the shape of the peak.

Parameter	Value	Parameter	Value
Maximum Grain Size	4.5	Maximum Dust Parcel Mass, $M_{d,\max}$	$10^{-13} M_\odot$
Dist. Exponent, α_{\max}		Maximum Shell Dust Mass [†] , $\sum M_d$	$1.37 \times 10^{-8} M_\odot$
Grain Size Distribution Bounds	[0.01, 0.5] μm		
b_g	5	b_d	3
c_g	0.05	c_d	2
d_g	0.2		

TABLE 4.2: The dust parameters for our WR 140 light curve (Figure 4.9) favour large grain sizes and a dust mass comparable to the observationally inferred value of a few times 10^{-8} (Williams, 2011). The left column are parameters pertaining to the grain size distribution, and the right column are the dust mass parameters. [†]This is a calculated parameter, given the other point cloud and dust mass parameters.

More work needs to be done to align our light curve simulations with observations, and to simulate the light curves of other CWB systems. Aside from not yet having access to decades of photometry for other systems², the problem itself is degenerate, computationally expensive, and is high dimensional. All of these drawbacks make it difficult to try to manually search parameter space for an observational light curve, but there may be solutions in the future. During the writing of this thesis, a JAX-based radiative transfer code, RADJax (Levis et al., 2025), was described in the literature. The vast majority of astrophysics-focused radiative transfer codes are designed with the CPU in mind, but ray tracing is orders of magnitude more efficient on even consumer-grade GPUs. JAX has native support for GPU computations, and so RADJax was shown to be orders of magnitude faster for some given problems. The autodifferentiability of JAX code also lends itself towards solving inference problems in high dimensions, e.g. with Hamiltonian Monte Carlo inference or gradient descent optimisation. We did not use RADJax in this work as the code is, as of the time of writing, closed source, but its use is a promising avenue for future work.

4.2.3 Cooling Curve Analysis

To learn about the properties of dust and the circumstellar environment, it can be useful to construct a temperature profile (or cooling curve) of dust around stellar systems. The slope of this cooling curve can then describe the physical properties of the dust grains in that environment. The very first step of any MCFOST run, before any images are produced, is to compute the temperature profile of the dust given the radiation sources at its centre. Hence, in looking to compute light curves of these systems we get their temperature profiles essentially for free.

There are some caveats with how MCFOST computes the temperature profile, however. The first is that the temperature structure is computed in a random way; although

²Much of this data is not available publicly online, and though some custodians of it expressed interest in this analysis, we were not able to retrieve the data in the time frame of this Thesis.

the unstructured density grid (the point cloud) is given to MCFOST in a specific ordering, this ordering is randomised for performance reasons during Voronoi tessellation. When this randomisation is turned off, `Voro++` significant drops in performance and memory issues arise and so we leave the Voronoi randomisation turned on. This means that while we have detailed information about the exact temperature of each point in the point cloud, we do not know to which exact point that temperature corresponds to. Therefore we cannot create a temperature spatial map. Still, we are able to analyse the macroscopic temperature profile using this information.

Figure 4.10 shows an example of what our temperature profile output is, here for 3 shells of the Apep system using the parameters from [White et al. \(2025\)](#) and amorphous carbon dust with a mass of each dust shell of $10^{-5} M_{\odot}$ (similar to that inferred in [Han et al., 2020](#)). In the histogram we see three distinct Gaussians in temperature space, each one corresponding to a different concentric dust shell, where the highest temperatures correspond to the innermost shell and the temperatures subsequently fall with radius. To obtain the mean temperature within each shell, we used a Gaussian Mixture model using the Scikit-Learn library ([Pedregosa et al., 2011](#)) to fit 3 components. Using this, we find temperatures of $T_1 = 307 \pm 17$ K, $T_2 = 177 \pm 6$ K, and

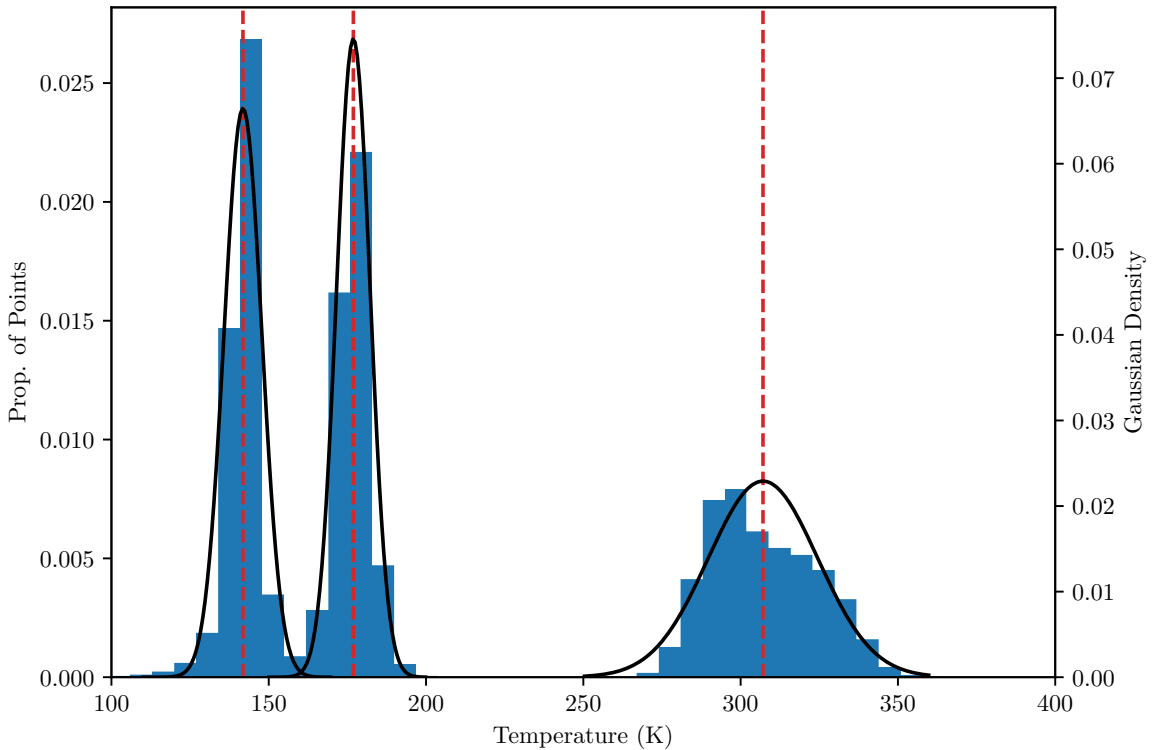


FIGURE 4.10: A histogram of the temperature of each dust parcel in the 3-shell Apep point cloud shows 3 distinct Gaussians, one for each concentric shell. The blue histogram shows the binned points of the point cloud, the black curves the three fit Gaussian curves according to the text, and the vertical red lines the mean temperature of each shell.

$T_3 = 142 \pm 6$ K for the innermost to the outermost shells respectively. Despite needing to infer the temperature of each shell, we are able to simply calculate the average the radii of each shell (where the ‘error’ in this case corresponds to the standard deviation of radii within each shell) and then form a cooling curve, which we show in Figure 4.11. Following from Han et al. (2025), we fit a power law of the form

$$T(r) = T_0 \left(\frac{r}{r_0} \right)^{-\gamma} \quad (4.13)$$

to this cooling curve. Here, T_0 is the temperature of dust at a distance r_0 from the stellar binary, and we set $r_0 = 10^4$ au. Fitting for this by bootstrapping on a least-squares fitting routine we obtain a power law exponent of $\gamma_{\text{sim}} = 0.381 \pm 0.024$ and a factor $T_{0,\text{sim}} = 340 \pm 15$ K at 10^4 au. This exponent is well aligned with what we expect from amorphous carbon grains – Williams et al. (2009) derives an expected exponent of $\gamma = 0.384$ for grains in radiative equilibrium – which is a good consistency

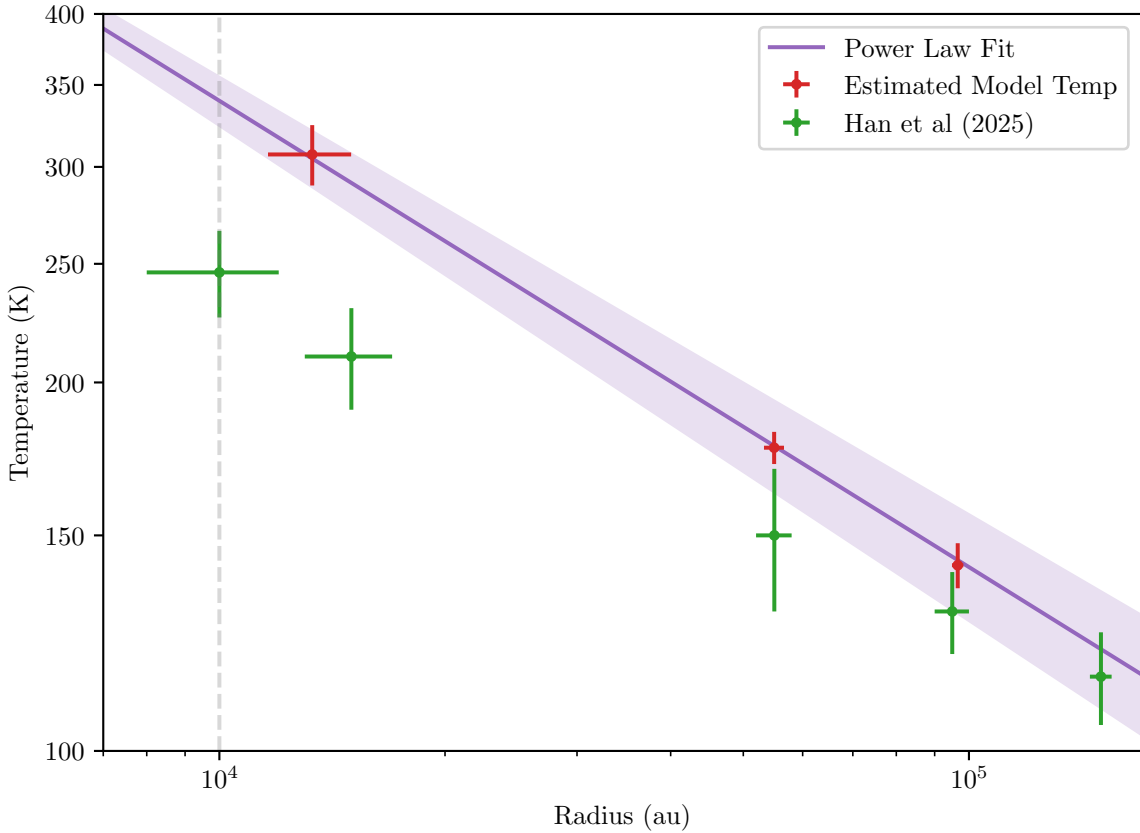


FIGURE 4.11: We compare the cooling curve from our simulated shells of Apep to that presented in Han et al. (2025). The red points are those simulated with our radiative transfer model, where the purple shaded region shows the uncertainty in our fit. The green points are the approximate values from Han et al. (2025), averaged across the features at each radius. The dashed vertical line at $r = 10^4$ au is to help give a visual aid for the meaning of the T_0 parameter.

check considering that the simulation was done assuming solely amorphous carbon in radiative and thermal equilibrium. These parameters fit on our simulation are at odds with those found observationally in Han et al. (2025): $\gamma_{\text{obs}} = 0.31 \pm 0.02$ and $T_{0,\text{obs}} = 246 \pm 7$ K. Therein, Han et al. used the flux density across 3 wavelength bands to estimate the spectral energy distribution and the subsequent temperature of features within each concentric shell. It is not immediately clear why there is such a discrepancy between the values, namely whether the observational Apep nebula truthfully deviates from what we would expect from amorphous carbon (e.g. if there are other grains or non-equilibrium processes involved) or if the observational result is erroneous. Regardless, both results deviate significantly from the $\gamma = 0.5$ cooling curve associated with purely blackbody emission indicating that irradiation from the central binary remains important to $\gtrsim 10^5$ au scales.

Hear those bells ring deep in the soul
Chiming away for a moment
Feel your breath course frankly
below
And see life as a worthy opponent

David Le'aupépe, *Achilles Come Down*
(*Gang of Youths' 'Go Father in*
Lightness')

5

Peering into the Serpent's Dust

The success of our light curve modelling of colliding wind binaries fundamentally relies on our understanding of the dust geometry of these systems. This modelling powerfully describes exactly where the dust is in the environment around the central WR binary, but itself does not provide much insight into the physical conditions leading to dust formation and its subsequent properties. For this, more detailed analyses are needed. In this Chapter we describe our preliminary work seeking to better understand the dust formation and destruction mechanisms taking place within the most enigmatic WR CWB: Apep. To study dust formation processes in Apep, and in the process better understand the winds of each of the WR stars, we run a series of hydrodynamic models focusing on the binary periastron passage which we describe in Chapter 5.1. In Chapter 5.2 we utilise a set of analytical models to describe better the grain destruction mechanisms taking place in the newly-discovered tertiary cavity in the Apep system.

5.1 Dust Formation

The Apep system presents mysteries in scores. There is a well documented discrepancy between the spectroscopic stellar wind speeds and the apparent dust expansion speed (Callingham et al., 2019), the open question of how two classical WR stars can coexist in the same system at the same time (Callingham et al., 2020), and how a tertiary star in the system carves a cavity in the dust nebula (White et al., 2025), among more open questions. In addition to these, our previous research in White et al. (2024) showed that, given the orbital parameters of the system and typical wind parameters for WN+WC stars, the wind-wind shock should be adiabatic across the entire orbit. This challenges our understanding of dust formation within colliding wind binaries, which is expected to occur when the wind collision region is strongly radiative. Despite this, dust is unequivocally present around the Apep system as evidenced through direct infrared imaging (Callingham et al., 2019; Han et al., 2020, 2025; White et al., 2025).

To try to better understand the Apep system in particular, we ran a series of hydrodynamical simulations using the Phantom smoothed particle hydrodynamics (SPH) code (Price et al., 2018). As described in Chapter 3, published hydrodynamic analyses have seldom focused on eccentric colliding wind binaries with episodic dust production, and this study is the first such simulation of the Apep system (or indeed a colliding wind binary with two very strong WR winds).

5.1.1 Simulation Setup

Our Phantom setup is based on a modified version of that in Siess et al. (2022) and Deschaux-Beaume & Siess (2025), focusing on 3D winds ejected from stars. In this setup, shells of SPH particles are ejected from the surface of a sphere – distributed across a Fibonacci sequence spiralling along the spherical surface – at regular time steps (see Chapter 3.2 of Deschaux-Beaume & Siess, 2025, for more detail). Distinct from that original paper, our simulations feature two such stellar winds where the resolution of the wind injection grid is determined by an overall wind resolution parameter and the mass loss rates of each star; we set the resolution to 100 particles per shell for the star with the higher mass loss rate in all of our simulations, where the ‘secondary’ star (in terms of mass loss) has a proportionally lower resolution since Phantom SPH particles have equal mass. As the code is periodically injecting more and more particles into the simulation, we set an outer boundary of 3000 au at which particles are deleted so as to stop the compute time increasing exponentially – this results in a roughly steady state particle population of $\sim 3.5 \times 10^6$.

The Apep central binary is known to host a nitrogen type and a carbon type Wolf-Rayet star. These WR types have typical mass ranges and well-defined wind chemistry which we consider in our simulation setup. The orbital period is observationally constrained to ~ 190 yr (Han et al., 2025), and the semi-major axis to ~ 90 au (Han et al., 2020). WN type stars are universally more massive than WC stars, and so to enforce the desired orbit with an appropriate mass ratio we chose typical stellar masses of $M_{\text{WN}} = 15.5 M_{\odot}$ and $M_{\text{WC}} = 7.1 M_{\odot}$ (Crowther, 2007).

While there seems to be a clear separation of stellar mass with WR spectral type, this is not so much the case when it comes to mass loss rates. It is therefore ambiguous which of the WN or WC stars in the Apep system has the dominant wind (with previous studies arbitrarily choosing one over the other, e.g. Marcote et al., 2021), despite both stellar wind speeds being known precisely (where the WN star has a wind speed of 3500 km s^{-1} and the WC star 2100 km s^{-1} ; Callingham et al., 2020). In this work we choose the WN star to have the stronger wind. In addition to this, we assume the WC stellar wind under the anisotropic wind hypothesis introduced by Callingham et al. (2019), where we approximate the spherical WC stellar wind as having the ‘dense equatorial’ wind speed of 1020 km s^{-1} (in line with the nebula expansion speed inferred by Han et al., 2025; White et al., 2025). It would be a suitable topic of future work to simulate a full anisotropic wind of the WC star, with a dense and slow equatorial wind simultaneous with a fast and sparse polar wind. Still, if the spin axis of the WC star is aligned with the orbital plane of the binary, we might not expect wind anisotropy to have a significant effect (White et al., 2024). From geometric modelling of the Apep nebula we have strong constraints on the wind momentum ratio of the two

WR stellar winds; using the relationship between the shock cone opening angle and wind momentum ratio from (Tuthill et al., 2008; Gayley, 2009),

$$\eta_{\text{S/W}} = \left(\frac{121}{\theta_{\text{OA}}/2} - \frac{31}{90} \right)^3 \quad (5.1)$$

where $\eta_{\text{S/W}}$ is the ratio of the stronger to the weaker wind and θ_{OA} is the shock opening angle, we obtain a required $\eta_{\text{S/W}} \approx 2.55$ given the observationally derived cone opening angle of $\theta_{\text{OA}} = 125^\circ$ (White et al., 2025). WN mass loss rates are usually in the range $10^{-4.5} \lesssim \dot{M}_{\text{WN}} \lesssim 10^{-3.8} M_\odot/\text{yr}$, with a peak at about $\dot{M}_{\text{WN}} \sim 10^{-4.3} M_\odot/\text{yr}$ which is what we give the WN star in our simulation. Hence, to give the required wind momentum ratio with a WN star with that mass loss rate, a wind speed of 3500 km s^{-1} , and a WC wind speed of 1020 km s^{-1} , the wind momentum ratio equation

$$\eta = \frac{\dot{M}_1 v_{\infty,1}}{\dot{M}_2 v_{\infty,2}} \quad (5.2)$$

requires that the mass loss rate of the WC star be $\dot{M}_{\text{WC}} \sim 10^{-4.17} M_\odot/\text{yr}$ which is high but not unreasonable for a WC star (Crowther, 2007), especially if this mass loss rate is localised around an equatorial band and the poles have a lower mass loss rate.

The chemistry of a double Wolf-Rayet stellar wind also sensitively affects our simulation parameters. WR stars are characterised by an absence of hydrogen in their spectra and therefore in their wind material too. The chemical abundance in WC stellar winds is roughly equal parts helium and carbon with some small amount of more massive ions (De Marco & Barlow, 2001), and we assume that the WN wind is made up entirely of helium. We set the stellar temperatures to be $T_{\text{WN}} = 6 \times 10^4 \text{ K}$ and $T_{\text{WC}} = 4 \times 10^4 \text{ K}$, which are typical of stars of these type (Crowther, 2007). For such temperatures, we expect that the helium in the wind will be totally ionised and that the carbon will be mostly composed of CIV ions with the remaining in CV ions (Kostenko & Kholygin, 1999; Zhekov et al., 2011). In its default state, Phantom cannot track the chemistry within each SPH particle and so all particles in the simulation assume the same molecular properties; we set the wind to be overall 20% carbon and 80% helium by number density, i.e. $f_{\text{C}} = 0.2$ and $f_{\text{He}} = 0.8$. Given that most of the carbon is expected to be CIV, we set the proportion of carbon in this ion species to $f_{\text{CIV}} = 0.75$ and therefore $f_{\text{CV}} = 0.25$. The mean molecular weight of the particles in our simulation is then

$$\mu = \sum_j \frac{f_j A_j}{1 + n_{e,j}} \quad (5.3)$$

$$= f_{\text{C}} \left(f_{\text{CIV}} \frac{A_{\text{C}}}{1 + n_{e,\text{CIV}}} + f_{\text{CV}} \frac{A_{\text{C}}}{1 + n_{e,\text{CV}}} \right) + f_{\text{He}} \left(\frac{A_{\text{HeII}}}{1 + n_{e,\text{HeII}}} \right) \quad (5.4)$$

$$\simeq 1.486 \quad (5.5)$$

where A_j and $n_{e,j}$ represent the atomic mass and number of free electrons of each ion species respectively.

The Apep system produces dust within a specific range of orbital true anomaly centred around the periastron passage. This dust production is observationally constrained to be between $\nu_{\text{turn-on}} = -108^\circ$ (or equivalently, 252°) and $\nu_{\text{turn-off}} = 141^\circ$

(where $\nu = 0^\circ$ corresponds to periastron; [White et al., 2025](#)). With this in mind, we initialise each hydrodynamic simulation with the stars at a true anomaly of 230° in their orbit – about 20° before the expected dust ‘turn on’. This is so that the simulation has time to reach a steady state before the expected turn on is reached (which we find is reached very quickly, in only a couple of degrees in true anomaly). Since dust production is centred around periastron, we evolve the simulations for ~ 100 time units (where each time unit in the simulation is $\Delta t = 5.023 \times 10^6$ s) so that the stars pass periastron during the run. Given that the outer boundary of the simulation was chosen to be 3000 au for computational reasons, we would not be able to resolve an entire shell at once and so we care mainly about the behaviour of the fluid near to the binary.

The problem of dust formation in the Apep system is indeed a problem. One of the dominant cooling mechanisms relevant for shocks and used in hydrodynamic simulations [Malfait et al. \(2024b\)](#) is HI cooling, which is expected to be a significant contributor in cooling hot shocked gas towards temperatures of $\lesssim 10^4$ K in order to start condensing dust grains. The Apep system has no hydrogen, though, bearing two classical Wolf-Rayet stars at its centre which excludes the use of hydrogen-based cooling mechanisms. Separately, [Deschaux-Beaume & Siess \(2025\)](#) implemented a high temperature cooling prescription that seeks to model line emission, bremsstrahlung, and Compton heating+cooling. We considered additionally implementing inverse-Compton cooling with the prescription introduced in [Mackey et al. \(2023\)](#) – a cooling mechanism that accounts for photon scattering in the intense radiation field and circumstellar plasma in CWBs – though the authors discussed that this effect should be significant only in radiative shocks. Even accounting for IC cooling, we found in [White et al. \(2024\)](#) that the Apep colliding wind shock should be roughly adiabatic across its entire orbit, and so an implementation of IC cooling should not have much of an effect for this system. We considered an alternative tabulated cooling prescription, e.g. like that in [Eatson et al. \(2022\)](#), but delegate this to future work.

With these dust formation caveats in mind, we instead chose to perform a parameter space exploration on the adiabatic index as a proxy for a more sophisticated cooling prescription. It is common to lower the adiabatic index towards $\gamma \sim 1$ to approximate an isothermal, or radiatively cooling, shock (for example, [Lamberts et al., 2011](#); [MacLeod & Loeb, 2020](#)). We ran identical simulations at three different adiabatic indices: $\gamma_1 = 1.01$ (asymptotically approaching isothermal), $\gamma_2 = 1.1$, and $\gamma_3 = 5/3$ (a ‘true’ adiabatic simulation), and we present the results of these in the following section.

5.1.2 Results

With our hydrodynamic simulations of the Apep system we have captured the expected colliding wind shock phenomenology. We show in Figures 5.1 and 5.2 the gas density distribution in the region around the WR+WR binary for an orbital phase just following periastron passage, as plotted with the **Sarracen** Python package ([Harris & Tricco, 2023](#)). Figure 2.1 presents an annotated version of the CWB shock phenomenology, but we describe again here the key features specifically for our Apep simulations. Given our simulation setup, the higher momentum wind is faster and sparser and constitutes the less opaque regions of Figure 5.1. We see the first shock, which is expected to be

orders of magnitude hotter and less dense than the second shock on the side of the higher momentum wind. In contrast, the second shock (significantly denser and hence brighter in Figure 5.1) traces the wind of the lower momentum wind, in this case that of our WC star. In this Figure, the orbital motion of the stars is anticlockwise, and so the orbit wraps the shock into a spiral with leading and trailing arms which correspond to boundaries at the forefront and in the wake of orbital motion respectively (and so there are both leading and trailing first and second shocks). We note that due to the relatively equal wind momentum ratio, there is no reconfinement shock within the weaker wind region, and that the contact discontinuity, in this case, is synonymous with the second shock (since there is no reverse shock in the weaker wind region).

We see immediately that the adiabatic index affects the phenomenology of the first and second shocks in different ways. We first note the change in behaviour between the leading and trailing shocks as a function of adiabatic index. Regarding the denser second shock we see that for a lower index the trailing arm has a larger density compared to the leading arm. This is in contrast to a larger index where the leading arm has a similar maximum density (brightness) to the trailing arm. Assuming for the moment that dust preferentially forms in these regions of higher density, this aligns well with observations of colliding wind nebulae; strongly radiative shocks (e.g. that in WR 140; Williams et al., 2009; Han et al., 2022; Lau et al., 2022) result in a strong dependency of dust mass as a function of azimuthal angle within the shock cone (that is, dust preferentially forms in the trailing arm) while more adiabatic shocks (e.g. the Apep nebula; White et al., 2024, 2025) have little-to-no indication of a leading versus trailing dust mass disparity. We also note key differences in the less-dense

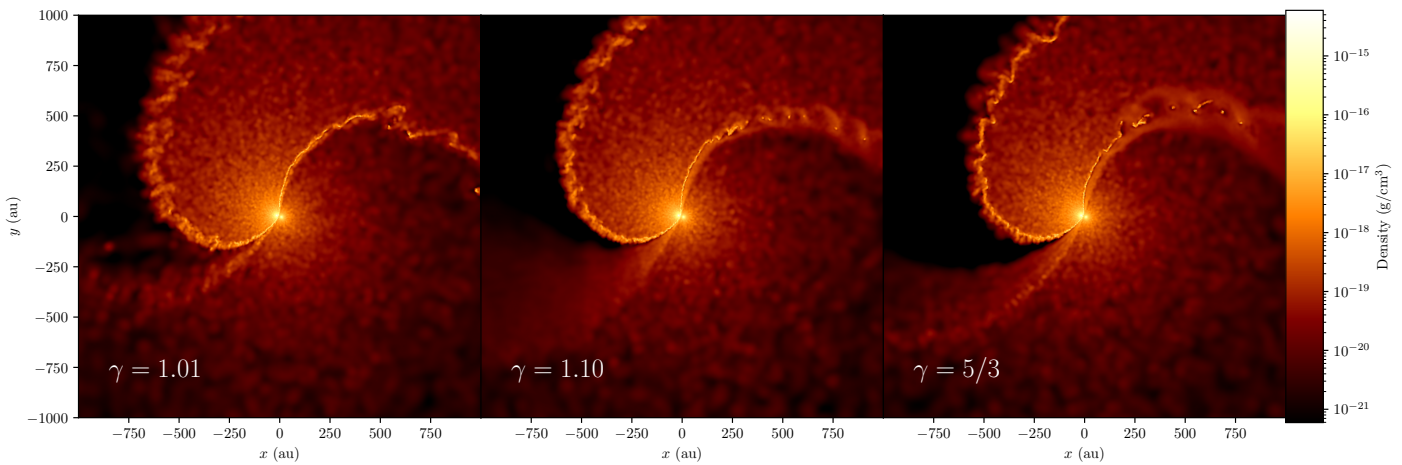


FIGURE 5.1: The density cross section along the midplane of each of our three simulations reveals subtle differences as a function of adiabatic index. The time snapshot is consistent across each panel, where the stars are a few degrees in true anomaly prior to periastron, making their way in closer ($t \sim 16$ yr since simulation start). The two stars light at the centre of each panel, indicated by a region of high gas density (as the winds are densest near to the stellar surface). See Figure 2.1 for a description of the phenomenology in these images, and Figure A.1 for a version zoomed out to the spatial bounds of the simulation.

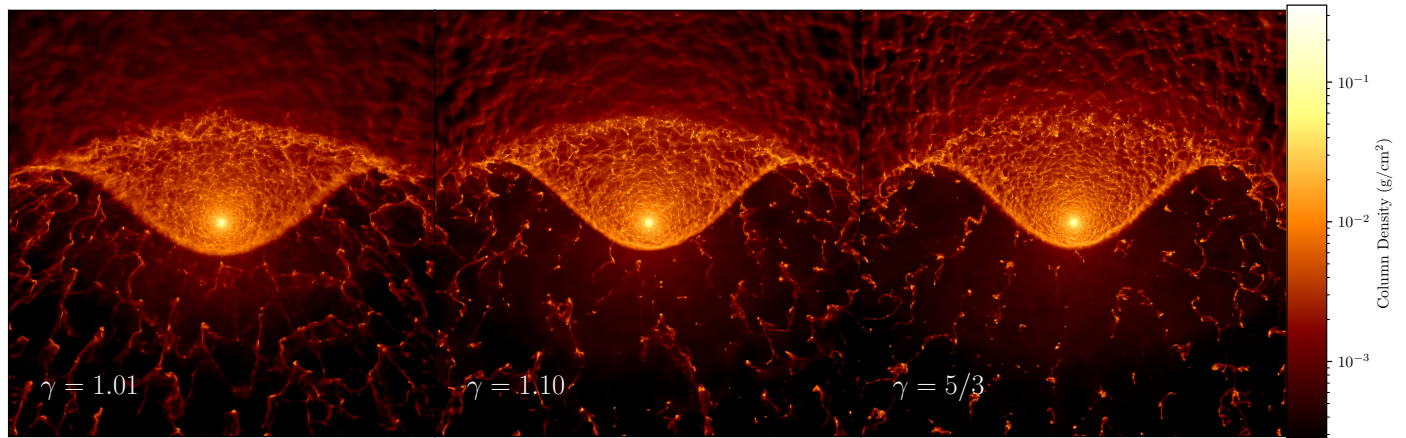


FIGURE 5.2: Plotting the projected (column) density reveals significantly more structure and different phenomenology compared to a cross section slice as in Figure 5.1. The spatial scale is the same as in the previous Figure, though the view here is not looking down onto the binary orbital plane but rather along the separation vector of the two stars.

first shock across adiabatic index. It is well established that a higher adiabatic index leads to less compression and hence mass density in the first shock (Stevens et al., 1992) – we see that the second shock tends to be more inflated for higher adiabatic indices, and more granulated in the approximately isothermal case. In addition, we see in Figure 5.1 that the trailing shock sharpens considerably for a more isothermal adiabatic index (or in other words, the first and second shocks being ‘squeezed’ into the contact discontinuity), leading to higher contrast structure in the trailing shock as the higher momentum wind interacts directly with the turbulent material (the so-called thin-shell instability). This is even more obvious in the colliding wind structure as a function of adiabatic index as we look at the cross section on a larger scale as in Figure A.1. Although the shock is reasonably uniform in structure across adiabatic index for small radii, at $r \gtrsim 500$ au the thin-shell instability for more isothermal indices begins to dominate. Still, we do see small-scale structure within the shocked material even for $\gamma = 5/3$ in Figures 5.2 and A.1; the thin-shell instability is not just a function of cooling but of mass density too (Kee et al., 2014). The fact that we observe a dusty colliding wind nebula around the Apep system – and one with a wealth of flocculent structure at that (Han et al., 2025; White et al., 2025, and Figure 2.2) – despite its shock potentially being adiabatic across its entire orbit (White et al., 2024) could be a result of this being the only nebula confirmed to be sourced from two classical Wolf-Rayet stars both with high mass loss rates.

Aside from the density of gas, the temperature of the shocked material is particularly important for dust formation. We show in Figure 5.3 the temperature distribution of the material at the same spatial scale as in Figure 5.1. As expected, we see that the first shock is consistently orders of magnitude hotter than the second shock at a typical minimum of $T \sim 10^7$ K and is hence not conducive to dust formation (which takes place at $\lesssim 2000$ K). We note that because of our neglect of sophisticated,

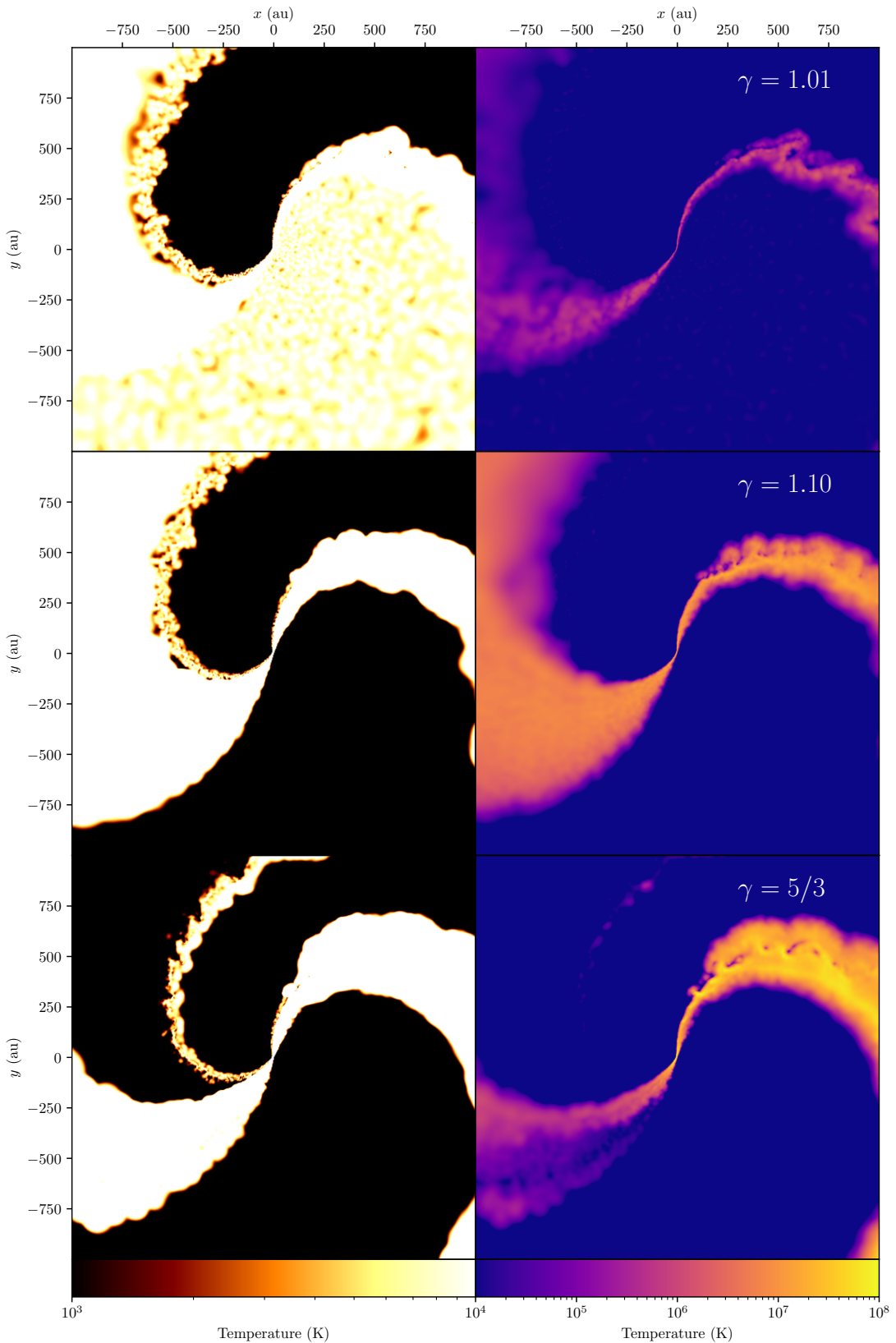


FIGURE 5.3: We compare the temperatures of the shocked winds across adiabatic indices (rows). The left column colour scale focuses on the cooler 2nd shock, while the right column colour scale focuses on the hotter 1st shock. The hydrodynamic snapshots are the same as those in Figure 5.1. We see, broadly, higher temperatures for higher adiabatic indices especially in the first shock (right column).

chemistry-dependent cooling functions, our shocked material seldom reaches this low a temperature anywhere in the simulation domain bar for a few localised pockets. We see many regions at $T \lesssim 10^4$ K, however, which we qualitatively describe as regions of possible dust formation (which is typical in the literature given how difficult it is to simulate dust nucleation in such complex systems, e.g. Soulain et al., 2023). Across all studied adiabatic indices, we see regions of low temperature particularly in the leading second shock (and especially so for the $\gamma = 5/3$ case). A low-temperature trailing shock is only significant in the $\gamma = 1.01$ case, although there are regions of cool material for the other simulated indices.

The morphology of the first shock is particularly apparent when observing in the high-temperature space. For $\gamma = 1.01$ we see that the trailing first shock is indeed suppressed in spatial extent and temperature as suggested by the mass density distribution. In contrast, the trailing first shock for $\gamma = 5/3$ is well-extended and ~ 2 orders of magnitude hotter than in the approximately isothermal case, further suggesting a suppression of dust formation.

The final state variable of the gas we consider is pressure. When we plot the pressure of the SPH particles in the simulation as a function of radius and temperature (Figure 5.4) we see that there are three distinct regions of parameter space. The low pressure and low temperature region corresponds to each unshocked stellar wind¹. The intermediate pressure and temperature region corresponds to the dense second shock, while the high pressure and temperature region corresponds to the sparse first shock. Visualising the SPH particles in this way allows us to easily partition particles as needed for further analysis. For example, dust formation takes place solely within the cool dense second shock so, even though our simulated gas does not reach a low enough temperature for dust formation on account of our lack of cooling prescription, we are able to estimate the presence of dust making a few simple assumptions. To separate out this proposed dust nucleation environment, we take particles that fit the following criteria:

$$r > 30 \text{ au}; \quad 10^3 \text{ K} \leq T \leq 1.5 \times 10^4 \text{ K}; \quad \log_{10}(P) \geq -2.6266 \log_{10}(r) - 3.12019 \quad (5.6)$$

The condition on pressure in the above criteria was found by fitting a line between $(\log_{10}(P_1), r_1) = (-7, 30)$ and $(\log_{10}(P_2), r_2) = (-11, 10^3)$, with P in units of erg/cm³ and r in au, in order to best separate out the turquoise region of Figure 5.4. With the dense second shock separated out, we are able to make some estimates of the dust mass by taking the gas mass and then assuming a gas-to-dust mass ratio of 100:1 (Aller, 1984). Due to the simulated domain border of 3000 au we are not able to estimate the mass of an entire shell at once, but in considering the simulation duration we are able to estimate a dust production rate² of $\dot{M}_d \approx 5.3 \times 10^{-7} M_\odot/\text{yr}$ (irrespective of adiabatic index) which agrees almost perfectly with the estimated rate in Han et al. (2020) and is well within the bounds of their uncertainty.

¹This is not true in the $\gamma = 1.01$ simulation (Figure A.4), since our Phantom setup detects the WN wind as conducive to dust formation here. We ignore this since in truth the WN wind alone does not have the chemistry for dust formation in this astrophysical environment outside of rare eruptions

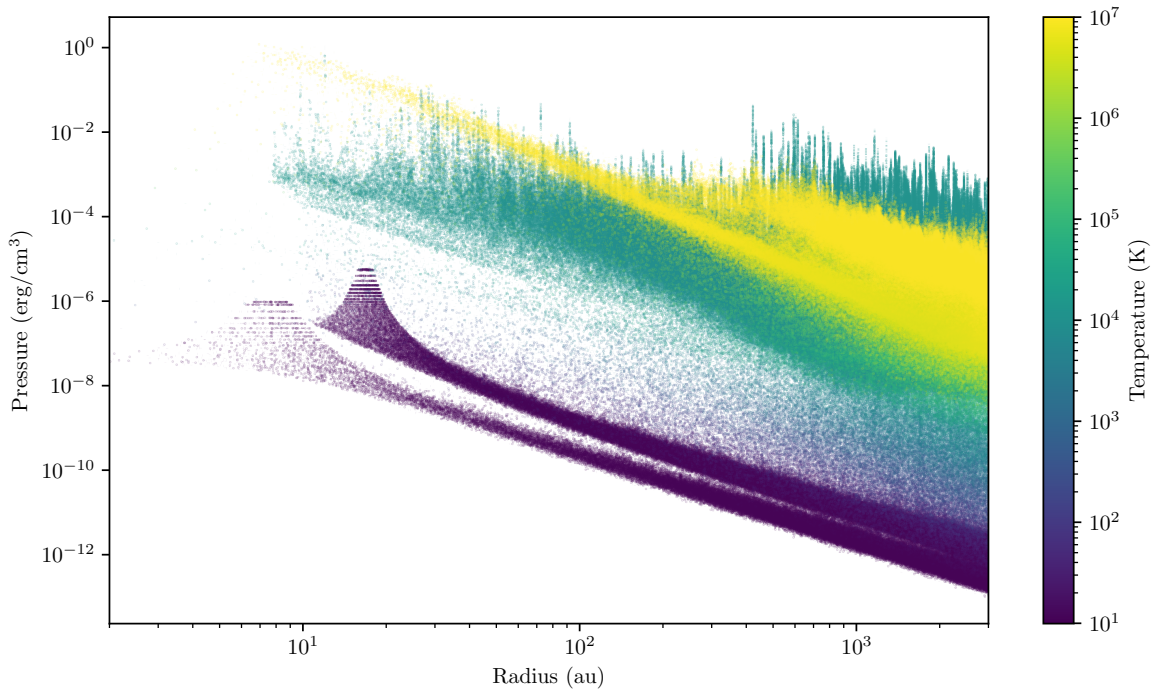


FIGURE 5.4: The phenomenology of the wind-wind shock can be mapped to distinct regions in pressure-radius-temperature space. Here we plot all of the SPH particles from our $\gamma = 1.1$ simulation in this space, where each point has an opacity of 0.2. Particles were plotted in order of temperature (so that high temperature points overlay low temp ones). Analogous plots for the other simulated adiabatic indices are shown in Figures A.4 and A.5.

With the second shock separated as a proxy for the dust distribution, we are also able to compare it to our geometric model which describes purely the dust distribution. We show a direct comparison in Figure 5.5, with what is a perfect qualitative match for the Apep nebula at a phase of $\phi = 0.02$. Of course, the geometric model smooths over any thin-shell instability that is produced in the hydrodynamic simulation, but this forms a valuable consistency check and a validation of our assumption that these regions are sites for dust nucleation. The geometric model has been a consistently powerful tool to explain observations (e.g. Lau et al., 2022; White et al., 2025), and our comparison here presents the first time that it has been verified to match hydrodynamic simulations, supporting our use of the geometric model as a proxy for more detailed simulations.

One of the few, albeit less-supported hypotheses for the wind speed/nebula expansion speed discrepancy in the Apep system is that some process at the shock front significantly slows down the expansion of material. If this were the case, in our hydrodynamic simulations we would expect to see the expansion of the second shock (which is cooler and denser, and would go on to be the site of dust formation) proceeding at a

e.g. Barniske et al. (2008) and Rubio et al. (2020)

²We calculate this by considering the ‘crossing time’ of the gas, given the simulation bounds and the radial velocity of the second shock.

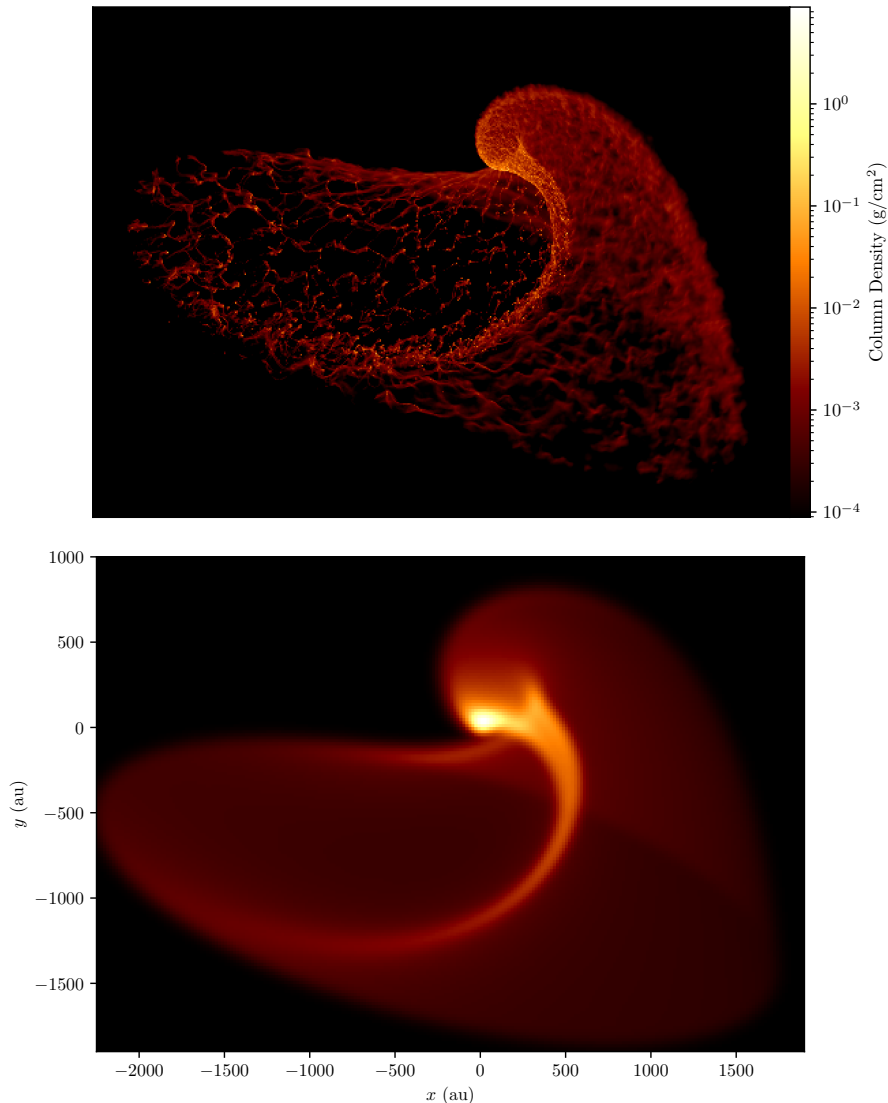


FIGURE 5.5: We compare our hydrodynamic simulation of Apep (top) – having rotated it to its correct orientation in the plane of the sky (White et al., 2025) and made the particle cuts as described in the text – to our geometric model (bottom) at $\phi = 0.02$. The hydrodynamic simulation here is for $\gamma = 1.1$, but the general structure is identical for the other adiabatic indices tested in the text, albeit with varying degrees of small-scale structure. Note the geometric model is also displaying column density, except on a normalised scale (and not in physical units).

rate slower than either of the unshocked stellar winds. We show the radial velocities of the simulated gas in Figure A.3. We see that the second shock expands at the velocity of the WC stellar wind in our simulation, 1020 km/s, which we simulate here as the subdominant wind albeit with a higher mass loss rate than the WN star. It would be a worthwhile future study to investigate the impact of changing the dominant wind to that of the WC star to see if the second shock expansion speed traces that of the subdominant wind (with which the shocked material is coeval) or the stellar wind with the higher mass loss rate. Given the observationally derived wind momentum ratio,

the WC star *must* have the higher mass loss rate in both cases, but in the former case the second shock would expand with the WN wind speed and in the latter the second shock would still expand with the WC wind speed.

5.2 Dust Destruction

This Section is an adapted excerpt from our peer-reviewed publication, White et al. (2025), accepted in the Astrophysical Journal.

One of the key open questions since the discovery of Apep is whether or not the ‘northern companion’ star, an O8 Iaf supergiant 0.7” north of the central WR+WR binary, is associated with the WR stars and Apep nebula, or is a (statistically unlikely) apparent line-of-sight alignment. In analysing archival VLT data, together with the new VLT epochs and JWST imagery, we have conclusively linked the O star to the WR stars, identifying the Apep system as a hierarchical triple. The new evidence for this lies in an apparent ‘cavity’ of dust along the direction of the tertiary star from the WR+WR binary. Figure 5.6 shows that by incorporating a ‘dust destruction’ region along the surface of a cone into our geometric model, we may accurately explain the missing dust. The parameters of the destruction cone, in spherical coordinates relative to the orbital plane of the WR+WR binary, are shown in Table 5.1. We also note that adding a stellar sprite 1700 au from the inner binary at the 3D angular position of the cavity precisely matches the observed location of the tertiary star in Apep, further supporting the O star as the cavity sculptor. Due to the asymmetric nature of the Apep nebula, the angular position of the O star is uniquely associated with the position of the cavity and so there are no alternative configurations that can explain such cavity ridge positions.

Our proposed mechanism for this cavity is as follows. As the dust forms from the central WR+WR colliding wind shock, that material expanding radially northwards enters the environment of the O star companion. A large fraction of this northbound dust is destroyed and no longer contributes to the infrared emission, carving a gap in

Parameter	Value
Inclination Angle, β_{tert}	$(124 \pm 10)^\circ$
Azimuthal Angle, α_{tert}	$(239 \pm 10)^\circ$
Opening Angle, $\theta_{\text{OA,tert}}$	$(90 \pm 10)^\circ$
Tertiary Star Radial Position, r_{tert}	$1700 \pm 200 \text{ au}$

TABLE 5.1: Parameters describing the simple conical model for the dust depletion region of Apep due to the northern companion in an ordinate system relative to the WR+WR binary orbital plane. An inclination angle of 0° lies directly below the orbital plane, while the periastron position of the inner binary is at 180° azimuthal angle. For the r_{tert} parameter, we assume the distance to Apep is $d = 2.4 \text{ kpc}$. This table is taken from White et al. (2024, 2025), where there is also a more in-depth description of each parameter and the cavity model.

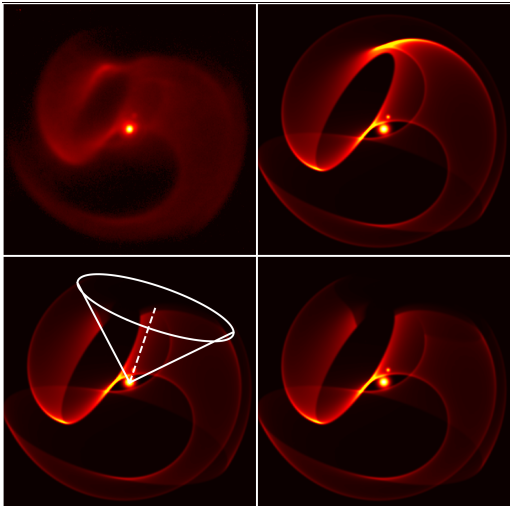


FIGURE 5.6: The tertiary cavity in the Apep nebula is well reproduced by geometric models (see Section 3.2). *Top left:* The minimally processed VLT/VISIR data of the Apep nebula. *Top right:* Models that do not account for the tertiary overpredict nebula flux in the northern region. *Bottom left:* The tertiary can be accounted for by extending a cone from the inner binary along the direction of the tertiary and destroying dust in this volume. *Bottom right:* Accounting for this in the model means that the data is more faithfully simulated. Figure from White et al. (2025).

the shell geometry. The dust then continues outward where the cavity persists as a scar indicative of earlier interaction with the tertiary star.

The root cause of the apparent cavity of dust in the Apep nebula is almost certainly a combination of several processes in parallel. From our derived geometry of the cavity, we are able to discern some relative dominance between competing effects. The main pieces of information we have pertaining to the dust physics is that the cavity open angle is approximately $90 \pm 10^\circ$, and that the O supergiant companion lies 1700 ± 200 au from the WR+WR central engine – with these two pieces of information together, we find that the radius of the cavity when the dust shell directly passes the O companion is also about 1700 au.

The first avenue to dust destruction we consider is grain sublimation as a result of radiative heating from the O star. For a UV source of brightness L_{UV} and grain sublimation temperature of T_{sub} , Hoang et al. (2019) gives the sublimation distance as

$$r_{\text{sub}} \simeq 0.015 \left(\frac{L_{\text{UV}}}{10^9 L_\odot} \right)^{1/2} \left(\frac{T_{\text{sub}}}{1800 \text{ K}} \right)^{-2.8} \text{ pc} \quad (5.7)$$

For carbonaceous dust with sublimation temperature $\sim 1800 \text{ K}$ (Lau et al., 2023), and a source of UV luminosity $\sim 10^5 L_\odot$, we arrive at a sublimation radius of ~ 30 au. This is two orders of magnitude smaller than the required dust destruction radius of $\lesssim 1700$ au, and so grain sublimation cannot be the dominant process of dust destruction in the Apep nebula.

The second process of destruction we consider is by grain-grain or grain-ion collisions inducing grain shattering. O supergiant stars, like Wolf-Rayets, are characterised by fast and dense winds, so we would expect a significant wind-wind shock where the nebula intercepts the supergiant wind. To test whether we observe such a shock as expected, we consider the required wind momentum ratio (equation 5.1). Inserting an opening angle of 90° yields a momentum ratio of $\eta_{\text{S/W}} \sim 13$ for the mixed WR+WR wind to the O8 Iaf wind. If a wind-wind shock is the dominant influence on this cavity, we would expect to recover a similar wind momentum ratio with equation 5.2. For this, we can use our nebular expansion speed of 1020 km s^{-1} and estimate a mass flux of $\sim 10^{-4} - 10^{-4.75} M_\odot \text{ yr}^{-1}$; the exact mass flux is difficult to discern since it is the mixed

product of two WR winds, each with different intrinsic mass loss rates, but each should be independently in this range (Callingham et al., 2020). Callingham et al. (2020) gives the terminal wind speed of the O star as $1280 \pm 50 \text{ km s}^{-1}$, and if we assume a mass loss rate in the range $10^{-5.2} - 10^{-6} M_{\odot} \text{ yr}^{-1}$ (typical for O supergiants of this spectral type; Crowther & Evans, 2009), we can recover a wind momentum ratio of $\eta_{\text{S/W}} \sim 13$ using equation 5.2. This result implies that the cavity geometry may be explained at least partially by the presence of a tertiary shock with grain-ion sputtering. Although the radius of the cavity is 1700 au, the tertiary shock front will be significantly closer to the O star at the point of stagnation between the mixed WR+WR wind and the O star wind. Following Marcote et al. (2021); Cantó et al. (1996), the stagnation point will be at a distance

$$R_{\text{W/S}} = \frac{r_{\text{tert}}}{1 + \eta_{\text{S/W}}^{1/2}} \quad (5.8)$$

from the O star (with the weaker wind). Inputting our distance and wind momentum ratio values gives a distance of ~ 370 au, which is still an order of magnitude too large for the dust destruction mechanism to be from dust sublimation. In Section 5.2.1 we describe more mechanisms that may be working in parallel on the dust grains within the cavity geometry.

5.2.1 Effect on Dust Grains in the Cavity

Our tertiary cone modelling does not exactly produce the observed structure and one of the last remaining mysteries in the Apep plume geometry is the origin of the horizontal ridge outlining the cavity on its southern border. Our first interpretation of this ridge is that the O star may deflect some proportion of the dust onto this outer ridge, but modelling this has proven difficult. We considered and implemented several models of deflection in an attempt to explain this ridge, where the O star deflects dust particles: into a ring along the entire cavity edge; onto the cavity edge on those angular coordinates co-located with the dust; or onto a central angular position along the cavity boundary with some azimuthal spread, but all three models were unsuccessful in reproducing the geometry. The first two ideas significantly over-predict ridges at other locations that are not seen in the observations, and the third can produce a ridge in the correct location (by design) but at an angle which does not match the observed ridge. Given that this is a persistent feature across the shells, we do not think that this is an anomalous dust feature (created by e.g. a surface mass eruption). Consequently, our picture of the tertiary shock is that it does not displace dust grains but rather destroys them. Estimates on the dust grain properties within and around the cavity are difficult to discern without spectra, however, but constraints can be inferred based on the environmental conditions.

The disruption of dust grains via radiative torques (radiative torque disruption – RATD) has recently been studied in the context of Wolf-Rayet colliding wind binaries (Lau et al., 2023; Hoang et al., 2019). This occurs due to high energy photon absorption inducing rotation in asymmetric dust grains, thereby inducing a centrifugal stress which can disrupt the grains (Hoang et al., 2019). At a given distance $r_* \text{ pc}$ from a central point source of luminosity L_* (units of $10^9 L_{\odot}$) with mean wavelength $\bar{\lambda}_{0.5}$ (in units of $0.5 \mu\text{m}$), the maximum size of dust grains with tensile strength S_9 (units of 10^9 erg cm^{-3})

surviving this mechanism is given by Hoang et al. (2019) as

$$a_{\text{RATD}} \simeq 0.003197 \left(\bar{\lambda}_{0.5}^{-1.7} L_*^{-1/3} r_*^{2/3} S_9^{1/2} \right)^{1/2.7} \mu\text{m} \quad (5.9)$$

Using this, together with our cavity edge distance of 1700 au, a mean wavelength given by a blackbody distribution of 30 kK, a luminosity of $10^{5.9} L_\odot$ (typical of O8 Iaf supergiants), and a grain maximum tensile strength of 10^9 erg cm^{-3} (for disordered grains, Hoang & Tram, 2019), we obtain a maximum surviving dust grain size of $\sim 4 \text{ nm}$. The timescale on which this destruction takes place is

$$\tau_{\text{RATD}} \simeq \frac{368}{438} \bar{\lambda}_{0.5}^{-1.7} L_*^{-1} r_*^2 S_9^{1/2} (10 a_{\text{RATD}})^{-0.7} \text{ yr} \quad (5.10)$$

which, with the same parameters and calculated maximum grain size, is $\sim 6 \text{ yr}$ (Hoang et al., 2019). More ordered, stronger grains such as graphite can have tensile strengths of $\sim 2 \times 10^{10} \text{ erg cm}^{-3}$ (Hoang & Tram, 2019), however, which results in a maximum grain size of $\sim 13 \text{ nm}$ and destruction timescale of $\gtrsim 12 \text{ yr}$. We note that the maximum grain sizes and destruction timescales due to the RATD mechanism could be underestimated by factors of a few given our orders of magnitude uncertainty in the tensile strengths across the true grain distribution. We also note that these calculations are done given parameters at the periphery of the dust cavity; in reality, we might expect a gradient of dust conditions across the cavity ‘surface’. These calculations assume that the environmental conditions are constant across the destruction timescale, when this is not the case: the dust shell, produced from the colliding wind of the WR+WR binary, is moving radially outwards first into the O stars wind and radiation and then out of it. In parallel the dust is becoming less dense as it expands into a larger shell surface with time, implying that the dust grains will be less shielded from radiation as time goes on (which explains in part why the tertiary star apparently destroys so much dust compared to the similar radiation environment of the central WR+WR binary).

Our overall picture of the dust destruction resulting in a circular cavity consists of several processes in parallel. We suggest that the tertiary wind-wind shock breaks down large grains into nano-grains via grain-grain and gas-grain collisions, while the radiation pressure from the O supergiant disrupts large grains above $\sim 4 \text{ nm}$ into nano-grains via the RATD mechanism. The closest $\lesssim 1700 \text{ au}$ to the O tertiary will see an ionising environment up to orders of magnitude more intense than the photon-dominated regions around sites of massive stellar formation (mainly due to the much smaller length scales involved in the cavity, albeit on shorter timescales), and so nano-grains will be photodissociated by the UV flux as they are formed (Schirmer et al., 2022). The many competing phenomena warrant the use of detailed simulations, for example with a hydrodynamical code, to model this observed geometry in Apep in future studies.

And it shakes and rattles through the ward
A lightning bolt across the door
Fluorescent like the visions in my sleep
So much braver than our present life
A golden factory of light
And you'll live long enough to catch its beams

David Le'aupepe, *The Overpass*
(*Gang of Youths' 'The Positions'*)

6

Conclusions and Future Work

In this thesis we have sought to model the carbon dust that we can and cannot directly see as made in Wolf-Rayet colliding wind binaries – short-lived massive systems whose dance would have enriched the early interstellar medium with carbon grains. This investigation was two fold: firstly we produced the very first ray-traced infrared light curve models of these systems so that we may better understand the multitude of systems that can never be imaged, and finally we simulated the Apel system with the hydrodynamic code Phantom so that we may compare our understanding of the system to direct observations.

Our light curve modelling of colliding wind binaries was done by interfacing our geometric code `xenomorph` with the radiative transfer code `MCFOST`. By generating dozens of ray-traced images of the nebulae across an orbit, we were able to produce the first simulated light curves of this class of system. We have shown in particular that the dust mass within each shell has a dominant impact on the overall infrared brightness of the system. Interestingly, we found that the inclination of the system has little impact on the overall light curve outside of a narrow window of phase near periastron, indicating that one would need a densely sampled light curve to have any constraining power on inclination. At present, more work needs to be done to calibrate the dust properties fed into the light curve pipeline in order to match to observations. Ideally this would be done for systems with both a densely phase-sampled light curve and well-defined geometry; WR 140 stands out as the only system that currently matches this description, although WR 48a and WR 137 have decades of photometric observations as well as recent direct images with JWST which will soon allow a strong geometric model of the systems. Once our pipeline has been calibrated on well-constrained systems, we could, in principle, seek to understand those CWBs who have quality light curves but may never be directly imaged (as they are resolution-limited by being so distant) so that we may understand carbon dust production in these systems with a greater population. Such a study would be aided by integrating `xenomorph` with a more performant radiative transfer code; the ray-tracing problem is well-suited to GPU

calculations (whereas MCFOST runs purely on the CPU), and so using e.g. RADJax (which has native GPU support) would allow for orders of magnitude faster light curve generation time. Using RADJax in particular, or else another JAX-based radiative transfer code, also has the advantage of coming with native autodifferentiation which would allow parameter inference with gradient-based techniques such as Hamiltonian Monte Carlo.

In addition to us being able to simulate a light curve, coupling our geometric model with a radiative transfer code allowed us to compute the temperature structure of the circumstellar dust distribution. With this, we calculated the temperature structure for the innermost 3 shells of the Apep system so that we could compare a simulated estimate with the recently published observational results in Han et al. (2025). Since we assumed that the dust shells are composed of purely amorphous carbon grains, we obtained a cooling curve exponent consistent with amorphous carbon which is notably discrepant from the observational fit. The error bars on both the simulated and observational fits are large, however, and the fits may be reconciled by obtaining higher quality data (e.g. with spectra as opposed to fits using direct images) and also with fitting more than one grain population. As a caveat to our model so far, the Voronoi tesselation in the radiative transfer step randomised the order of the particles and so we were not able to produce a spatial temperature map of the nebula; altering the code in the future so that it can return the sorting indices will allow us to discern the impact of self-shielding within the depth of each shell.

We also expanded our `xenomorph` code to be able to generate colliding wind nebulae in discretised velocity bins. At the time of writing, the Apep system has been observed with ALMA and we expect that the line profiles of this (currently private) data will allow us to map the 3D velocity structure of the nebula. Using our expanded geometric code together with this data will allow us to solve the anisotropic wind hypothesis and provide the strongest constraints on the distance to the system (together with the angular expansion rates measured over 8 years in Han et al., 2025) simultaneously.

In addition to the work done with our geometric model and radiative transfer code, we also performed the first hydrodynamic simulation of the Apep system. Using standard mass loss values coupled with the observationally constrained wind speeds and wind momentum ratio, we were able to reproduce the expected colliding wind phenomenology and in doing so verified the use of our geometric models. Because of the current lack of a sophisticated cooling mechanism for the hydrogen-free shocked gas in the Apep system, we did not incorporate a full dust nucleation mechanism in our Phantom simulation. It would be a worthwhile topic of future work to integrate such a nucleation mechanism for these eccentric colliding wind binaries to model the conditions of dust turn on/off for the first time, given that there are such strong observational constraints for this process. In addition to the grain nucleation process, more work would ideally be done on hydrogen-free cooling mechanisms for the wind-wind shock, and for example implementing the IC cooling mechanism (Mackey et al., 2023) into Phantom, which may not be particularly relevant for the Apep system though should be important for more compact systems.

Despite our neglect of a rigorous dust nucleation process in our hydrodynamic model, by making a few simple assumptions we are still able to infer some properties of dust formation. We made cuts on the temperature and pressure of the SPH particles

to separate out the dense secondary shock where dust is expected to nucleate; in doing so, we found a dust production rate of $\dot{M}_d \approx 5.3 \times 10^{-7} M_\odot/\text{yr}$ assuming a gas-to-dust mass ratio of 100:1, almost exactly in-line with the observationally inferred rate of $\dot{M}_d = 5 \times 10^{-7} M_\odot/\text{yr}$ in [Han et al. \(2020\)](#). One notable feature of our hydrodynamic models is that turbulence in the shock results in regions of high density. Qualitatively similar flocculent material was observed with new JWST imagery of the Apep system ([Han et al., 2025](#); [White et al., 2025](#)), and comparing the spatial properties of the turbulent regions in our simulations to that in the observations may help constrain the cooling processes taking place in Apep’s shock.

We chose to represent Apep’s WN star as the higher momentum wind in our hydrodynamic simulations, meaning that the dense secondary shock was comoving with the weaker WC wind. We made this decision arbitrarily; the WC star could just as well have a higher momentum wind (and the WC star must have a higher mass loss rate in either case given the observationally constrained wind speeds), and future work could seek to understand the effect of changing the order of wind momenta on the overall nebula expansion. Here, the dust nebula would expand at the slower speed of the WC wind, but it remains unclear as to whether the dense shock traces the wind speed of the star with a higher mass loss rate or if it traces the wind speed of the weaker wind with which it is comoving with.

Finally, we investigated the effect of a recently associated tertiary companion on the Apep dust nebula ([White et al., 2024, 2025](#)). In doing so we are able to put broad constraints on the surviving dust grains within a cavity carved from the tertiary shock. Still, the exact mechanism by which this cavity is carved remains unclear. Building on our existing simulations to incorporate a tertiary O supergiant star in the hydrodynamic setup could help reveal if this cavity is possible purely from an additional wind-wind shock (e.g. a similar setup to [Malافت et al., 2024a](#)). In particular, it would be interesting to model this interaction with a magnetohydrodynamics (MHD) code; [Marcote et al. \(2021\)](#) imposes a non-detection of non-thermal radio flux up to $40 \mu\text{Jy}$ for a tertiary interaction in the Apep system, and an MHD simulation may provide some estimate of the intrinsic flux of such an interaction.

A

Appendices

A.1 Additional Hydrodynamic Simulation Plots

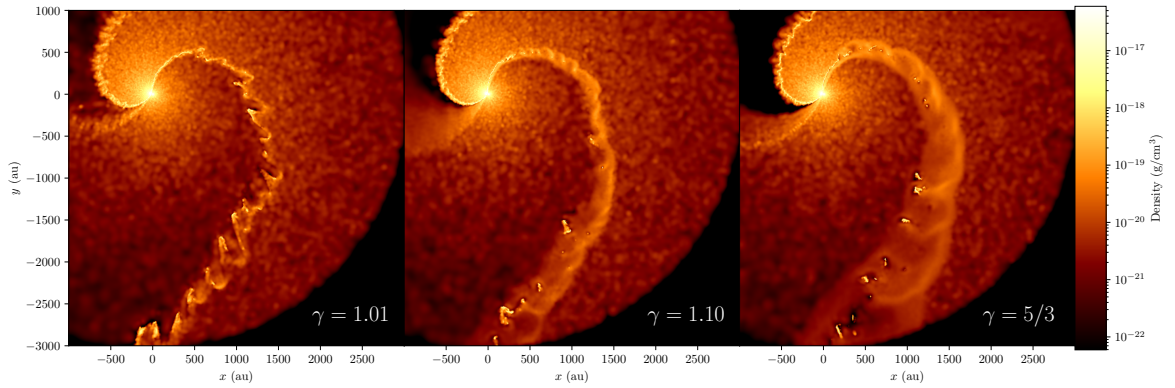


FIGURE A.1: We show a zoomed out version of the same data as in Figure 5.1. A zoomed out view highlights the onset of thin shell instability for the lower adiabatic indices, and especially the ‘puffy’ shock of larger indices. We note the region at $r = 3000$ au at which point particles are no longer simulated for computational reasons.

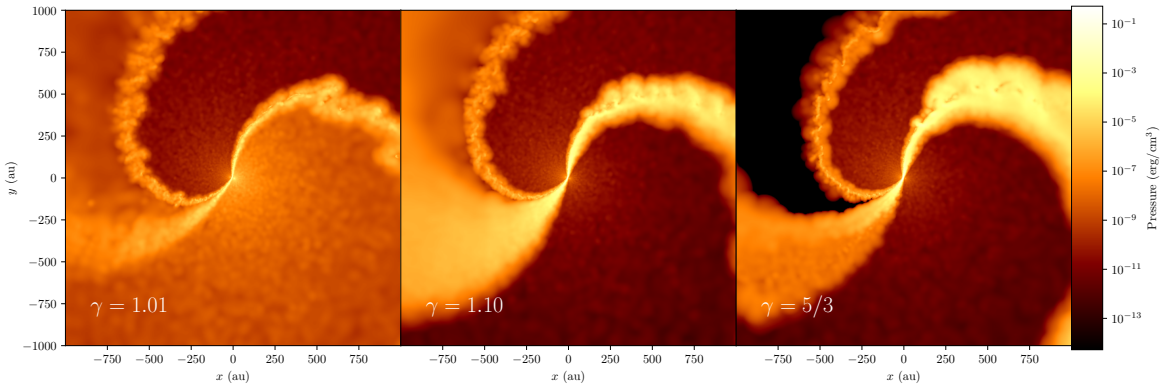


FIGURE A.2: The gas pressure at each region of the shock is sensitive to the adiabatic index used. We see broadly higher pressures and inflated shocks (first and second) for a higher adiabatic index, and low pressures for the unshocked stellar wind.

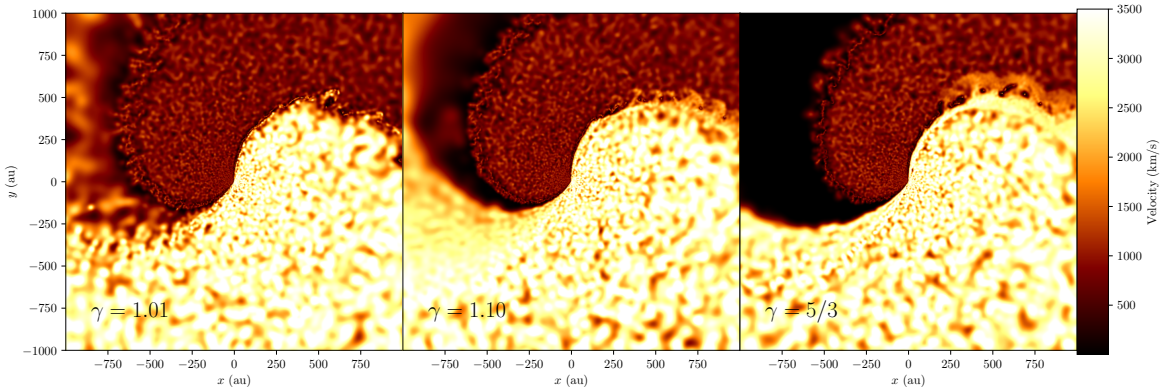


FIGURE A.3: Looking at the velocity, $v = \sqrt{v_x^2 + v_y^2}$, of the particles in our hydrodynamic simulations shows clearly the distinction between each stellar wind. We see here that the expansion velocity of the second shock (the densest material that would go on to form the dust nebula) is of the slower WC stellar wind.

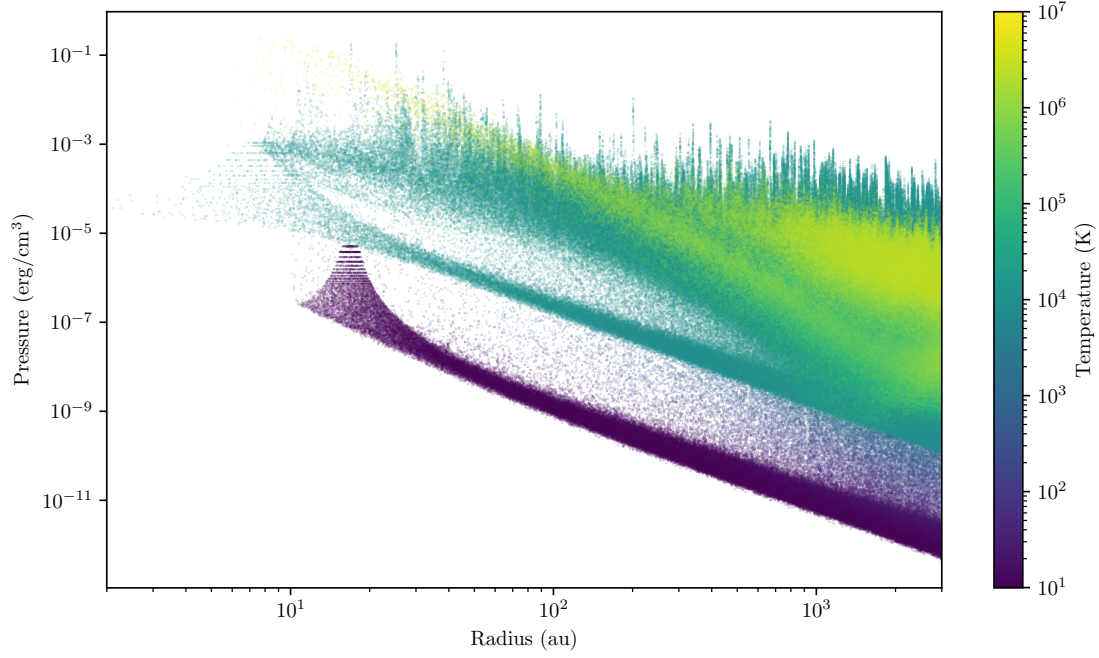


FIGURE A.4: A companion plot for Figure 5.4, here for our simulation with $\gamma = 1.01$. The colour scale and all other parameters are identical.

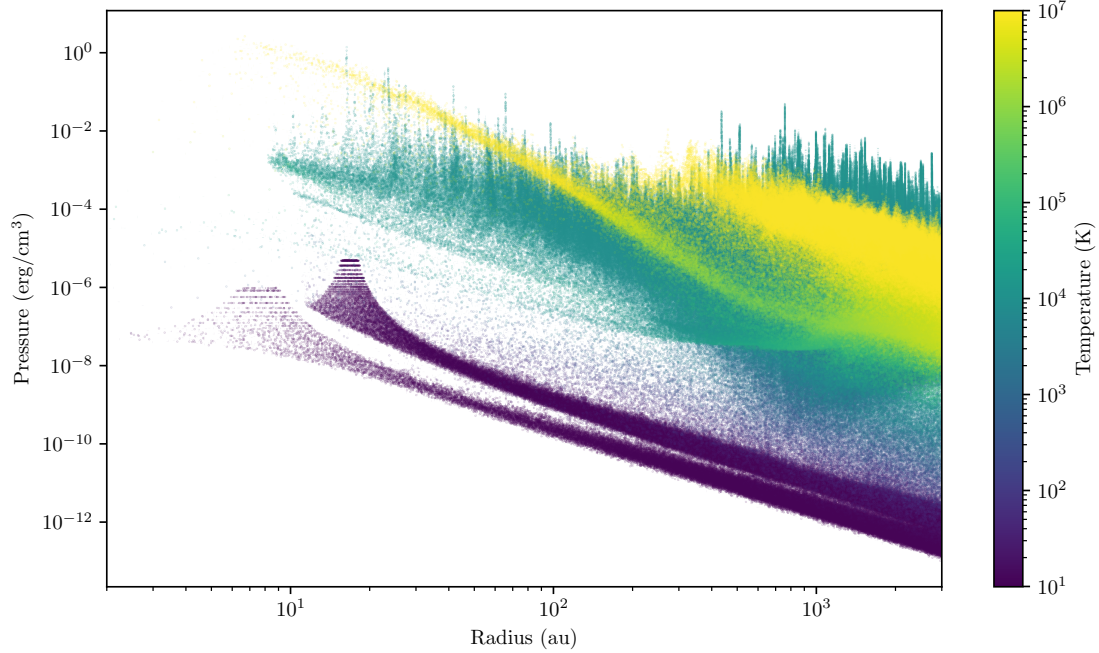


FIGURE A.5: A companion plot for Figure 5.4, here for our simulation with $\gamma = 5/3$. The colour scale and all other parameters are identical.

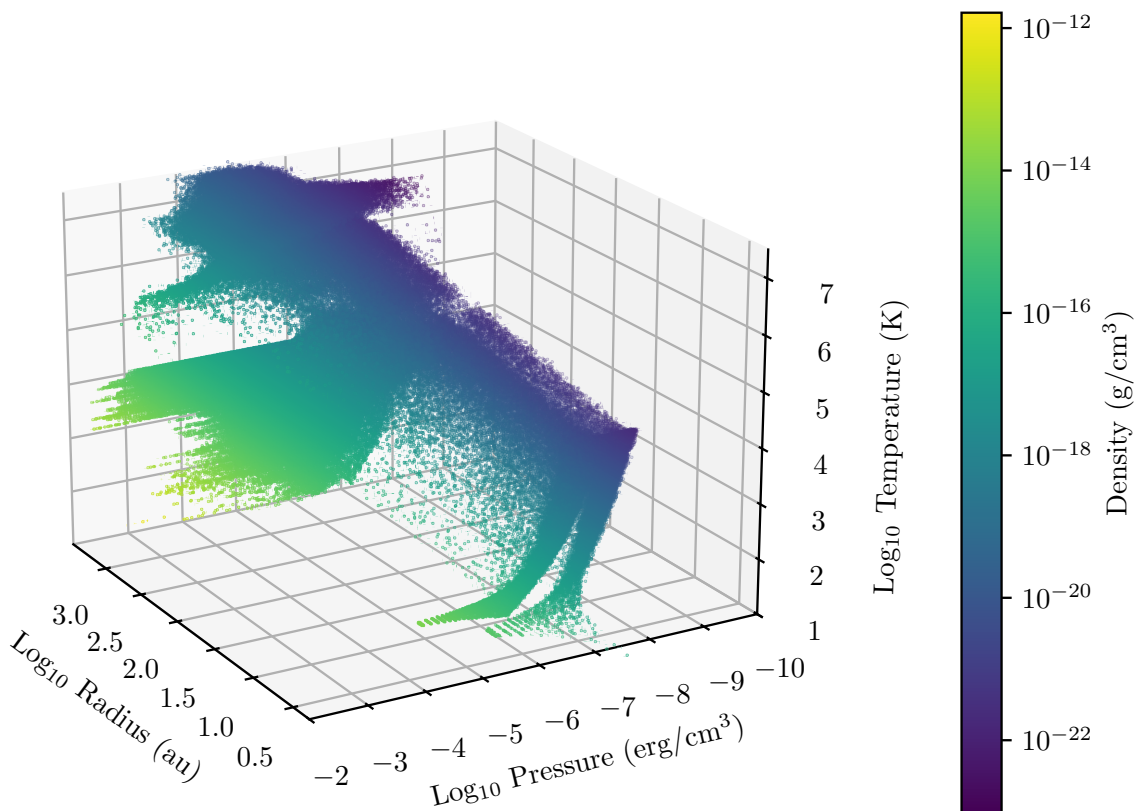


FIGURE A.6: A companion plot for Figure 5.4, where instead temperature is plotted as a third axis and the colour corresponds to the gas density.

References

- Abdi D. S., Almgren A., Giraldo F. X., Jankov I., 2024, arXiv e-prints, p. arXiv:2404.16648 13
- Aller L. H., 1984, Dust and Related Phenomena in Gaseous Nebulae. Springer Netherlands, Dordrecht, doi:10.1007/978-94-010-9639-3 48
- Astropy Collaboration et al., 2013, *A&A*, 558, A33 31
- Astropy Collaboration et al., 2018, *AJ*, 156, 123 31
- Astropy Collaboration et al., 2022, *ApJ*, 935, 167 31
- Barniske A., Osokinova L. M., Hamann W.-R., 2008, *A&A*, 486, 971 49
- Berger M. J., Colella P., 1989, *Journal of Computational Physics*, 82, 64 13
- Bloot S., Callingham J. R., Marcote B., 2022, *MNRAS*, 509, 475 9
- Boisse P., 1990, *A&A*, 228, 483 18
- Boissier S., Prantzos N., 2009, *A&A*, 503, 137 4
- Böker T., et al., 2022, *A&A*, 661, A82 22
- Boyer M. L., et al., 2012, *ApJ*, 748, 40 4
- Bradbury J., et al., 2018, JAX: composable transformations of Python+NumPy programs, <http://github.com/jax-ml/jax> 21
- Brown R. L., Wild W., Cunningham C., 2004, *Advances in Space Research*, 34, 555 22
- Burbidge E. M., Burbidge G. R., Fowler W. A., Hoyle F., 1957, *Reviews of Modern Physics*, 29, 547 3
- Callingham J. R., Tuthill P. G., Pope B. J. S., Williams P. M., Crowther P. A., Edwards M., Norris B., Kedziora-Chudczer L., 2019, *Nature Astronomy*, 3, 82 9, 41, 42
- Callingham J. R., Crowther P. A., Williams P. M., Tuthill P. G., Han Y., Pope B. J. S., Marcote B., 2020, *MNRAS*, 495, 3323 9, 17, 41, 42, 53
- Camps P., Baes M., Saftly W., 2013, *A&A*, 560, A35 19
- Cantó J., Raga A. C., Wilkin F. P., 1996, *ApJ*, 469, 729 53

- Castor J. I., Abbott D. C., Klein R. I., 1975, *ApJ*, 195, 157 6
- Cecil M., Gehrig L., Steiner D., 2024, *A&A*, 687, A136 12
- Chandrasekhar S., 1950, Radiative transfer.. Oxford, Clarendon Press 18
- Cherepashchuk A. M., 1976, Soviet Astronomy Letters, 2, 138 7
- Chruslinska M., Nelemans G., 2019, *MNRAS*, 488, 5300 4
- Claret A., Torres G., Wolf M., 2010, *A&A*, 515, A4 5
- Clementel N., Madura T. I., Kruip C. J. H., Icke V., Gull T. R., 2014, *MNRAS*, 443, 2475 20
- Crowther P. A., 2007, *ARA&A*, 45, 177 6, 42, 43
- Crowther P. A., Evans C. J., 2009, *A&A*, 503, 985 53
- Cullen F., et al., 2025, *MNRAS*, 540, 2176 4
- Dahlen T., Strolger L.-G., Riess A. G., Mattila S., Kankare E., Mobasher B., 2012, *ApJ*, 757, 70 4
- David-Uraz A., et al., 2012, *MNRAS*, 426, 1720 10
- Davidson K., Humphreys R. M., 1997, *ARA&A*, 35, 1 5
- Davis P. J., Siess L., Deschamps R., 2013, *A&A*, 556, A4 5
- De Beck E., Andrews H., Quintana-Lacaci G., Vlemmings W. H. T., 2025, *A&A*, 698, A179 22
- De Marco O., Barlow M. J., 2001, *Ap&SS*, 275, 53 43
- De Marco O., Izzard R. G., 2017, *PASA*, 34, e001 6
- De Marco O., et al., 2022, *Nature Astronomy*, 6, 1421 14
- Delaunay B., 1934, Bulletin de l'Académie des Sciences de l'URSS. Classe des sciences mathématiques et na, 1934, 793 19
- Deschaux-Beaume S., Siess L., 2025, A SPH Approach To Stellar Wind Collisions With Phantom, unpublished Masters Thesis 42, 44
- Deshmukh K., et al., 2024, *A&A*, 692, A109 6
- Detmers R. G., Langer N., Podsiadlowski P., Izzard R. G., 2008, *A&A*, 484, 831 4
- Dsilva K., Shenar T., Sana H., Marchant P., 2020, *A&A*, 641, A26 6
- Duchêne G., Kraus A., 2013, *ARA&A*, 51, 269 5

- Dullemond C. P., Juhasz A., Pohl A., Sereshti F., Shetty R., Peters T., Commercon B., Flock M., 2012, RADMC-3D: A multi-purpose radiative transfer tool, *Astrophysics Source Code Library*, record ascl:1202.015 (ascl:1202.015) 28
- Dwarkadas V. V., Dauphas N., Meyer B., Boyajian P., Bojazi M., 2017, *ApJ*, 851, 147 3
- Eatson J. W., Pittard J. M., Van Loo S., 2022, *MNRAS*, 516, 6132 15, 16, 44
- Ekström S., Georgy C., 2025, arXiv e-prints, p. arXiv:2507.15960 6
- Eldridge J. J., Stanway E. R., 2022, *ARA&A*, 60, 455 6
- Ettorre G., et al., 2025, *MNRAS*, 539, 2537 4
- Flores-Rivera L., Flock M., Nakatani R., 2020, *A&A*, 644, A50 12
- Forbes J. C., Alves J., Lin D. N. C., 2021, *Nature Astronomy*, 5, 1009 3
- Freiburghaus C., Rosswog S., Thielemann F. K., 1999, *ApJ*, 525, L121 3
- Garofali K., Levesque E. M., Massey P., Williams B. F., 2019, *ApJ*, 880, 8 10
- Gayley K. G., 2009, *ApJ*, 703, 89 43
- Gingold R. A., Monaghan J. J., 1977, *MNRAS*, 181, 375 13
- Gräfener G., Hamann W. R., 2008, *A&A*, 482, 945 4
- Grayling M., et al., 2023, *MNRAS*, 520, 684 3
- Han Y., et al., 2020, *MNRAS*, 498, 5604 38, 41, 42, 48, 57
- Han Y., Tuthill P. G., Lau R. M., Soulain A., 2022, *Nature*, 610, 269 15, 17, 33, 36, 45
- Han Y., White R. M. T., Callingham J. R., Lau R. M., Pope B. J. S., Richardson N. D., Tuthill P. G., 2025, arXiv e-prints, p. arXiv:2507.14498 8, 9, 17, 22, 27, 29, 39, 40, 41, 42, 46, 56, 57
- Harries T. J., Monnier J. D., Symington N. H., Kurosawa R., 2004, *MNRAS*, 350, 565 17, 19, 20
- Harris A., Tricco T., 2023, *The Journal of Open Source Software*, 8, 5263 44
- Heger A., Fryer C. L., Woosley S. E., Langer N., Hartmann D. H., 2003, *ApJ*, 591, 288 4
- Hendrix T., Keppens R., van Marle A. J., Camps P., Baes M., Meliani Z., 2016, *MNRAS*, 460, 3975 14, 15, 16, 20
- Hoang T., Tram L. N., 2019, *ApJ*, 877, 36 54
- Hoang T., Tram L. N., Lee H., Ahn S.-H., 2019, *Nature Astronomy*, 3, 766 52, 53, 54

- Hulse R. A., Taylor J. H., 1975, *ApJ*, 195, L51 5
- Hummer D. G., Rybicki G. B., 1971, *MNRAS*, 152, 1 18
- Johnstone C. P., Güdel M., Lüftinger T., Toth G., Brott I., 2015, *A&A*, 577, A27 12
- Kasen D., Metzger B., Barnes J., Quataert E., Ramirez-Ruiz E., 2017, *Nature*, 551, 80 3
- Kato S., Fukue J., 2020, Fundamentals of Astrophysical Fluid Dynamics; Hydrodynamics, Magnetohydrodynamics, and Radiation Hydrodynamics. Springer Nature Singapore, Singapore, doi:10.1007/978-981-15-4174-2 19
- Kee N. D., Owocki S., ud-Doula A., 2014, *MNRAS*, 438, 3557 46
- Kirchschlager F., Wolf S., 2014, *A&A*, 568, A103 29
- Klessen R. S., Heitsch F., Mac Low M.-M., 2000, *ApJ*, 535, 887 12
- Kosirev N. A., 1934, *MNRAS*, 94, 430 18
- Kostenko F. V., Kholtygin A. F., 1999, *Astrophysics*, 42, 280 43
- Kroupa P., 2001, *MNRAS*, 322, 231 4, 6
- Kudritzki R.-P., Puls J., 2000, *ARA&A*, 38, 613 7
- Kuruwita R., Tychoniec L., Federrath C., 2024, arXiv e-prints, p. arXiv:2409.03371 12
- Lamberts A., Fromang S., Dubus G., 2011, *MNRAS*, 418, 2618 14, 15, 44
- Lamberts A., Dubus G., Lesur G., Fromang S., 2012, *A&A*, 546, A60 15, 16
- Lan G.-X., Wei J.-J., Zeng H.-D., Li Y., Wu X.-F., 2021, *MNRAS*, 508, 52 4
- Lau R. M., et al., 2020, *ApJ*, 900, 190 17
- Lau R. M., et al., 2022, *Nature Astronomy*, 6, 1308 8, 17, 36, 45, 49
- Lau R. M., et al., 2023, *ApJ*, 951, 89 29, 52, 53
- Lau R. M., et al., 2024, *ApJ*, 963, 127 8, 17
- Lemaster M. N., Stone J. M., Gardiner T. A., 2007, *ApJ*, 662, 582 15
- Levis A., Luong N., Teague R., Bouman K. L., Barraza-Alfarro M., Flaherty K., 2025, Revealing Fine Structure in Protoplanetary Disks with Physics Constrained Neural Fields (arXiv:2509.03623), <https://arxiv.org/abs/2509.03623> 37
- Li J., Liu C., Zhang Z.-Y., Tian H., Fu X., Li J., Yan Z.-Q., 2023a, *Nature*, 613, 460 4
- Li J., Dempsey A. M., Li H., Lai D., Li S., 2023b, *ApJ*, 944, L42 12

- Lian J., Bergemann M., Pillepich A., Zasowski G., Lane R. R., 2023, *Nature Astronomy*, **7**, 951–954
- Lieb E. P., et al., 2025, *ApJ*, **979**, L3–8
- Lucy L. B., 1977, *AJ*, **82**, 1013–1013
- Lucy L. B., 1999, *A&A*, **344**, 282–282
- Lupton R., Blanton M. R., Fekete G., Hogg D. W., O’Mullane W., Szalay A., Wherry N., 2004, *PASP*, **116**, 133–131
- MacLeod M., Loeb A., 2020, *ApJ*, **902**, 85–14, 44
- Mackey J., Jones T. A. K., Brose R., Grassitelli L., Reville B., Mathew A., 2023, *MNRAS*, **526**, 3099–3099, 44–56
- Madau P., Dickinson M., 2014, *ARA&A*, **52**, 415–415
- Madura T. I., et al., 2013, *MNRAS*, **436**, 3820–3820
- Maeder A., Meynet G., 2000, *ARA&A*, **38**, 143–143
- Malfait J., et al., 2024a, *A&A*, **691**, A57–16, 57
- Malfait J., Siess L., Esseldeurs M., De Ceuster F., Wallström S. H. J., de Koter A., Decin L., 2024b, *A&A*, **691**, A84–44
- Marchant P., Bodensteiner J., 2024, *ARA&A*, **62**, 21–5, 6
- Marchenko S. V., Moffat A. F. J., Grosdidier Y., 1999, *ApJ*, **522**, 433–433
- Marcote B., Callingham J. R., De Becker M., Edwards P. G., Han Y., Schulz R., Stevens J., Tuthill P. G., 2021, *MNRAS*, **501**, 2478–2478, 9–42, 53–57
- Mathew S. S., Federrath C., Seta A., 2023, *MNRAS*, **518**, 5190–5190
- Mestel L., 1953, *MNRAS*, **113**, 716–716
- Metropolis N., Ulam S., 1949, *Journal of the American Statistical Association*, **44**, 335–335
- Mignon-Risse R., González M., Commerçon B., Rosdahl J., 2020, *A&A*, **635**, A42–A42
- Millour F., et al., 2009, *A&A*, **506**, L49–L49
- Monaghan J. J., 1992, *ARA&A*, **30**, 543–543
- Monnier J. D., Tuthill P. G., Danchi W. C., 1999, *ApJ*, **525**, L97–L97
- Monnier J. D., Tuthill P. G., Danchi W. C., 2002, *ApJ*, **567**, L137–L137
- Moore G. E., 1965, *IEEE Solid-State Circuits Society Newsletter*, **38**, 114–114

- Muijres L., Vink J. S., de Koter A., Hirschi R., Langer N., Yoon S. C., 2012, *A&A*, 546, A42 4
- Naoz S., 2016, *ARA&A*, 54, 441 5
- Noebauer U. M., Sim S. A., 2019, *Living Reviews in Computational Astrophysics*, 5, 1 19
- Offner S. S. R., Moe M., Kratter K. M., Sadavoy S. I., Jensen E. L. N., Tobin J. J., 2023, in Inutsuka S., Aikawa Y., Muto T., Tomida K., Tamura M., eds, Astronomical Society of the Pacific Conference Series Vol. 534, Protostars and Planets VII. p. 275 ([arXiv:2203.10066](https://arxiv.org/abs/2203.10066)), doi:10.48550/arXiv.2203.10066 5
- Oláh K., et al., 2025, *A&A*, 698, A150 5
- Paardekooper J. P., Kruip C. J. H., Icke V., 2010, *A&A*, 515, A79 19
- Parkin E. R., Gosset E., 2011, *A&A*, 530, A119 16
- Parkin E. R., Pittard J. M., 2008, *MNRAS*, 388, 1047 17
- Parkin E. R., Pittard J. M., Corcoran M. F., Hamaguchi K., Stevens I. R., 2009, *MNRAS*, 394, 1758 16
- Pedregosa F., et al., 2011, *Journal of Machine Learning Research*, 12, 2825 38
- Peraiah A., 1973, *Ap&SS*, 21, 223 18
- Pessi T., Anderson J. P., Lyman J. D., Prieto J. L., Galbany L., Kochanek C. S., Sánchez S. F., Kuncarayakti H., 2023, *ApJ*, 955, L29 4
- Pinte C., Ménard F., Duchêne G., Bastien P., 2006, *A&A*, 459, 797 21, 28
- Pinte C., Harries T. J., Min M., Watson A. M., Dullemond C. P., Woitke P., Ménard F., Durán-Rojas M. C., 2009, *A&A*, 498, 967 21, 28
- Pittard J. M., 1998, *MNRAS*, 300, 479 14
- Potapov A., McCoustra M. R. S., Tazaki R., Bergin E. A., Bromley S. T., Garrod R. T., Rimola A., 2025, arXiv e-prints, p. [arXiv:2509.10292](https://arxiv.org/abs/2509.10292) 29
- Poudel S., et al., 2025, *ApJ*, 984, 161 3
- Price D. J., 2012, *Journal of Computational Physics*, 231, 759 13
- Price D. J., Federrath C., 2010, *MNRAS*, 406, 1659 14
- Price D. J., et al., 2018, *PASA*, 35, e031 12, 42
- Prilutskii O. F., Usov V. V., 1976, *Soviet Ast.*, 20, 2 7
- Rauw G., Nazé Y., 2016, *Advances in Space Research*, 58, 761 7

- Rauw G., et al., 2005, *A&A*, 432, 985 9
- Reitberger K., Kissmann R., Reimer A., Reimer O., Dubus G., 2014, *ApJ*, 782, 96 16
- Richardson N. D., et al., 2025, *ApJ*, 987, 160 8
- Rivera-Thorsen T. E., et al., 2024, *A&A*, 690, A269 4
- Rouleau F., Martin P. G., 1991, *ApJ*, 377, 526 20, 29
- Rowan C., Whitehead H., Fabj G., Kirkeberg P., Pessah M. E., Kocsis B., 2025, *arXiv e-prints*, p. arXiv:2505.23739 12
- Rubio G., Toalá J. A., Jiménez-Hernández P., Ramos-Larios G., Guerrero M. A., Gómez-González V. M. A., Santamaría E., Quino-Mendoza J. A., 2020, *MNRAS*, 499, 415 49
- Russell C. M. P., 2013, PhD thesis, University of Delaware 16
- Rycroft C. H., 2009, *Chaos*, 19, 041111 29
- Saio H., Georgy C., Meynet G., 2013, *MNRAS*, 433, 1246 6
- Salpeter E. E., 1955, *ApJ*, 121, 161 4
- Sana H., et al., 2012, *Science*, 337, 444 5
- Sana H., et al., 2013, *A&A*, 550, A107 5
- Schirmer T., Ysard N., Habart E., Jones A. P., Abergel A., Verstraete L., 2022, *A&A*, 666, A49 54
- Schneider R., Maiolino R., 2024, *A&A Rev.*, 32, 2 4
- Schuster A., 1905, *ApJ*, 21, 1 18
- Schwarzschild K., 1906, Nachrichten von der Königlichen Gesellschaft der Wissenschaften zu Göttingen. Math.-phys. Klasse, 195, 41 18
- Sharda P., Krumholz M. R., 2022, *MNRAS*, 509, 1959 4
- Shenar T., 2024, *arXiv e-prints*, p. arXiv:2410.04436 6
- Shenar T., Gilkis A., Vink J. S., Sana H., Sander A. A. C., 2020, *A&A*, 634, A79 6
- Siess L., Homan W., Toupin S., Price D. J., 2022, *A&A*, 667, A75 12, 16, 42
- Sobacchi E., Granot J., Bromberg O., Sormani M. C., 2017, *MNRAS*, 472, 616 4
- Soulain A., et al., 2018, *A&A*, 618, A108 17, 20
- Soulain A., Lamberts A., Millour F., Tuthill P., Lau R. M., 2023, *MNRAS*, 518, 3211 15, 16, 20, 48

- Speedie J., et al., 2024, *Nature*, 633, 58 22
- Springel V., 2010, *ARA&A*, 48, 391 11, 13
- Stegmann J., Antonini F., Moe M., 2022, *MNRAS*, 516, 1406 5
- Stevens I. R., Blondin J. M., Pollock A. M. T., 1992, *ApJ*, 386, 265 14, 46
- Taranova O. G., Shenavrin V. I., 2011a, VizieR Online Data Catalog: JHKLM light curves of WR 140 (Taranova+, 2011), VizieR On-line Data Catalog: J/PAZh/37/34. Originally published in: 2011PAZh...37...34T; 2011AstL...37...30T 36
- Taranova O. G., Shenavrin V. I., 2011b, *Astronomy Letters*, 37, 30 36
- Teyssier R., 2002, *A&A*, 385, 337 13
- Toonen S., Hamers A., Portegies Zwart S., 2016, *Computational Astrophysics and Cosmology*, 3, 6 5
- Toonen S., Portegies Zwart S., Hamers A. S., Bandopadhyay D., 2020, *A&A*, 640, A16 5
- Tuthill P. G., Monnier J. D., Danchi W. C., 1999, *Nature*, 398, 487 8, 16
- Tuthill P. G., Monnier J. D., Lawrence N., Danchi W. C., Owocki S. P., Gayley K. G., 2008, *ApJ*, 675, 698 43
- Ud-Doula A., Owocki S. P., Townsend R. H. D., 2009, *MNRAS*, 392, 1022 4
- van Marle A. J., Keppens R., Meliani Z., 2011, *A&A*, 527, A3 14, 17
- van Winckel H., 2003, *ARA&A*, 41, 391 4, 6
- Ventura P., Dell'Agli F., Lugaro M., Romano D., Tailo M., Yagüe A., 2020, *A&A*, 641, A103 4
- Vermeulen O., et al., 2025, arXiv e-prints, p. arXiv:2507.03583 12
- Vigna-Gómez A., Toonen S., Ramirez-Ruiz E., Leigh N. W. C., Riley J., Haster C.-J., 2021, *ApJ*, 907, L19 5
- Vigna-Gómez A., et al., 2025, arXiv e-prints, p. arXiv:2503.17006 5
- Vink J. S., Harries T. J., 2017, *A&A*, 603, A120 4
- Vink J. S., de Koter A., 2005, *A&A*, 442, 587 4
- Virtanen P., et al., 2020, *Nature Methods*, 17, 261 24
- Vogelsberger M., et al., 2014, *MNRAS*, 444, 1518 14
- Voronoi G., 1908, *Journal für die reine und angewandte Mathematik (Crelles Journal)*, 1908, 97 19

- White R. M. T., Tuthill P., 2026, in Encyclopedia of Astrophysics. pp 584–603, doi:10.1016/B978-0-443-21439-4.00067-5 2, 3, 5, 7, 8
- White R. M. T., Pope B. J. S., Tuthill P. G., 2024, Geometric Modelling of Wolf-Rayet Binary Colliding Wind Nebulae, unpublished Honours Thesis 2, 28, 41, 42, 44, 45, 46, 51, 57
- White R. M. T., Pope B. J. S., Tuthill P. G., Han Y., Dholakia S., Lau R. M., Callingham J. R., Richardson N. D., 2025, arXiv e-prints, p. arXiv:2507.14610 2, 8, 9, 16, 17, 21, 33, 38, 41, 42, 43, 44, 45, 46, 49, 50, 51, 52, 57
- Williams P., 2011, arXiv e-prints, p. arXiv:1101.1046 23, 24, 36, 37
- Williams P. M., 2019, MNRAS, 488, 1282 10
- Williams P. M., et al., 2009, MNRAS, 395, 1749 17, 23, 39, 45
- Williams P. M., van der Hucht K. A., van Wyk F., Marang F., Whitelock P. A., Bouchet P., Setia Gunawan D. Y. A., 2012, MNRAS, 420, 2526 33
- Williams P. M., van der Hucht K. A., van Wyk F., Marang F., Whitelock P. A., Bouchet P., Gunawan D. Y. A. S., 2013, MNRAS, 429, 494 10
- Wolf C. J. E., Rayet G., 1867, Academie des Sciences Paris Comptes Rendus, 65, 292 6
- Woosley S. E., 1993, ApJ, 405, 273 4
- Woosley S. E., Heger A., 2006, ApJ, 637, 914 4
- Zhekov S. A., Gagné M., Skinner S. L., 2011, ApJ, 727, L17 43

List of External Links

ThreeBodyBot	https://github.com/kirklong/ThreeBodyBot	5
Velocity Slicing Nebulae	https://ryanwhite1.github.io/xenomorph/tutorials/velocity_cube/	23
UK IR Telescope	https://about.ifa.hawaii.edu/ukirt/calibration-and-standards/astromonical-utilities/zero-mag-fluxes-and-conversions/	31
NSFCam	https://irtfweb.ifa.hawaii.edu/ nsfcam2/Filter_Profiles.html	31